UNIVERSITY OF CALGARY

Microseismic Monitoring and Hypocenter Location

by

Lejia Han

A THESIS
SUBMITTED TO THE FACULTY OF GRADUATE STUDIES
IN PARTIAL FULFILMENT OF THE REQUIREMENTS FOR THE
DEGREE OF MASTER SCIENCE

DEPARMENT OF GEOSCIENCE
CALGARY, ALBERTA
December, 2010

UNIVERSITY OF
CALGARY

ABSTRACT

Well fracturing or CO_2 sequestration produces microseismic events that indicate the location of the injected fluids, providing feedback on the stimulation objectives. This thesis provides improvement to standard procedures to locate the microseismic events more accurately.

Three methods, for arrival time-picking, propagation polarization approximation, and hypocenter localization of microseismic events, are proposed in this thesis along with a particular noise attenuation approach to pre-process raw microseismograms. The three proposed methods are named as modified energy ratio analysis, hodogram analysis, and back-propagation analysis. They are stable and robust for microseismic monitoring.

Effective noise attenuation, event-detection trigger, propagation polarization by weighted least-squares regression on hodograms, and hypocenter estimation are also included. A novel approach for finding the nearest point to two spatial lines is included to estimate a source location.

The joint procedure integrating all proposed methods was implemented in MATLAB software and can consistently produce hypocenter locations at a signal to noise ratio of 3.

ACKNOWLEDGEMENTS

I would like to thank a number of people who have helped, advised, and encouraged me immensely and generously in completing this thesis research:

Thanks to my first supervisor, Dr. Robert R. Stewart who moved to Houston.

Thanks to Dr. John C. Bancroft who became my supervisor, without your assistance, I might have failed at the very early time of this program. I hope that I might qualify now to follow you for the challenges in migration and inversion technologies.

A special thanks to Dr. Joe Wong, who gave assistance in implementing many of the algorithms used in this thesis. I would not have improved and progressed so much without your assistance.

Thanks to Dr. Gary F. Margrave, the primary author of the CREWES toolbox where I've frequently adopted the coding techniques and algorithms dealing with seismic problems in my research applications.

Thanks to Dr. Don Lawton for your advice, right after the one-hour final examination of the GOPH701 project, to take the non-program required course however compensate my geophysical fundamentals. And thanks John for having pushed me to follow your advice as I didn't realize it was necessary until in the middle of that course.

Thanks to Dr. Larry Lines for your questions, interests, and encouragements during and after my oral and poster presentations. Although I didn't take your course formally, your course textbooks and references did interest me a lot and gave me so much information to compose the first chapter of this thesis.

Thanks to Dr. Robert Ferguson, for your theoretical imaging course, where the tedious mathematics applied in geophysics in this subject begin being more meaningful instead of puzzling and boring me.

Thanks to Dr. Michael Lamoureux, for your wave-related math course, where I got more understanding on related-electronics as well.

Thanks to Dr. Kristopher Innanen, for your questions on my posters, this gave me ideas about the presentation in a very limited space and sufficient preparation for related questions from professionals.

Special thanks to Dr. Rolf Maier for your tremendous editing time and writing help for this thesis.

Thanks to Ms. Laura Baird, Ms. Cathy Hubbell, and Ms. Louise Forgues, for many help, advice, and consulting during the past.

Thanks as well for the excellence of the management, facility, and resources from the Department and the University that I've also benefited much during the past three years.

DEDICATION

To my parents, daughter, loved ones, and others, near and far, who have greatly help me.

TABLE OF CONTENTS

LIST OF FIGURES

LIST OF TABLES

LIST OF ABBREAVIATIONS

1C:	One-component
3C:	Three-component
2D:	Two-dimensional
3D:	Three-dimensional
S-wave:	Shear-wave
P-wave:	Primary-wave
ER:	Energy ratio
RMS:	Root-mean-square
MER:	Modified energy ratio
MVA:	Minimum variance
STA/LTA:	Short term average/long term average
ATA:	After-time average
BTA:	Before-time average
DTA:	Delayed-time average
HDR:	Hard and dry rock
CTBT:	Comprehensive Test Ban Treaty
WWSSN:	Worldwide Standardized Seismographic Network
bp-filter:	Bandpass filter
Mm-stack:	MER-*stack* with matched filtering adjustment
MER-*stack*:	Trace stack by MER shifts
MVA-*stack*:	Trace stack by MVA shifts
NSS:	Noise signal separation
SNR:	Signal to noise ratio

Chapter One: Introduction, objectives, and outline

1.1 General understanding and perspective of microseismic monitoring

Microseismic monitoring has only been used in the petroleum industry in recent years, much later than in other cross-industry applications such as the mining industry or geothermal resource exploration. However, seismic monitoring techniques, along with the science of seismology, have a long history of developments, from ancient earthquake monitoring to modern microseismic monitoring.

1.1.1 Seismic monitoring and the evolution of seismic sensors

Seismic monitoring is of interest both on the global scale, detecting events across thousands of kilometres as for instances in earthquake monitoring, and on the local scale for detecting events only hundreds or perhaps thousands of meters away as in microseismic monitoring.

In terms of energy released underground, teleseismicity, seismicity, and microseismicity are so called to distinguish the energy amount as well as the monitoring scale. Teleseismicity refers to ground motions caused by strong, long-distance sources, for instance, natural earthquakes or nuclear explosions. Microseismicity refers to ground vibrations caused by much weaker events on a local scale, where the man-made ones are of most research interest, for example, mining operation and oil production.

Earthquakes are familiar to most people, perhaps because of historic natural disasters and their devastating effects on human civilizations. To seismologists, microseisms are also tiny earthquakes. Most natural earthquakes are very small; hence

they can only be registered by sensitive seismographs and therefore receive no attention from non-seismologists.

Seismic monitoring can be dated back to 132 A.D. by the earliest known seismoscope built by a Chinese astronomer, Heng Zhang, during the Han dynasty of China (Dewey and Byerly, 1969). This elegant mechanical seismoscope, depicted in Figure 1.1, enabled an observer to view the direction of arrival of the seismic wave from where the ground motion came, even though it could not provide a permanent record of the seismic wave itself.

Figure 1.1: The earliest known mechanical seismoscope, built by a Chinese astronomer in 132 A.D.

Historically, the advancement of seismic recording techniques has been credited as enabling seismology to proceed to being a science since 1892, when the English scientist John Milne invented a seismograph that can produce a recording of an unfelt ground vibration.

John Milne, James Ewing, and Thomas Gray, working in Japan as visiting professors in the years1880-1882, developed the early work for the first practical

horizontal- and vertical-motion seismographs, with the ability to convert an unfelt ground vibration into a permanent visible record as a function of time. The sensor used to detect ground vibrations (called a seismometer) was based on long-period pendulums with long arms and heavy weights. Recordings were made by scratching a stylus on smoked-glass plates. Milne continued to improve on the early designs after he returned to England in 1895 (Dewey and Byerly, 1969).

In 1904, the German seismologist Emil Wiechert described an improved seismometer that included viscous damping. It reacted to a broader band of seismic frequencies by increasing sensitivity to low-period vibrations, but it carried an inertial mass of 1000 kg. Later, Wiechert built similar seismometers with inertial masses as low as 80 kg. For the seismic exploration profession, an important development was the introduction in 1903 of the electromagnetic seismometer by Prince Boris Galitzin of Russia, who based the sensing of ground motion on sensitive galvanometers (Dewey and Byerly, 1969). Galitzin's electromagnetic seismometer has evolved into the modern light-weight moving-coil geophones (as shown in Figure 1.2) so critically important to the entire seismic acquisition industry.

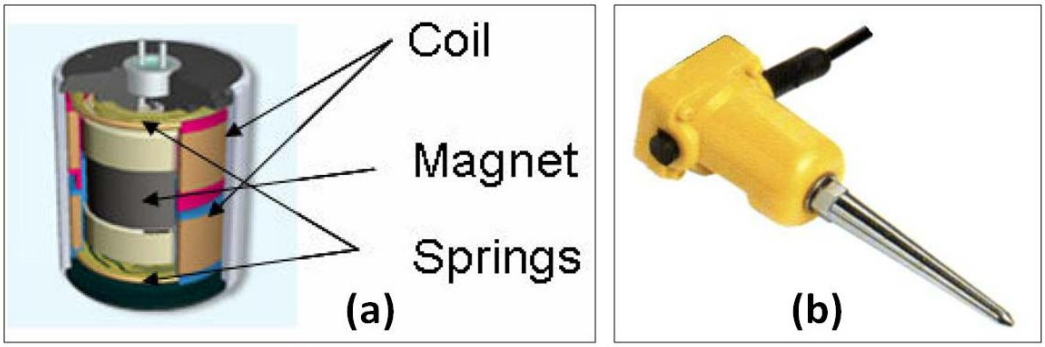

Figure 1.2: A moving-coil geophone shown (a) in structural elements and (b) in a land case. (Modified from ION product brochure)

In recent years, seismometers based on micro-electromechanical systems (MEMS) have been introduced (Maxwell, 1999). These are accelerometers (similar to those used in car airbag control circuits) that can be mass-produced with very closely matched response curves. MEMS-based geophones (as shown in Figure 1.3) have low intrinsic noise and ultralow distortion. They are smaller and lighter than moving coil geophones, and hold the prospect of providing a broader-band frequency response (Stewart, 2009).

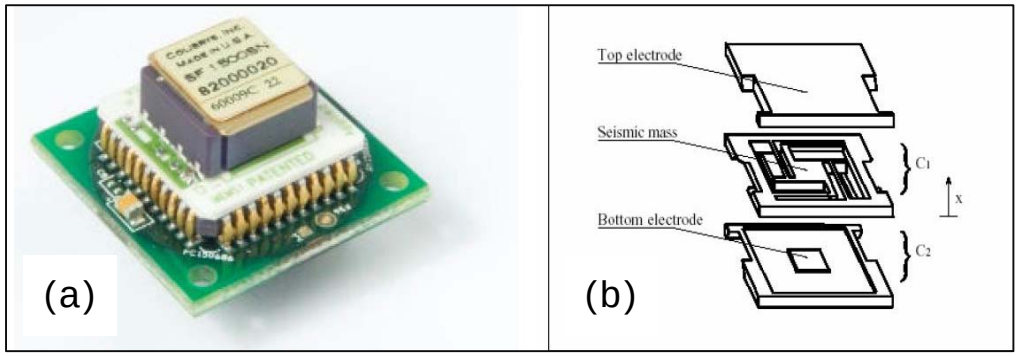

Figure 1.3: (a) MEMS accelerometer chip (Colibrys) and (b) cutaway cartoon (Kraft: 1997).

Recording systems also have advanced from the days of scratches on smoked glass plates. Thanks to modern computers, permanent electronic records of millions of digital seismograms can be stored for extended periods of time, regardless whether processing takes a few short seconds or as long as hours.

Along with the evolution of seismic sensors, the intensive study and understanding of seismology, as well as the development of seismic monitoring techniques, have made great strides in recent history.

Beginning in 1897, Milne had pressed for the establishment of a world-wide array of standardized seismographs so that teleseismicity caused by earthquakes could be

monitored. By 1900, Milne-type seismographs had been established on every inhabited continent in the world (Dewey and Byerly, 1969). Today, thousands of seismic stations exist worldwide for earthquake monitoring.

1.1.2 Seismic monitoring advance with nuclear weapons tests

The science of seismology, along with seismic monitoring techniques, was stimulated strongly in the 1950s and 1960s, due to the rapid development and intensive testing of nuclear bombs.

Nuclear explosion tests were mainly made underground in the 1960s, as they were banned in outer space, in the atmosphere, and underwater, by the Limited Test Ban Treaty (LTBT) signed by the United States., the Soviet Union and Great Britain in 1963.

The Comprehensive Test Ban Treaty (CTBT) in the 1950s was intended to outlaw all nuclear weapons tests. It needed monitoring mechanisms by which breaches of the ban could be spotted. Underground testing of nuclear explosions generates elastic wave energy that travels along great distances through the Earth, and the detection of seismic waves quickly became a major focus of the seismic monitoring community (Richards and Kim, 2009).

Fortunately, the sensors that detected earthquakes could do double duty in detecting bomb blasts. With this in mind, the U.S. government in 1959 initiated the Worldwide Standardized Seismographic Network (WWSSN), and began pouring millions of dollars into basic seismological research, giving a tremendous boost to what was then a peripheral field of study. The WWSSN was the first global seismic network, consisting of 120 stations (O'Hanlon, 2001).

Originally, seismometers were sensitive only to vibrations at a particular frequency, so seismic stations had to use arrays of different seismometers to monitor the range of vibrations that were of interest. But the development in the mid-1980s of broadband seismometers, which are sensitive to vibrations at a wide range of frequencies, made it easier and cheaper to add new stations to the global network. More than 16,000 seismic stations incorporating high-sensitivity triaxial (three-component) geophones now cover the globe (O'Hanlon, 2001). Figure 1.4 shows an example of a section view of hypocenters, i.e., earthquake focal points at depth, for a subduction zone, west of South America.

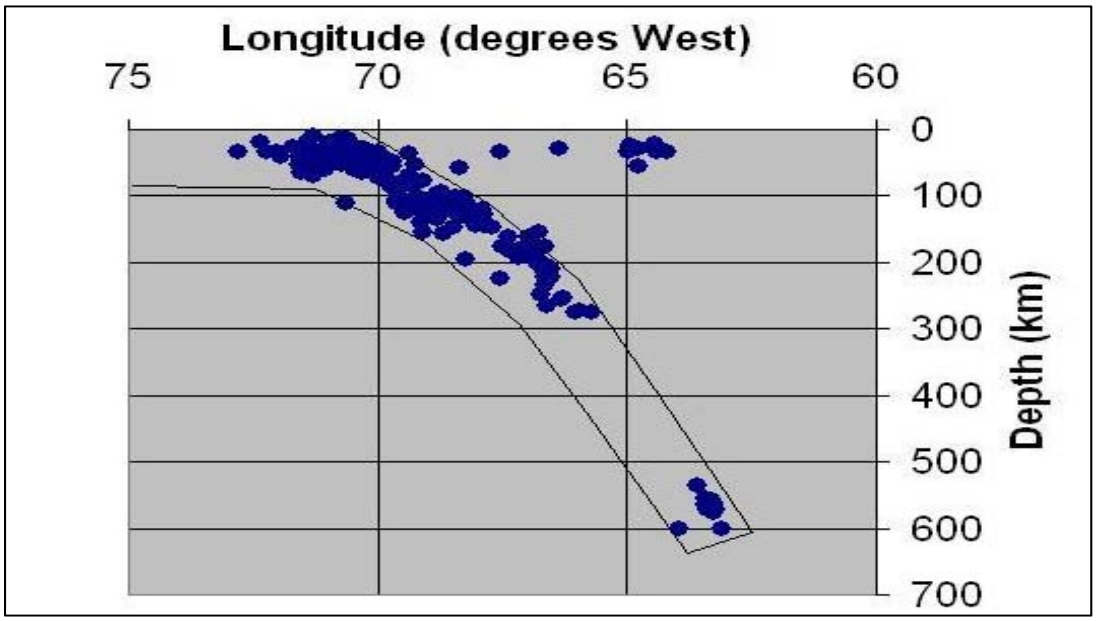

Figure 1.4: Earthquake hypocenters in the section view of a subduction zone. (http://web.ics.purdue.edu/~braile/edumod/epiplot/epiplot.htm)

According to Richards and Kim (2009), more than 600 earthquakes a day find their way into an international summary report, that include many more seismic events caused by mining operations that explode millions of tons of blasting agents a year. About 25 seismic events above a magnitude of four take place every day, and that

number goes up by a factor of about 10 for each drop of one unit in magnitude (say, from 25 to 250 events a day for a drop in magnitude from four to three).

1.1.3 Earthquake monitoring and plate tectonics

As WWSSN seismologists started to detect, locate, and map the world's earthquakes on the earth' surface, the collected epicentres started to delineate the hitherto unknown boundaries of the Earth's crustal plates. In addition, locating earthquake focal points in depth revealed the existence of subduction zones, at which thin, moving oceanic plates are forced into the earth's mantle by thicker continental crust. Figure 1.5 displays the Pacific Ring of Fire, i.e., belts of major volcanic activity around the Pacific Basin. The coincidence of epicentres with arcs of major volcanic activity was extremely strong evidence supporting the theory of plate tectonics (O'Hanlon, 2001).

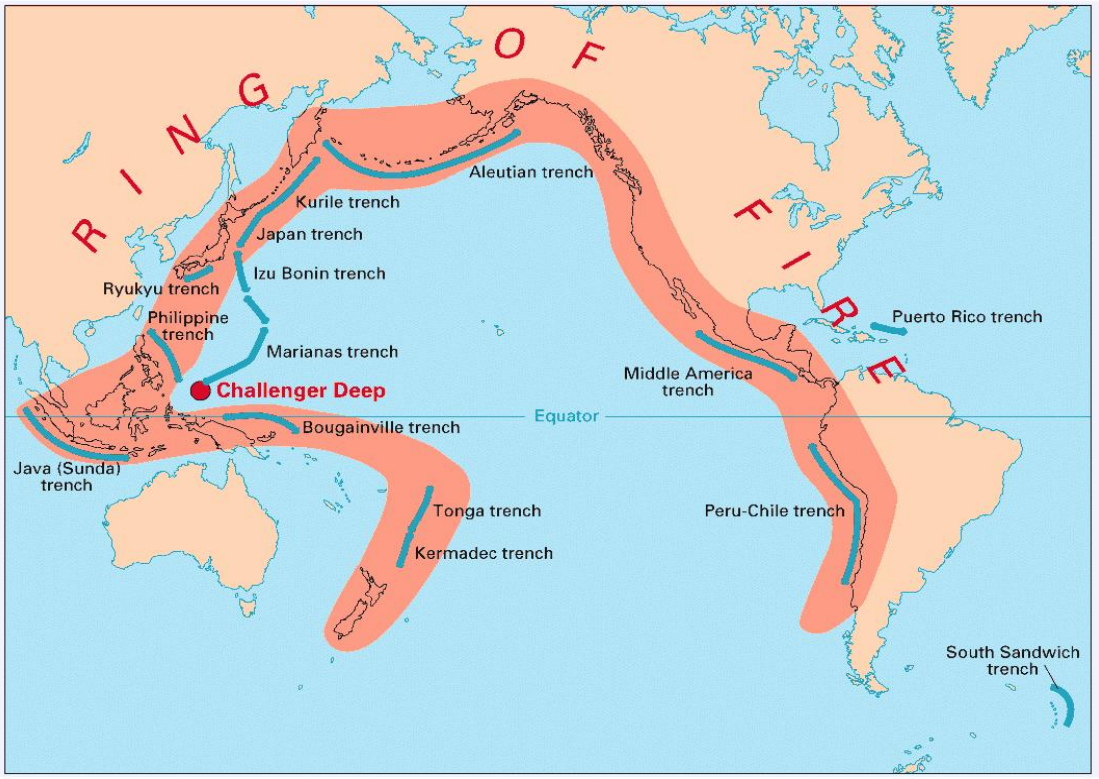

Figure 1.5: Volcanic arcs and oceanic trenches (in blue) partly encircling the Pacific Basin form the so-called Ring of Fire, a zone of frequent earthquakes and volcanic eruptions (http://pubs.usgs.gov/publications/text/fire.html).

The observation and analysis techniques used in passive monitoring of teleseismic events have been adopted for practical application on a much smaller scale. These microseismic applications occur in such diverse activities as deep underground mining, geothermal development, CO_2 sequestration, and well fracturing (fraccing).

1.1.4 Microseismic monitoring in deep underground mines

One of the earliest uses of microseismic monitoring was the detection and possible prediction of rock bursts in deep underground mines (Brady, 1977; Brady, 1974). The opening of a mine shaft relieves neighbouring rocks of tremendous pressure. The stress relief can cause the rock literally to explode spontaneously and violently as it attempts to re-establish equilibrium. Rock bursts that cause roof and wall collapses can result in rock falls of 100 to 200 tonnes or more, and are a serious hazard. In South Africa, they kill roughly 20 miners each year (Monroe and Wicander, 96). Similarly, outbursts in coal mines, involving the sudden and violent ejection of coal, gas, and rock from a coal face and surrounding strata, are dangerous and can cause multiple fatalities. Hasawega et al. (1989) has given an account of mine-induced seismicity in the potash, coal, and hard-rock mines in Canada. Monitoring of mine-induced microseisms and locating areas of unusual microseismic activity contributes significantly to mine safety.

1.1.5 Microseismic monitoring in geothermal reservoirs

In another early application at the Los Alamos National Laboratory in New Mexico, microseismic monitoring was used to follow hydraulic fracturing of crystalline rock in a test of the “hot dry rock,” or “HDR,” technique of geothermal energy production (House, 1987; Block et al., 1994). The HDR concept consists of extracting

heat energy from the earth's crust by circulating water through man-made fractures between two deep wellbores within otherwise impermeable rock. While the fractured reservoir was being created (by hydraulic fracturing), downhole geophones were used to monitor the induced microseismic events. Mapping of the points of rock breakage during fracturing was done by inverting observed arrival times of P and S waves at an array of downhole geophones to obtain the hypocenter locations.

1.1.6 Microseismic monitoring in hydrocarbon reservoirs

Passive microseismic monitoring in the oil and gas industry is an instance of multi-component seismic exploration where arrays of three-component (3C) geophones are used to detect ground vibrations. Rather than using the standard airguns, vibrators, or dynamite in conventional seismic surveys, passive seismic recording aims at the weaker wave signals from sources of opportunity, for example, rock fracturing.

Man-made microseismicity is usually induced by high-pressure injection in a hydrocarbon reservoir for deliberately fracturing rock and increasing the permeability and porosity of underground formations surrounding a producing well and the flow of oil and/or gas to the well.

When high-pressure fluids or gas are injected into underground formations, changes in effective pore pressures can be large enough to reactivate pre-existing faults and fractures, or even create new ones. This is illustrated in Figure 1.6 that shows hydraulic fracturing or CO_2 sequestration.

Man-made rock fracturing and surface deformation induced by Cyclic steam injections (CSS), as well as the steam-assisted gravity drainage (SAGD) processes (Maxwell et al., 2008), have been reported in heavy-oil projects. These artificial fracture

formation and fault movement may emit very small seismic signals that can only be detected by microseismic monitoring (Verdon et al., 2010).

Combined with other passive monitoring techniques such as tiltmeter measurements, microseismic monitoring helps reservoir engineers track the fracturing progress and extent, and then evaluate the affected reservoir volume (Maxwell and Urbancic, 2001).

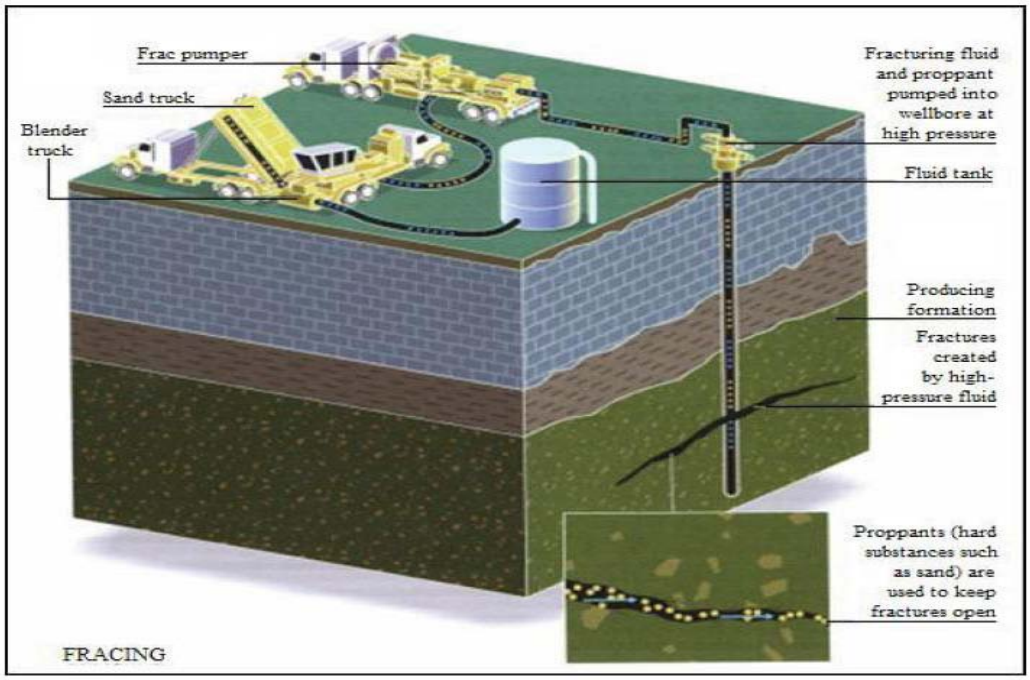

Figure 1.6: Man-made rock fracturing in a hydrocarbon reservoir. Artificial rock fracturing increases the production in a well by injecting fluids/gas, sand, and a mixture of chemicals at high pressure and causing the formation rock to crack (www.worc.org/userfiles/file/EPA-FracStudyFactSheet.pdf).

Microseismic monitoring has also been used in the surveillance of accidents related to heavy-oil production, such as well-casing failures, cement cracking, and unintended fluid flow. These failures have serious environmental consequences for groundwater and surface water resources.

Mandated by government regulations, microseismic monitoring has been extensively used and fully incorporated into heavy-oil field operations in Alberta (Maxwell and Urbancic, 2001).

Pioneering tests for reservoir characterization by oil-production-induced microseismicity were conducted from 1993 to 1995 in the Seventy-Six oil field, Clinton County, Kentucky (Rutledge et al., 1996). Well-established earthquake monitoring procedures were modified to develop monitoring and mapping techniques suitable for a reservoir setting. Their results proved the ability of microseismic monitoring to contribute to reservoir characterization.

Passive seismic monitoring for reservoir characterization in the petroleum industry has developed rapidly in recent years. Used in conjunction with horizontal drilling and multi-stage completions, it has helped hydraulic fracture stimulation to transform huge volumes of previously uneconomic rock into productive hydrocarbon reservoirs (Stewart, 2009). Stimulated production from methane-rich coal beds, gas-bearing shales, and tight sandstone formations has contributed hugely to the continued growth of the oil and gas industry worldwide.

Figure 1.7 shows a typical configuration for microseismic monitoring in support of a hydraulic fracturing project. An array of 3C geophones is deployed in the observation well on the left. Multiple zones in the treatment or producing well on the right are sequentially isolated by packers and stimulated by hydraulic fracturing. When the rock cracks, a small earthquake is produced and seismic energy is released at the point of rupture. By recording three-component microseismograms and using the

information to locate microseismic hypocenters, the direction and extent of fracture growth can be tracked.

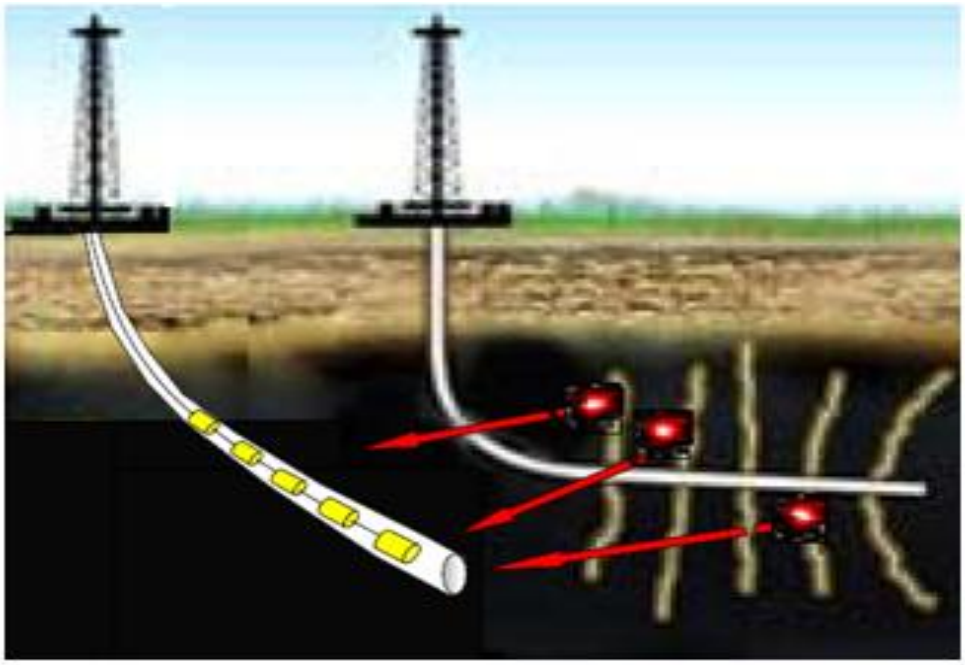

Figure 1.7: The observation well (left) monitoring microseisms with 3C geophones, and the treatment well (right) undergoing hydraulic fracture stimulation. (Courtesy Mahrer, 2009)

1.2 Objectives and contributions of this thesis

Microseismic monitoring has supported a variety of resource development projects, though they have only been applied recently in the petroleum industry. Its ability to map the opening of fractures or movement of fluids is of particular interests in hydrocarbons exploration and developments.

Commercial software for locating microseismic events is available, however, the detail of the algorithms used are rarely presented in the literature. It is the purpose of this thesis to present the details of algorithms that I have developed for location microseismic events.

Typical solutions in microseismic event detection and localization are reviewed first; then the modified energy ratio (MER) method is proposed as an alternative to the commonly used standard energy ratio of short term average to long term average (STA/LTA) method for event detection and arrival time picking. Hodogram polarization analysis in both 2D and 3D spaces then follow as an alternative to polarization analysis approach by eigenvectors/eigenvalues. Back-propagation analysis in both 2D and 3D approaches are then proposed as an alternative to the commonly used τ_S-τ_P method for locating microseismic hypocenters.

Weak energy is a distinguishing character for microseismic monitoring and several noise attenuation schemas are introduced and compared. With the optimal noise attenuation solution introduced in this thesis, all joint methods implemented on MATLAB platform for microseismic monitoring in both 2D and 3D scenarios (including MER analysis, hodogram polarization analysis, back-propagation analysis) can tolerate Gaussian noise down to a very low signal noise ratio.

1.3 Outline of the thesis

This thesis is to be presented in the following outline:

Chapter 1: Provide the general background information on seismic monitoring.
Chapter 2: Review techniques used in microseismic monitoring.
Chapter 3: Introduce MER event detection method.
Chapter 4: Analyze an optimal noise attenuation schema.
Chapter 5: Introduce hodogram polarization analysis for wave propagation.
Chapter 6: Introduce back-propagation analysis for hypocenter location.
Chapter 7: Conclude this thesis research.

Chapter Two: Review of techniques used in microseismic monitoring

2.1 Introduction

Table 2.1 is a flow chart showing the main steps in carrying out a microseismic monitoring survey in support of man-made rock fracturing in a gas/oil reservoir by hydraulic stimulation, cyclic steam injection, or CO_2 sequestration, as mentioned previously. The primary purpose of such a microseismic survey is to track the growth and spatial extent of the induced fractures by locating microseisms associated with induced fracturing. The focus of this thesis is on the tasks in the flow chart that are required, namely,

- identification of valid events,
- time-picking of microseismic arrivals, and
- location of microseismic hypocenters.

The identification and time-picking steps are usually done as a single operation. There are a variety of techniques for carrying out these tasks, some adapted from earthquake seismology, and some specifically developed by the microseismic community to address the particular characteristics of microseismic data from a reservoir. In the following sections, I review the most relevant procedures found in the literature.

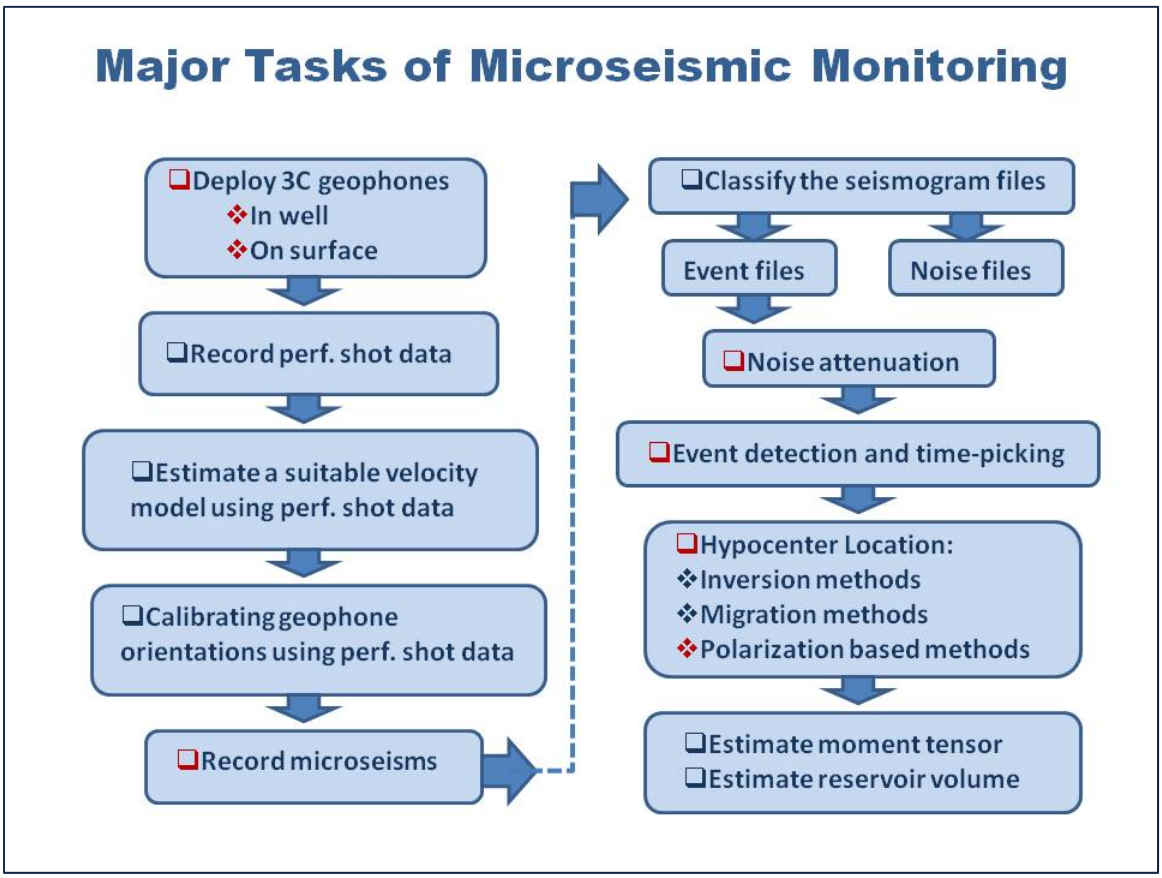

Table 2.1: Flow chart of major tasks for a microseismic monitoring survey in support of hydraulic fracturing of a hydrocarbon reservoir. Tasks marked by red squares are evaluated in this thesis research.

2.2 Automated seismic event detection and arrival time picking methods

Valid events on microseismograms include either *P*- or *S*- wave arrivals, or both. They could be identified and the arrival times picked manually, but continuous, long-term monitoring usually generates huge amounts of data that render manual identification and picking impractical. Fast, automatic techniques are therefore necessary for real-time monitoring and analysis (Oye and Roth, 2003).

Automated algorithms for global seismic phase and event detection have been reviewed periodically during the past (e.g., Beger and Sax, 1980; Allen, 1982; Withers et

al, 1998), and some methodology surveys have been conducted in more detailed ways within CREWES (Munro, 2005). The following is a historic view of the detection methods.

2.2.1 Time Domain Methods

The earliest and still popular method to find transient energy in the time domain is the STA/LTA technique (Saari, 1991; Withers et al., 1998). This method calculates average energies in a long time window (the long-term average, or LTA) and in a short time window (the short-term average, or STA) preceding a test point on a seismogram, as shown in Figure 2.1. The length of the STA window is set to be about two to three dominant periods of the seismic arrival; the LTA window is set to be five to ten times longer. A sharp increase in the plot of the STA/LTA ratio as a function of time is indicative of a seismic event as well as its arrival time. The STA/LTA method was first introduced on rectified data by Vanderkulk et al. (1965), later followed by Allen's (1978) method which utilizes squared data plus the weighted square of the first derivative. Notice that the standard STA/LTA ratio using squared data is also an estimate of the signal-to-noise ratio (SNR), with the STA representing the signal energy and the LTA representing the background noise.

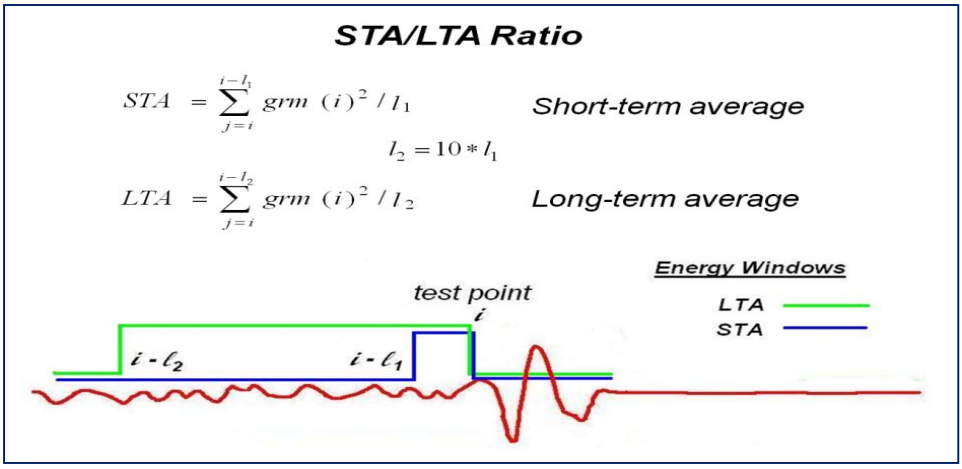

Figure 2.1: Formulation of the STA/LTA time picking method. Notice that window LTA (in green) is much longer than window STA (in blue).

Various modifications of the standard STA/LTA analysis improve the discernment of the event from a noisy background, usually at the expense of increased computational complexity, as discussed below.

Coppens (1985) combined the STA/LTA algorithm with coherency filtering to pick first arrival times on common-offset gathers of noisy seismograms. These first-arrival times were required for making static corrections before reflection imaging.

Willis and Toksoz (1983) used semblance and statistical analysis to obtain the arrival times of the P events on noisy multi-channel full waveform well logs. Then, using a trace from a reference channel, they cross-correlated the windowed P arrival with the rest of the trace to find an S arrival of similar waveform. This S arrival was windowed and cross-correlated with the traces from the remaining channels to obtain the time delays of the S events on different receiver channels from a common source. They called this the P-correlated S picking procedure.

Sarri (1991) took advantage of directional data from 3C recordings of passive microseismic earthquakes, and multiplied the components together, bandpass filters the

product, and then applies the STA/LTA triggering analysis, and was shown to be able to provide time picks appropriately based on a single station.

Withers et al. (1998) combined the STA/LTA analysis with adaptive window lengths and waveform correlation and proved its ability to detect seismic events on 150 channels of tele-metered broadband data in real time.

Oye and Roth (2003) combine the STA/LTA trigger with error prediction filtering in an auto-regressive model for P-waves, while a ray path rotation procedure is added for S-phase detection. This event detector is demonstrated on 3C microseismograms in real time and worked quite well.

Other formulations of energy transients for event-detection and arrival time-picking have been researched within CREWES. For example, a 3-window, 2-energy ratio trigger was constructed and shown to work well on noisy synthetic microseismic data (Chen and Steward, 2004). They calculated after-time average (ATA), before-time average (BTA), and delayed-time average (DTA) energies for a test point on a seismogram. Two ratios, ATA/BTA and DTA/BTA, are then used with statistically defined thresholds to pick the arrival times of both P and S phases. To improve the time-picking accuracy of the S-wave, whose onset is often interfered with by the earlier arriving P-wave coda, the detector also employs a polarization filter (Flinn, 1965; Vidale, 1971) on 3C seismograms to isolate the longitudinal and transverse particle motions.

Another recently developed energy transient trigger, different from but similar to both STA/LTA and ATA/BTA/DTA analysis, is to be introduced in this thesis as the MER method, as shown in Figure 2.2. Details are given in Chapter 3.

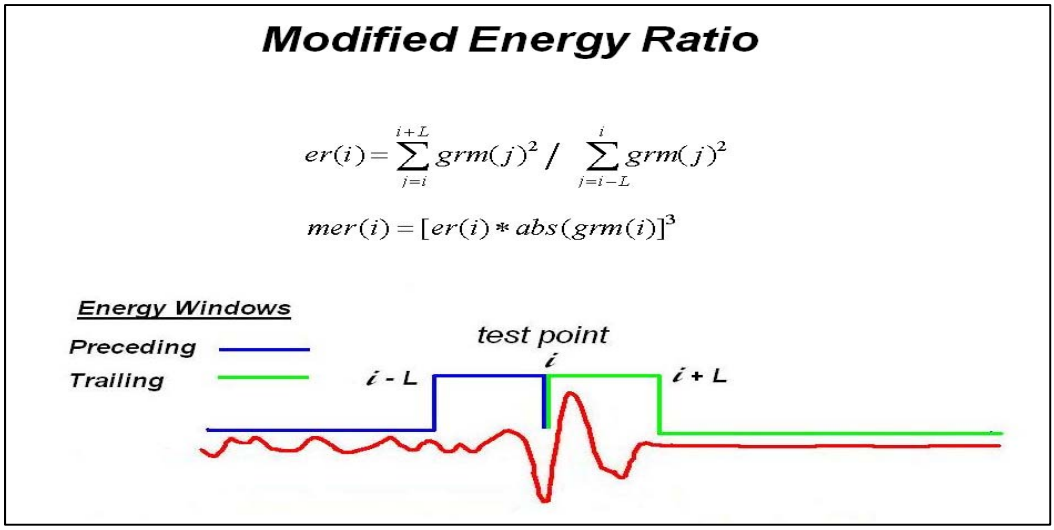

Figure 2.2: Formulation of the MER time picking method. Notice that both windows (blue & green) have the equal size.

Certainly there are many time domain methods that are not triggered by any kind of energy transient at all, which are valuable as well, for example, the pattern-matching schemas (e.g., Joswig, 1990; Gibbons and Ringdal, 2006, Einner et al., 2008, Hanafy et al., 2008), and the peaks and/or troughs analysis (Anderson, 1978; Murdoch and Hutt, 1983; Tan and Stewart, 2006). For another example, wavelet transforms were applied to seismic data first by Donoho (1993), and were then implemented by Ebel (1996).

2.2.2 Frequency domain methods

Frequency domain triggers are in general more computationally intensive than time domain triggers, however, they usually can stand alone to produce more reliable time picks at lower SNRs, and some of them can provide additional information (e.g. PSD detector, Shensa, 1977; Walsh transform, Goforth and Herrin, 1980; S-transform, Pinnegar and Mansinha, 2003; Gabor transform, Margrave and Lamoureux, 2005).

For example, the S-transform detector (Pinnegar and Mansinha, 2003) used a time-frequency filter for the polarity information from the detected event with the improved resolution of wave train initiation time over the Gaussian S-transform (Stockwell et al., 1996). Figure 2.3 shows a noisy seismogram and its S-transform, where the presence of the P arrival is clearly visible by the red energy in the center, although it is difficult to pick an accurate arrival time.

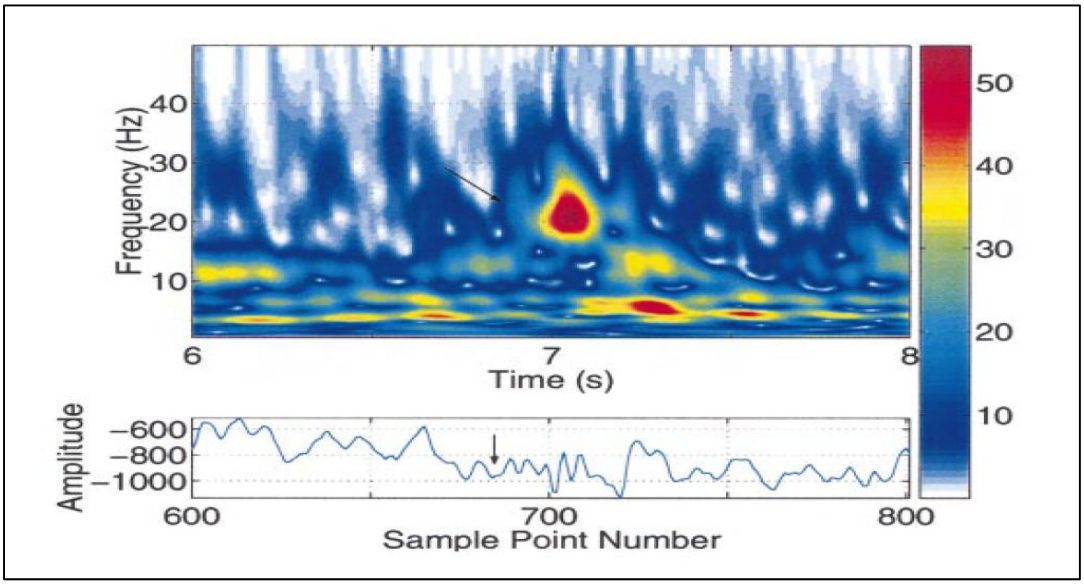

Figure 2.3: A noisy earthquake seismogram (bottom) and its S-transfrom (top). The arrow shows the onset of the P-wave arrival (from Pinnegar and Mansinha, 2003).

CREWES has developed and advanced a frequency-domain detecting algorithm, called Gabor-transform (Margrave and Lamoureux, 2005). In general, it involves taking the Fourier transform of short time portions of the seismogram and plotting the amplitude spectrum as a function of time.

It should be noticed that time-domain triggering schemas can be computationally intensive as well. For example, a fractal-based algorithm (Boschetti et al., 1996) requires that the fractal dimension in time domain of a seismic trace be determined. This

calculation is much more time-consuming than energy ratio computations. However, the extra effort is rewarded by the ability to tolerate noise up to 80% of the average signal amplitude (SNRs of about 1.33). Such noise levels are approximately one order of magnitude larger than the noise levels tolerated by the STA/LTA combined with Copper's (1985) coherency evaluation.

2.3 Microseismic hypocenter localization techniques

Once P- and/or S- arrivals are identified and time picks obtained manually or automatically from recorded microseismograms, the next step is to locate the hypocenters of microseismic sources. In this section, typical techniques for locating epicentres or hypocenters will be reviewed and discussed in terms of location uncertainty, noise tolerance, computing complexity, and improvements to the original versions if applicable, according to the following outline:

2.3.1 Inversion and migration techniques

2.3.2 Techniques based on propagation direction or polarization

2.3.2.1 Polarization analysis techniques

- eigenvector analysis
- ***hodogram analysis (in this thesis)***

2.3.2.2 Location methods based on propagation direction or polarization

- τ_S-τ_P methods
- ***back-propagation methods (in this thesis)***

2.3.3 Other techniques

2.3.4 Summary

2.3.1 Inversion and migration techniques

Microseismic hypocenters can be located by conventional seismological methodologies such as inversion and migration. Such algorithms are mostly successful at regional and teleseismic distances where they may face data perturbed by small-scale structural heterogeneities causing phase shifts, mode conversions, mutipathing, and scattering in microseismic monitoring applications.

A particular challenge to using inversion techniques for locating microseisms comes from the scale difference, as the dimensions of regional velocity models could be tens of kilometres, whereas for microseismic inversion grid considered is usually 1km or less.

Another practical difference is that passive microseismic monitoring in hydrocarbon reservoirs is most likely through borehole arrays which contain far fewer geophones than regional seismic survey networks. Thus, any inversion algorithm is not well constrained.

The joint hypocenter-velocity inversion technique (Crosson, 1976a and b; Aki and Lee, 1976) has been improved and used for structure studies of the crust and upper mantle in many regions of the world (Kovh, 1985; Roecker et al., 1987; Eberthart-Pillips, 1990; Michelini and McEvilly, 1991). The adaption of this method to the 3D velocity model for microseismic hypocenter location (Block et al., 1994) has been borne out by the simultaneous inversions of P-wave and S-wave data from 4-geophone borehole monitoring of geothermal energy. It recursively produces a refined 3D velocity model for the monitored area, and improves the absolute and relative microseismic location uncertainty as much as 35 and 40 percent respectively. It also proved able to yield more

accurate hypocenter locations at large monitoring scales with a 3D velocity model instead of a homogeneous earth.

Another inversion technology, so-called tomography, has been broadly confirmed as being able to obtain the hypocenter coordinates and velocity structure simultaneously. For example, Waldhauser and Ellsworth (2000), and Zhang and Thurber (2000) have described a double-difference (DD) tomography algorithm. The algorithm is based on observed and calculated arrivals times of two events observed at a common station. The first difference is formed by subtracting the calculated arrival time from the observed arrival time for each of the two events. The second difference is formed by subtracting the event one difference from the event two differences. Simultaneous inversion for source coordinates and velocity values is done on the double differences of multiple stations. According to Zhang and Thurber (2004), the use of the DD technique and the refinement of the velocity structure lead to significant improvement in the relative locations of hypocenters (Pavlis, 1992). Zhou et al. (2010) has applied the method to microseismic data from monitoring of a CO_2 sequestration project and given the more recently, inversion based double-difference as reported.

Oye and Roth (2003) have implemented a highly non-linear inversion technique with a global derivative-free search routine for ray-tracing a 3D velocity field to the microseismic hypocenter. It involves a matrix and least squares iteration from a specific start model.

A pattern search inversion technique has been recognized and recommended for microseismic localization and a horizontal-layer velocity calibration using P-wave arrival times from a perforation check shot. This conclusion is based on a comparison of

experiments using three inversion algorithms, these being the genetic algorithm (GA), pattern search (PS) algorithm, and the Levenberg-Marquardt (LM) algorithm (Wong, 2009).

The inversion techniques for microseismic monitoring generally have the advantage of better noise tolerance and hence a more accurate estimate of the location. However, this technique usually comes with the drawback of an increased computing expense.

Migration techniques are also applied for gathers of extremely noisy microseismograms. This technique may be useful for data which may be otherwise impossible to identify events. Examples of migration techniques for locating microseismic hypocenters have been reported by Cole (1990), Chambers et al. (2007), and Fu and Luo (2009).

Migration can be used for data from recording arrays that are deployed on the surface, in wells, or a combination of both. The key is that there must be many well-separated geophones, whether they are of the vertical or 3C type.

The migration technique of Chambers et al. (2008) is summarized in the following paragraphs to indicate the main steps in the 3D migration of 3C microseismograms. Instead of a straight stack, Chambers et al. (2008) compute a semblance traces for each potential source location $\boldsymbol{r_s} = (x_s, y_s, z_s)$:

$$S(\boldsymbol{r_s}, \tau) = \frac{[\sum_{i=1}^{i=N} u_i(t=T_i(\boldsymbol{r_s})+\tau)]^2}{N \sum_{i=1}^{i=N} [u_i(t=T_i(\boldsymbol{r_s})+\tau)]^2}, \quad (2.1)$$

where $u_i(t)$ represents the seismic trace for receiver i, $T_i(\boldsymbol{r_s})$ is the P-wave travel time from the assumed source location to receiver i (calculated using a wavefront construction

method), and N is the total number of geophone stations. The parameter τ accounts for the unknown time of occurrence of the microseism, and is a positive or negative number. The semblance $S(\boldsymbol{r_s}, \tau)$ is calculated systematically, with each of the parameters (τ, x_s, y_s, z_s) varying in small step sizes between set limits. $S(\boldsymbol{r_s}, \tau)$ is smoothed, and the maximum value with respect to the parameter can be plotted in a data cube as a function of the (x_s, y_s, z_s) coordinates.

However, as pointed out earlier, it is appropriate to keep in mind that migration techniques usually have the drawback of a large computing expense and demand data redundancy due to the common approach of summing data along certain curves and computing regression in many approaching steps.

2.3.2 Techniques based on propagation polarization

The full inversion or migration techniques are usually applied to single-component recordings from surface observations. In the case of 3C recordings, which are usually from borehole observations, polarization analysis is a common approach to take advantage of the triaxial information. This introduction is used to estimate the propagation direction of the event wave field that is incident at a receiver site, which is then used to locate the direction to the hypocenter. This distance to the hypocenter is estimated from the difference in the arrival times of the P- and S-wave energies. Techniques with polarization analysis are usually less computationally intensive than inversion or migration methods.

2.3.2.1 Propagation analysis techniques

Polarization analysis of 3C recordings is used to determine the direction of the incoming wave incidence at a given recording station. Polarization analysis techniques are based on the particle motions in the Cartesian coordinates of *x*, *y*, and *z*; the strength of this analysis lies in the ability to discriminate between seismic wave types and/or noises, for their associated particle motions usually have different polarization patterns. I will use this technique to identify the direction of a propagating wavefield.

The quantitative definition of the directionality of partial motion at a given station and the degree of associated rectilinearity depends on the particular implementation of polarization filtering analysis. Two categories, eigenvector/eigenvalue analysis, and hodogram analysis will be described in some generality as following.

- ***Eigenvector analysis***

This group of polarization filters is generally constructed from the mathematically rigorous analysis of the eigenvalues and eigenvectors of the three-component covariance matrix. Some implementations use the real part of the signal (Flinn, 1965; Montalbetti and Kansasewich, 1970; Smart and Sproules, 1981; Magotra et al., 1987, 1989; Aster et al., 1990), where a running average is subtracted from the seismograms before computing the covariance, therefore the averaged estimate is more stable but looses time resolution and favours the higher frequency energy (as there are more high-frequency wavelengths within the time-averaging window). Some constructions use the analytic signal (Vidale, 1986), where the polarization can be measured from the covariance at any point in the seismogram, enabling the identification of multiple arrivals; however, the drawback is a fourfold computational effort required due to the complex algebra.

- ***Hodogram analysis***

The simpler polarization methods, being much less computationally complex than any aforementioned filtering algorithm, work by means of particle motion trajectories or hodograms. Yet, certain efficient noise attenuation schemas are still in high demand to damp strong polarization anomalies at lower SNRs. A hodogram is a parametric plot (with time as the parameter) in the *x*-*y*, *x*-*z*, *y*-*z*, or *r*-*z* planes of the corresponding signed amplitudes of the 3C seismograms (*r* is the radial coordinate in a cylindrical coordinate system). One particular implementation of hodogram analysis targets the first arrival of the P-phase at each channel as it has less contamination than subsequent arrivals.

An implementation of such a technique is proposed in this thesis as an alternative to eigenvector/eigenvalue polarization analysis for the construction of back-propagating rays and intersections. Figure 2.3 illustrates triaxial recordings at a single 3C geophone; the red trace is the simulated source wavelet, and the blue trace is the incident propagation at the receiver of the wavelet at a time of 550 seconds embedded in noise. The cyan, green, and pink traces are the *x*-, *y*-, and *z*- components at a 3C geophone, respectively. Figure 2.4 shows the result of planar hodogram analysis from those 3C recordings in Figure 2.3. Part (a) shows a vertical view of the arriving energy and the azimuthal direction of the incident energy as defined and estimated using least squares. Part (b) shows a horizontal projection of the energy on a vertical radial plane whose azimuth was defined in part (a). The radial dip is also identified. The combination of the analysis in (a) and (b) provide the direction of the incident energy.

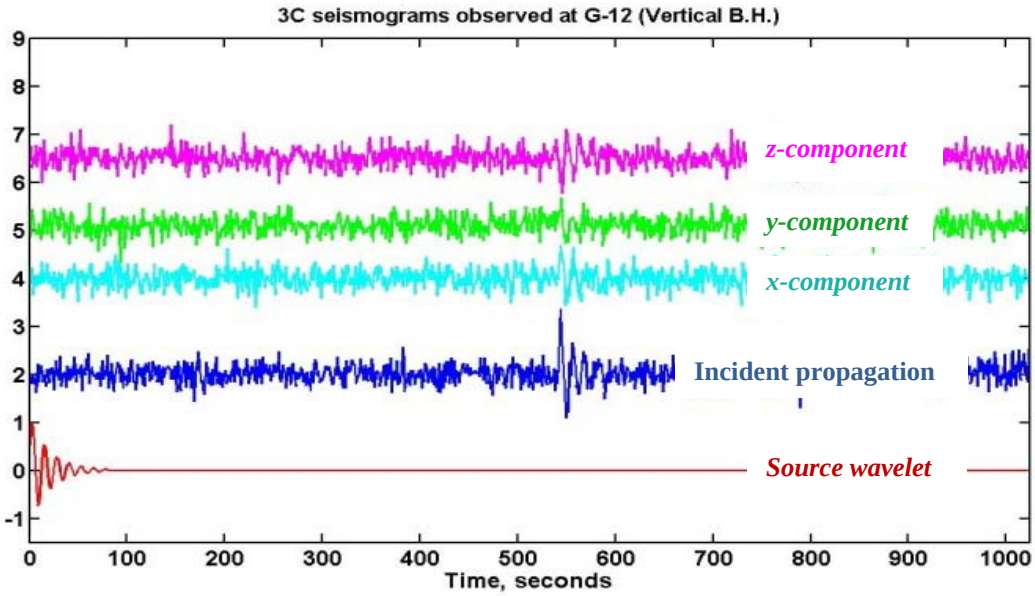

Figure 2.3: 3C data synthesis at a single recording site.

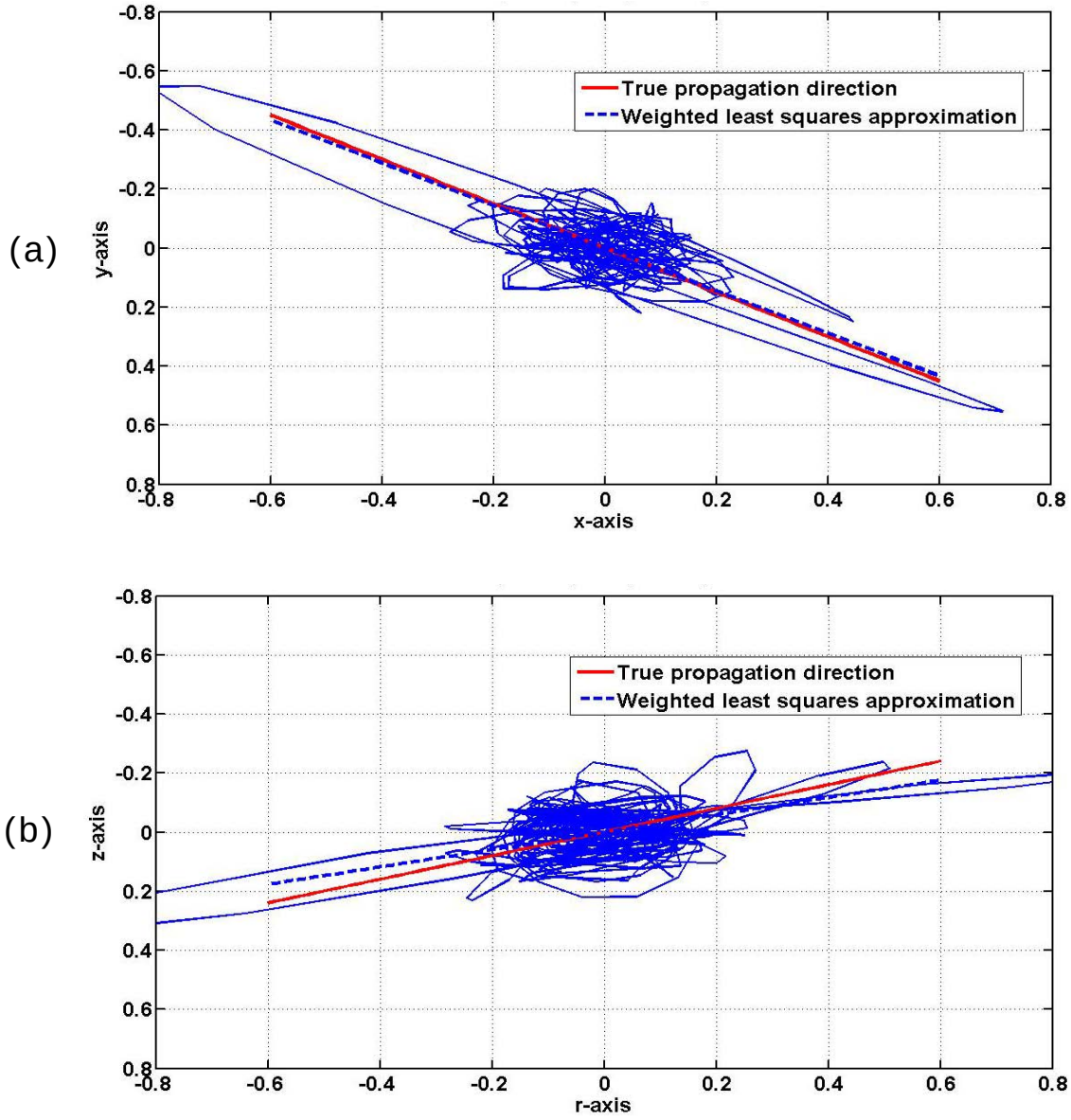

Figure 2.4: Hodogram polarization analysis (2D). (a) The azimuth estimation and (b) the radial direction estimation are resulted from the 2D approach of hodogram polarization analysis on data in Figure 2.5.

As a part of hodogram analysis, polarization analysis has been used to enhance highly polarized portions of the signal by rotating the seismic traces usually recorded in the geographic directions (North-East-Depth, or N-E-Z respectively) into the incident ray coordinate system. In this ray coordinate system, the particle motion in the direction of

the ray is referred to as the P-wave (primary) and particle motion perpendicular to the ray path is referred to as the S-wave (secondary). This rotation isolates the P-wave arrivals from S-wave arrivals and enhances the SNRs of both, thus improving onset determination.

In the following section, the difference is the arrival times of the P- and S-wave energy will provide an estimate of the distance between the source and receiver, to complete the location of the source.

2.3.2.2 Location methods based on propagation direction

- ***τ_S-τ_P methods***

Albright and Pearson (1982), Ruud et al. (1988), and Saari (1991) discussed the simplest case, in which a single 3C geophone records a microseismogram with P and S arrivals. Assuming a homogeneous velocity earth, the difference between the P and S picked times (τ_S - τ_P) can be used to find the distance *R* between the geophone and the source:

$$R = (\tau_S - \tau_P)/(1/V_S - 1/V_P) \tag{2.2}$$

where *Vp* and *Vs* are the P- and S- wave velocities, respectively. The 3C seismograms were used to estimate the azimuth and dip angle of the propagation vector (which in a homogeneous velocity field points towards the source). Albright and Pearson (1982) plotted hodograms based on the 3C seismograms to obtain the azimuth and dip angles. Ruud et al. (1988) and Saari (1991) estimated these directions using a more complicated maximum-likelihood analysis (Christoffersson et al., 1988). The distance and directions from the recording geophone effectively located the microseismic source.

Rutledge et al. (1998) employed up to three widely-spaced triaxial geophones in their study of production-induced microseismicity in an oil reservoir. For data recorded on one or two geophones, they used the (τ_S - τ_P) method to find the distances from the geophones to the microseismic source, and applied the eigenvector analysis of Flinn (1965) to obtain propagation directions. Velocities for horizontal layers were initially obtained from well logs. For data recorded on three geophones, a nonlinear-optimization (inversion) routine was used jointly to find the hypocenter coordinates and to refine the velocity model.

- ***Back-propagation methods***

Using only the P-wave data, the polarization method is used to define rays from the receivers to the estimated source location. In a 2D radial plane, the intersection of the rays provides an estimate of the source location.

In a 3D volume the rays may not intersect, so the closest point between the two rays is used as an estimate of the source location. Figure 2.5 shows the triaxial recordings of 20 receivers in a horizontal well. The well, as shown in Figure 2.6, is the pink one of three wells color coded by triangles. Rays estimated using the polarization method is drawn in Figure 2.6a with the legend shown on the map view. The closest points between pairs of these rays are illustrated in Figure 2.6b.

As shown in the legend of Figure 2.7, the estimated location indicated by the black star (i.e. x=406 m, y=295 m, and z=2160 m) is very close to the true setting of coordinates indicated by the red star (i.e. x=400 m, y=300 m, and z=2150 m). The standard deviations along the triaxial traces are very low.

Note that the hodogram method does not require the exact arrival time of the event as the largest amplitude are used to define the direction. A reasonable window around the event will reduce the clustering of noise about the origin.

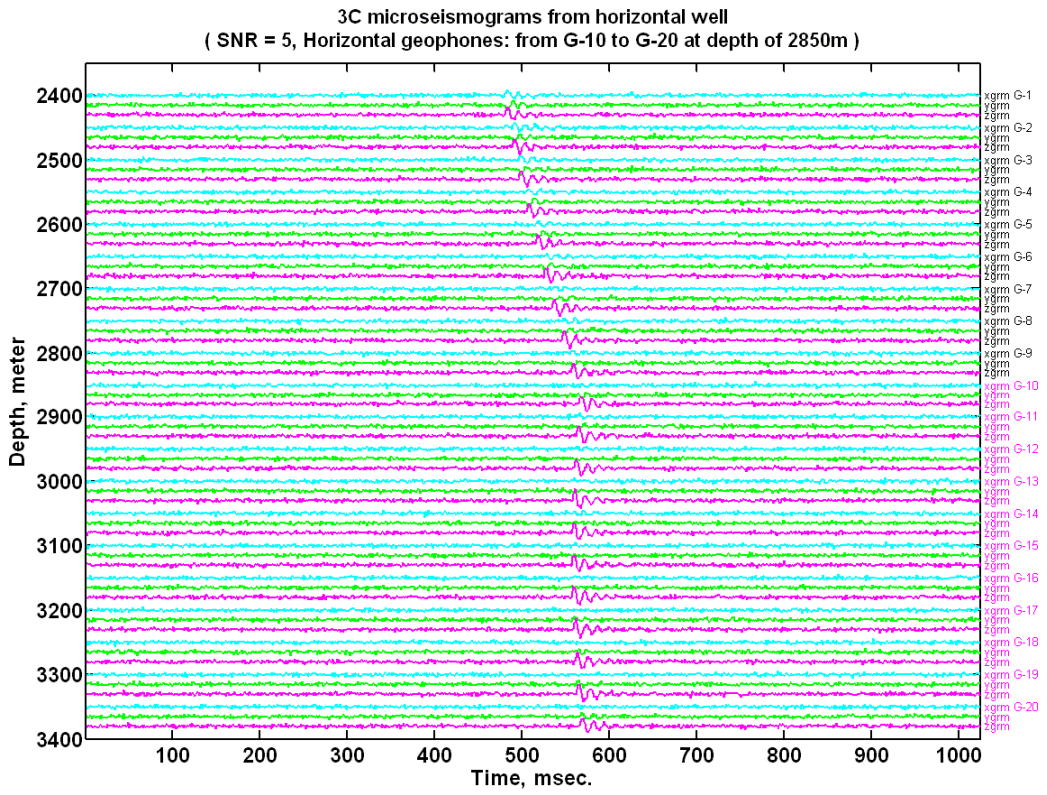

Figure 2.5: synthetic 3C microseismograms obtained at SNR=5 in a horizontal well with a vertical part from G-1 to G-9 (black indexes) and a horizontal part from G-10 to G-20 (pink indexes) of total 20 geophones with 50 meters of displacement.

(a)

(b)

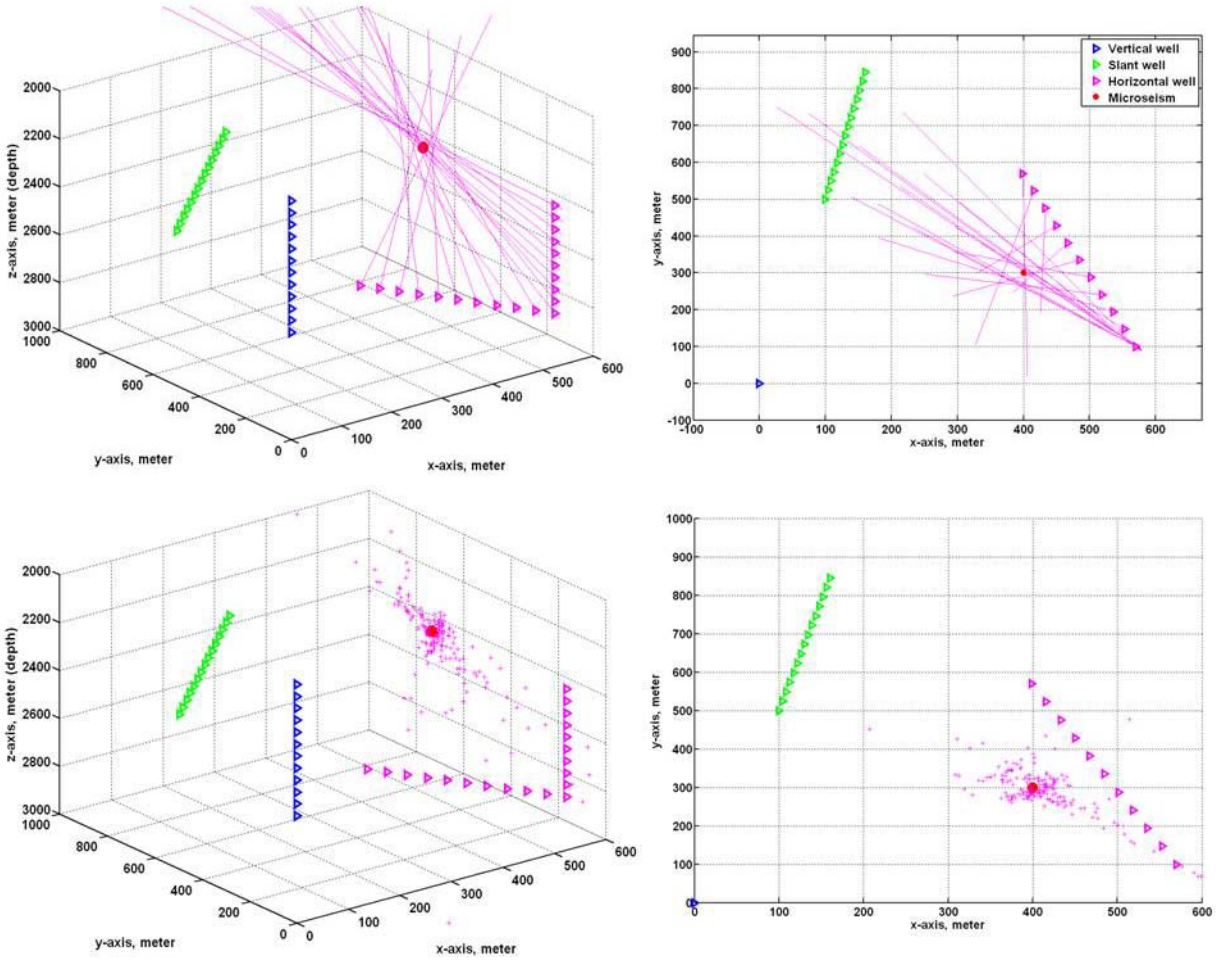

Figure 2.6: Hypocenter location by back-propagation analysis (Phase 1 and Phase 2). With a single horizontal well (pink triangles) monitoring of single microseism (red dot), the method derives (a) propagation raypaths (pink lines) in Phase 1 and (b) nearest points of mutual raypaths (pink crosses), in Phase 2, the 3D view on the left and the map view on the right.

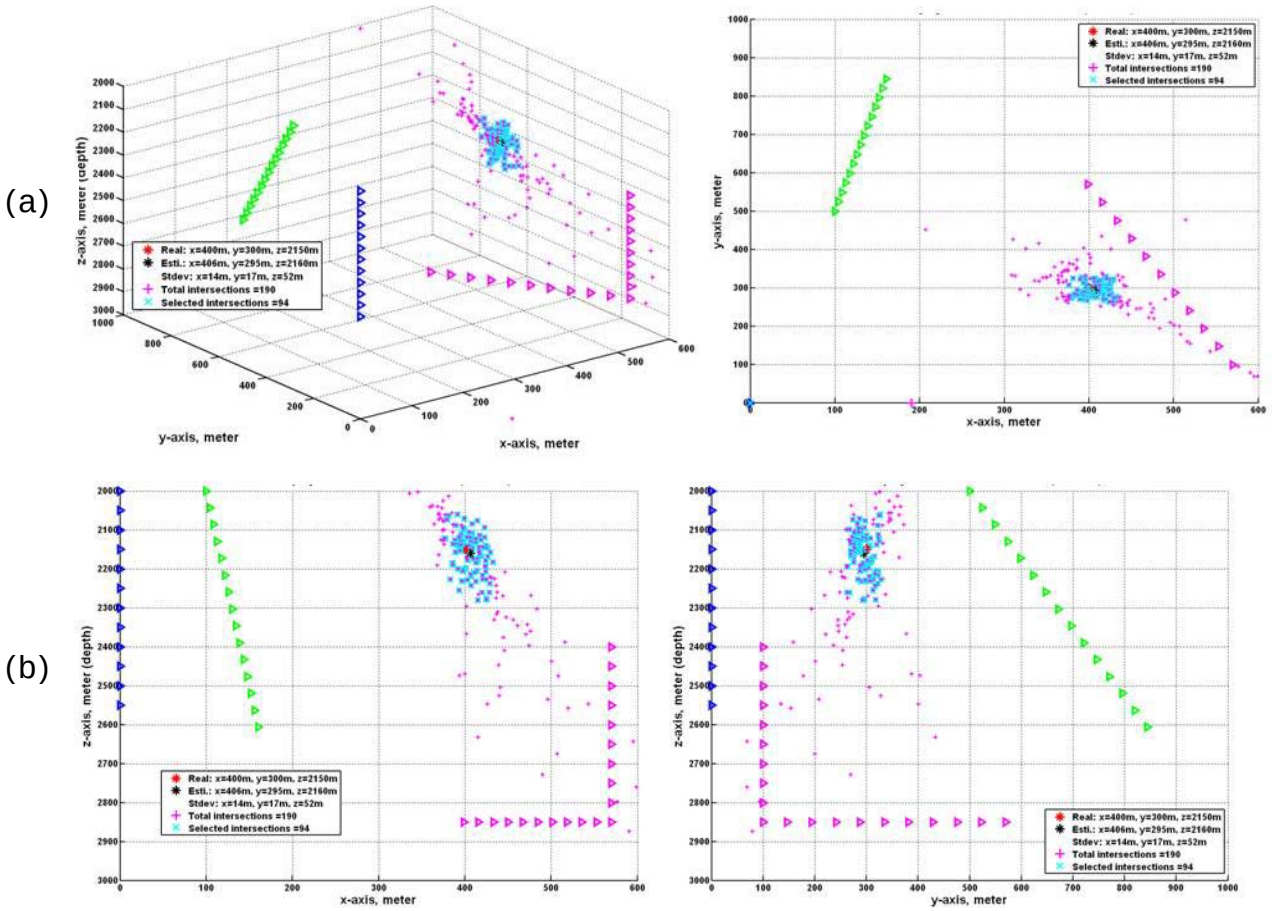

Figure 2.7: Hypocenter location by back-propagation analysis (Phase 3). Based on results in Figure 2.6, the method estimates the hypocenter location in Phase 3 from the clustering points (cyan crosses) from the original ones (pink crosses) (a) 3D and map views and (b) x-z section and y-z section views, on the left and right respectively.

2.3.3 Other techniques

Pavlis (1992) discussed the concept of relative hypocenter locations relative to a single reference hypocenter that is reliably located. This reference point is important, because it is the benchmark against which the accuracy of all other locations can be gauged. There is an analogy that can be made with surveying. In surveying, we can measure positions relative to a local benchmark with very high precision, even though the benchmark's absolute coordinates may not be known precisely. In the same way, the

absolute locations of a set of earthquake hypocenters may be rather imprecise, but their positions relative to a single hypocenter that serves as a control point may be determined more accurately. The reference hypocenter can be chosen to be the mean or centroid value of a group of hypocenters determined from multiple independent estimates for a single event, or for a group of events that are known to be closely clustered spatially such as an initially earthquake and its series of closely-followed aftershocks (Pavlis, 1992). An event better control location would be the explosive charge used in the well fracturing process.

For multiple receivers in a homogeneous and isotropic velocity field, Bancroft *et al*. (2009) have reported several analytic techniques that locate hypocenters using only the clock arrival times. One method involves finding the common tangent point of four Apollonius spheres whose radii depend on four picked arrival times and their offset time from the occurrence of the microseism. Another involves solving four quadratic arrival time equations with the three hypocenter coordinates (x_s, y_s, z_s) and the offset time as the unknown parameters. The details can be found in Bancroft et al. (2010).

2.3.4 Chapter summary

To summarize, three-component seismograms from one or more recording stations are used in passive microseismic monitoring to locate the hypocenter of the seismic source (an earthquake or an induced rock fracture). The 3C seismograms are analyzed to obtain propagation angles (azimuths and dip angles) to the event and the distance using the P and S arrival times. Various location schemes are applied to these angles and arrival times are to estimate the hypocenter location.

In contrast to the 3C method, first arrival times of the P- or S-wave energy are used to back propagate the direction to a microseismic event.

The earth velocity model needed for hypocenter location is either assumed, determined from well logging or calibration surveys, or results from a joint-inversion technique that simultaneously determines hypocenter coordinates and velocity parameters. Hypocenter location is fundamentally a triangulation process, so that the more widely-spaced the geophone locations are relative to the distance to the source, the more accurate the location coordinates will be.

Chapter Three: Energy ratio analysis for arrival time picking

The primary goal of microseismic monitoring is to map hypocenter locations. Arrival time-picking for direct P and/or S events is commonly a critical first step leading to this goal.

A passive seismic monitoring system may record files of microseismograms every 15 seconds for days, months, or even years. The resulting dataset may consist of tens or hundreds of thousands of microseismic traces. Rock fracturing usually emits much weaker energy than what is generally present in a conventional seismic survey; hence, the noise background is relatively much higher in microseismic monitoring applications.

Under these conditions, a time-picking method that is fast, automatic, and accurate in the presence of strong random noise is essential for any algorithm and implementation of real-time microseismic analysis.

In this chapter, various energy ratio (ER) formulations are first analyzed and compared for their efficacy of arrival detection and time-picking accuracy at various noise levels. The most sensitive ER variant are chosen and named as modified energy ratio (MER) as the seismic event trigger proposed in this thesis.

The short-term-average (STA) to long-term (LTA) ratio analysis is then introduced and compared with MER analysis. Since both global earthquake and microseism monitoring use the standard STA/LTA method to identify the presence of valid events and pick the arrival times (Saari, 1991; Withers et al., 1998).

STA/LTA, MER, and other ERs are all energy transient triggers but in different formulations. It should be emphasized that Chapter 3 herein only focuses on the efficacy

of various event triggering formulations themselves, regardless of any other joint process, for example, noise attenuation as detailed next in Chapter 4, which could further improve the time-picking accuracy.

3.1 MER analysis

MER is a modified version of the basic energy ratio (ER) formulation,

$$\mathrm{ER}(i) = \sum_{j=i}^{i+L} g(j)^2 \,/\, \sum_{j=i}^{i-L} g(j)^2, \tag{3.1}$$

where $g(j)$ is the seismogram value at time index j, i is the testing point index, and L is the length of the energy-collecting window preceding and trailing the test point. This energy ratio is illustrated in Figure 3.1a. Figure 3.1b illustrates the STA/LTA ratio that will be discussed later.

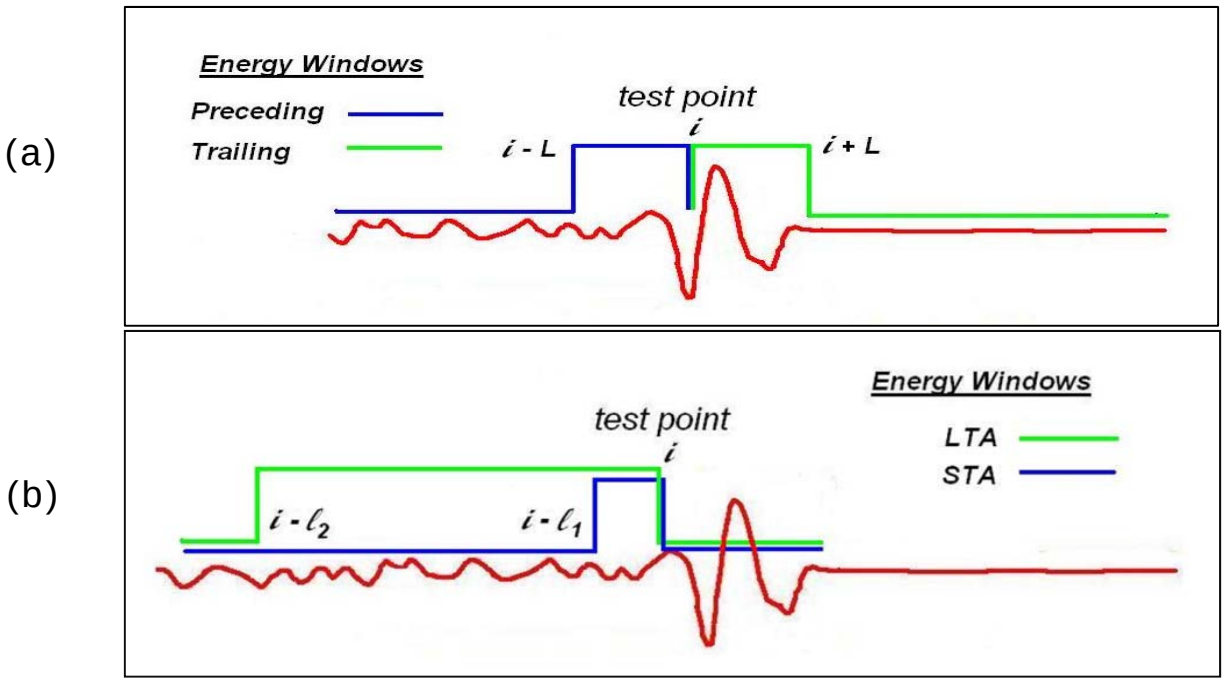

Figure 3.1: Energy window definitions for (a) MER or ER methods and (b) STA/LTA methods.

In general, the energy window L should be long enough to cover the dominant period of the target's P-arrival, but short enough not to cover the first following arrival of any phase. Based on the extensive testing on simulated microseismograms, two to three cycles of the source wavelet or the dominant period of a seismic arrival are found to be appropriate as the energy-collecting window length for picking P-arrival time. The energy-collecting window length L is also a critical attribute for all ER variants as following. The term energy is used here as a generic term referring to amplitudes modified in one of the following three ways:

$$er1(i) = ER(i) \cdot abs(g(i)) \ , \tag{3.2a}$$

$$er2(i) = ER(i) \cdot [abs(g(i))]^3 \ , \tag{3.2b}$$

$$er3(i) = [ER(i) \cdot abs(g(i))]^3 \ . \tag{3.2c}$$

The purpose of research on these variants of the basic energy formulation is to find the most sensitive version as an alternative to the commonly used STA/LTA formulation.

Figure 3.2 shows the sensitivity testing results from synthetic data with random noise imposed at different levels. Notice that all three ER variants defined in the above formulations improve the sensitivity to the onset of a seismic arrival. Also notice that *er3(i)* is just the cube of *er1(i)*, but the plot of *er3(i)* shows a much clearer spike. Gaussian random noise was added to the transient signal to produce SNR's of 10, 5, and 2.

The *er3(i)* method was chosen for general time-picking on the basis of the results of Figure 3.2. In the rest of this thesis, the MER acronym will refer to *er3(i)*.

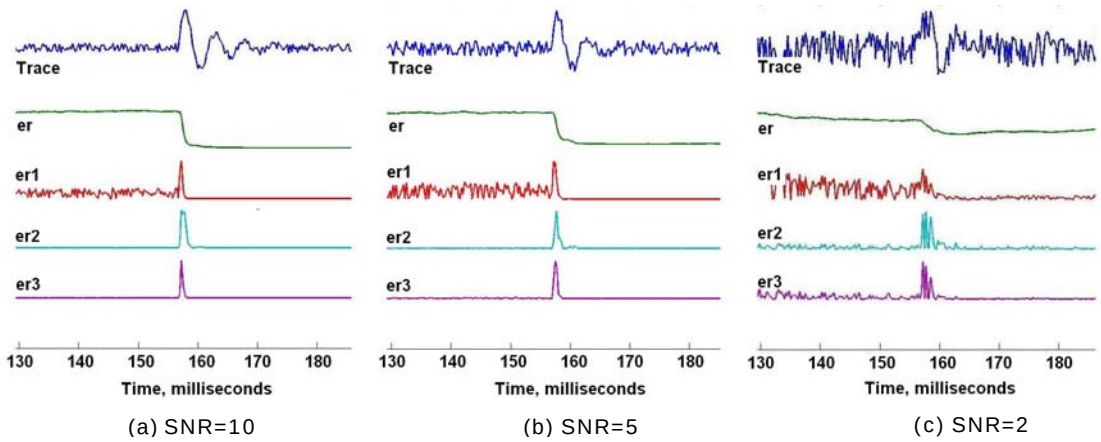

Figure 3.2: Sensitivity tests of various ER formulations. These plots indicate that the er3 definition corresponding to Equation 3.2c may be the most sensitive ER variant to use for time picking on microseismograms with low SNRs.

3.2 STA/LTA analysis

The STA/LTA method is commonly used by industry, and like the MER with the basic ER formulation and the variants, there exist various modifications of the standard STA/LTA formulation as well, such as delayed STA/LTA and recursive STA/LTA (Withers *et al*., 1998); the focus herein is only on the standard version.

Equation 3.3, 3.3a, and 3.3b define the energy ratio formulation representing the standard STA/LTA analysis approach:

$$ER(i) = \frac{STA(i)}{LTA(i)}, \tag{3.3}$$

$$STA(i) = \sum_{j=i}^{i-l_1} g(j)^2 \ / \ l_1 \ , \tag{3.3a}$$

$$LTA(i) = \sum_{j=i}^{i-l_2} g(j)^2 \ / \ l_2 \ , \tag{3.3b}$$

where *g(i)* represents the time series of a seismogram, l_1 in $STA(i)$ represents the length of a short-term window, and l_2 in $LTA(i)$ represents the length of a long-term window with $l_2 > l_1$, as shown in Figure 3.1(b).

The average energies in the short- and long- term windows, namely, the STA and LTA windows, are preceding the time index *i*, whereas in the MER analysis, one window is preceding and another window is following the time index *i*.

The length of the LTA energy collection window l_2 is five to ten times the length of the STA energy collection window l_1, which needs to be on the order or two to three times the length of the dominant period of the seismic arrival (Munro, 2004).

Notice that the standard STA/LTA could be an estimate of the signal-to-noise ratio; with the STA representing the signal energy, and the LTA representing the background noise, but not the MER as it does not represent the background noise.

3.3 Noise tolerance tests via picking first *P*-arrivals

Initially, *P*-arrival picking was evaluated employing both the MER and standard STA/LTA analysis on the same trace or set of data. The original data was from a casing perforation shot; as the data quality was very good. Gaussian random noise was added to the original data, as shown in Figure 3.3. The original field data is denoted as SNR=100, and the noisy modification as SNR=3.

Figure 3.3 demonstrates first arrival picking on a single trace using both STA/LTA ratios (top red trace) and MER ratios (bottom green trace) are calculated at a noisy trace and a clean trace. The noisy trace (SNR=3) was created by adding synthetic random noise to the clean trace (SNR=100). For the clean trace, the MER and STA/LTA methods both give an arrival time at the first break. For the noisy trace, both the STA/LTA and MER picks occur at a later time.

It can be observed that the time pick using STA/LTA ratios occurs at the maximum of the rising slope of the red ratio trace, while the time pick using MER ratios occurs at the peak of the green ratio trace.

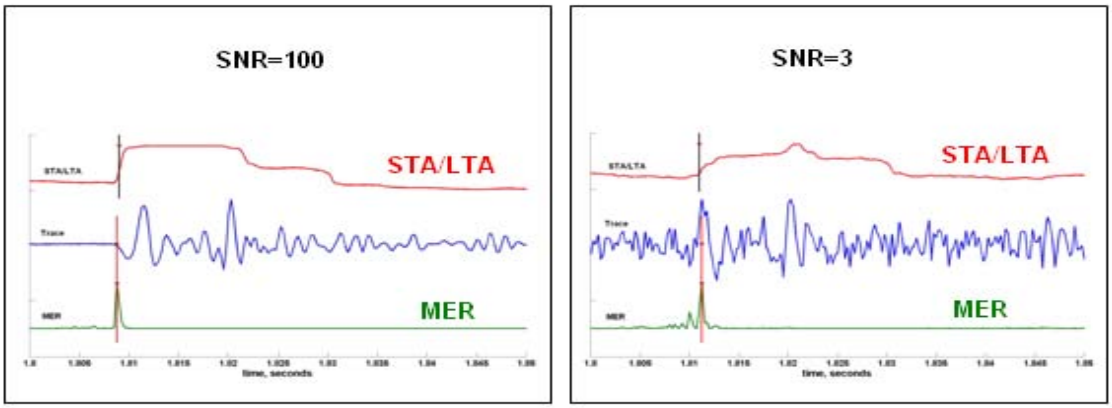

(a) (b)

Figure 3.3: Demonstration of first arrival time picking with STA/LTA and MER ratios on (a) a clean trace and (b) a noisy trace.

This advantage of MER over STA/LTA is further supported by the statistical results shown on Figure 3.4. Time picks were produced for noisy traces using 100 trials for the three SNR levels (20, 5, and 3) using different levels of Gaussian noise. For each trace and for each run, the noisy time picks were subtracted from the corresponding noise-free picks. The standard deviation of the 100 time differences for each trace and for each SNR level was calculated and plotted in Figure 3.4 for both the MER and STA/LTA methods. Large standard deviations mean that many of the 100 picked times on noisy data are significantly different for the noise-free picks. Figure 3.4(b) shows that at the SNR = 5 level, the STA/LTA method begins to pick many wrong arrival times, whereas the MER method still produces many picks that have zero or very small differences from the noise-free picks. Figure 3.4c shows that at the SNR level of 3, both

methods result in many wrong picks, but the MER picks are, on a statistical basis, closer to the noise free-picks. The conclusion drawn from the plots on Figure 3.4 is that, for noisy seismic traces, MER time picks are more consistent and reliable than STA/LTA picks.

In these tests, the MER method performed about three times faster than the STA/LTA method. The increased speed is due to the fact that the LTA energy window is usually five to ten times longer than each MER energy window. Both methods perform only arithmetic operations, and fast filtering techniques could be used to improve the computational speed.

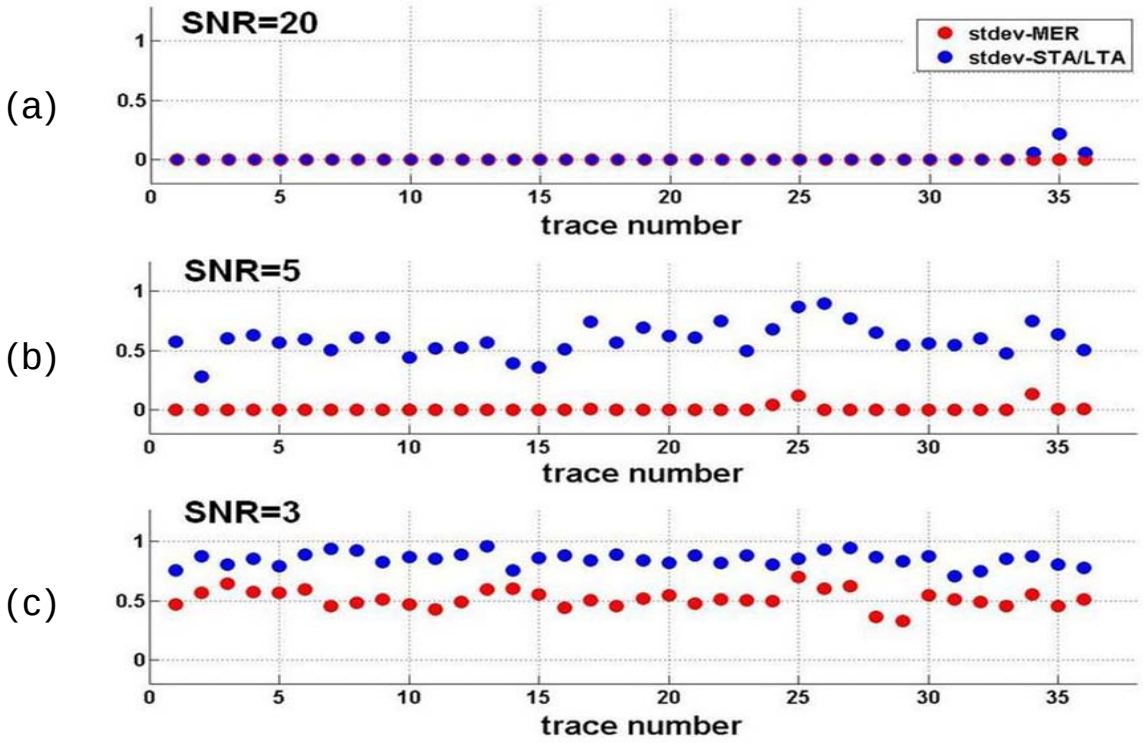

Figure 3.4: Standard deviations for arrival time differences between noisy and noise-free microseismograms. The plots show that, for noisy seismograms, the MER time picks are more consistent than the STA/LTA time picks.

3.4 Noise tolerance tests via picking multiple arrivals

The first arrival time-picking algorithm is modified to accommodate multi-arrival picking as microseismograms often contain both *P*- and *S*- arrivals. Then MER analysis can also be evaluated by associating with the solution of multi-phase and/or multi-arrival time picking.

Figure 3.5 indicates how the multi-arrival time picking solution can handle multiple events as noise levels increase, along with the MER trigger.

Figure 3.5 shows that for SNRs greater than about 3.5, the arrival times for well-separated coherent events are picked accurately, while for SNRs less than 3.5, more and more outliers begin to appear. At a SNR=3.5, as shown in Figure 3.5c, multiple arrival time-picking in both P- and S-phase also work appropriately.

Notice that the MER window length might have to be adjusted as the time interval between the first P-arrival and the following S-wave may overlap. The time interval between the S-arrival and the following event should be considered as well, to control the energy window adjustment for the geometry of a particular application.

(a)

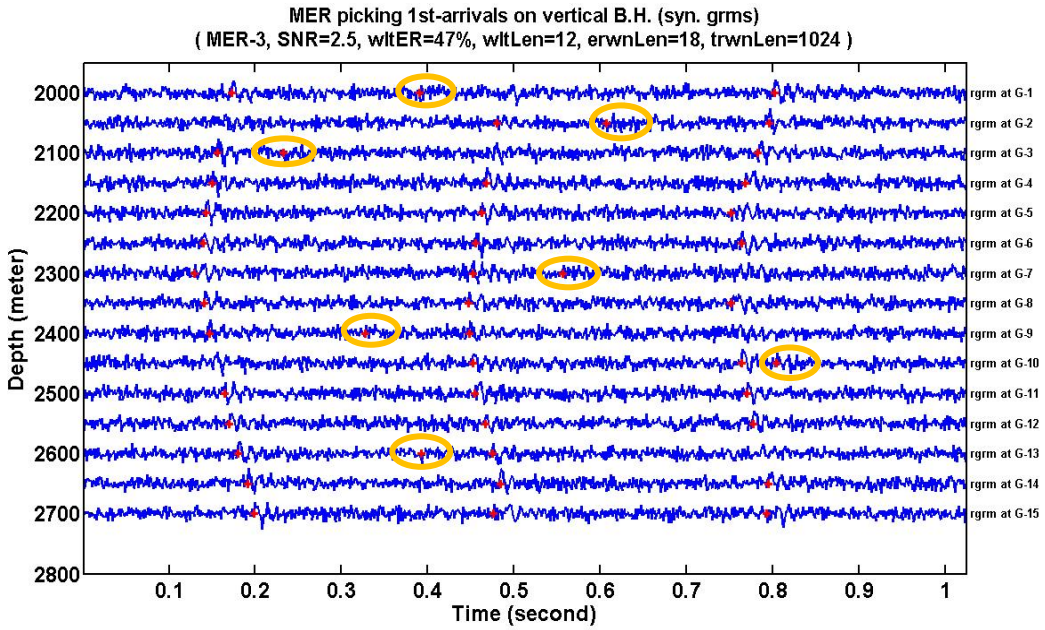

(b)

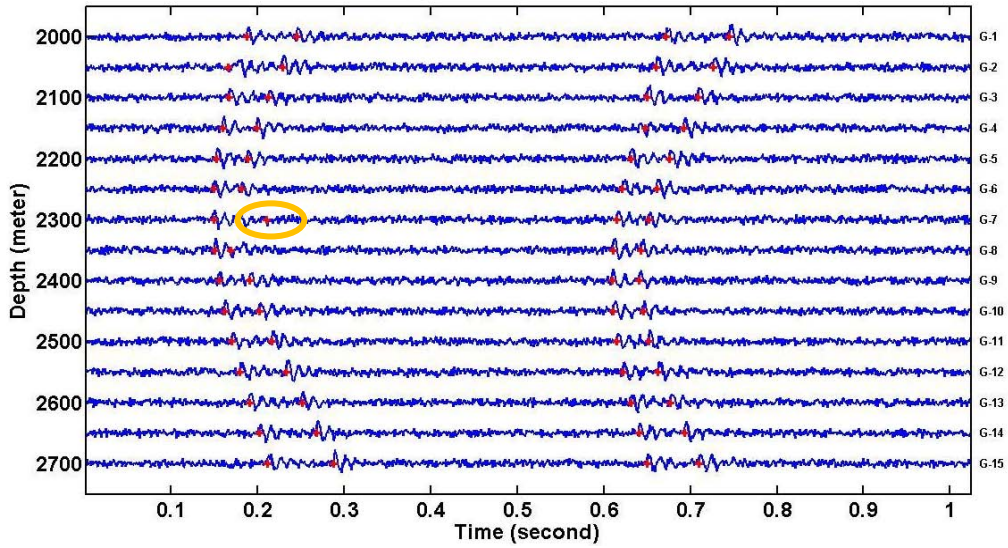

Figure 3.5: MER time picking of multiple arrivals in P-phase and/or S-phase with different levels of Gaussian noise: (a) SNR=2.5; (b) SNR=3.5.

3.5 Synthetic seismograms generation for various geometries

In Chapters 3 and 4, source wavelets are based on Equation 3.5, and were generated with f = 80Hz or 200Hz, and k = 50.

$$x(t) = [\, A \cdot cos(2\pi ft) + B \cdot sin(2\pi ft)] \cdot exp(-kt) \;\; , \tag{3.5}$$

There are many ways to define SNR when we compare a transient response with a steady state signal such as noise. I choose to define the transient signal using the root mean square (RMS) energy in a window that is approximately three times the wave length of the dominant frequency and the noise using the conventional RMS method. Notice that this an amplitude ratio, typical in geophysics, and not the power or energy ratio used in other disciplines.

Figure 3.6 illustrates a synthetic data set of both the incident trace (dark blue) and the associated triaxial components at a single 3C geophone. It is used for MER testing in Chapter 3 and for hodograms and back-propagation analysis in later chapters, respectively.

P- or S-wave arrival times between a microseismic source and geophones were calculated by ray-tracing through a homogeneous and isotropic velocity model. For a particular geophone, a base synthetic trace (1024ms long and sampled at 1ms) was produced by convolving the source wavelet with a delta function located at the calculated arrival time. The amplitude of the base trace was scaled to account for spherical spreading. The *x*-*y*-*z* components were then derived from the base trace by applying the direction cosines of the propagation vector between the microseismic source and the geophone.

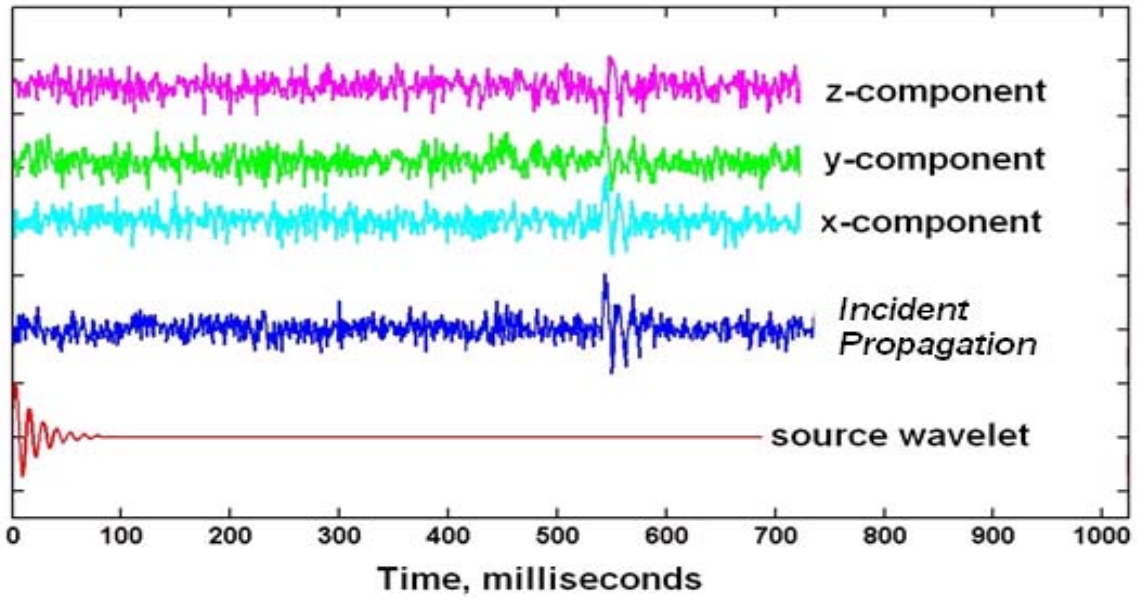

Figure 3.6: Synthetic 3C data generation at a single geophone with Gaussian noise imposed on the incident trace and each of triaxial recording traces randomly and independently at run time.

The 3D model illustrated in Figure 3.7 is used extensively in the later chapters, and contains a 3D representation of a microseismic source monitoring scenario with three wells. They are a vertical well, a slanted well with varying dips and azimuths, and a third well that contains a vertical portion and horizontal portion. I will refer to the third well as a horizontal well. Figure 3.7b is a map view of the wells showing projections of the wells in the *x*-*y* plane. Figure 3.8 shows section views of the x-z plane and the y-z plane. The media will be isotropic and homogenous with a P-wave velocity of 4500m/s.

(a)

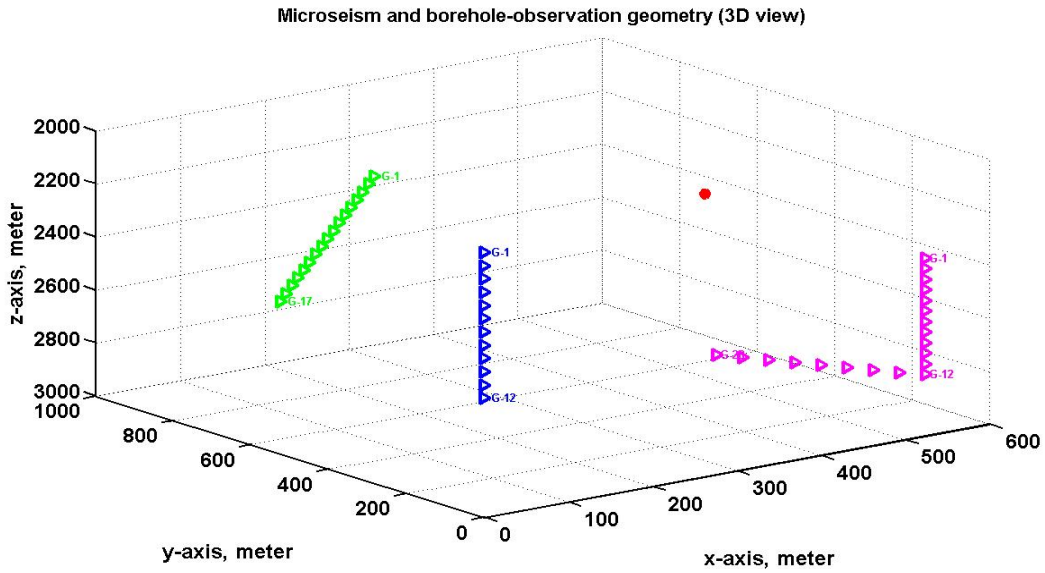

(b)

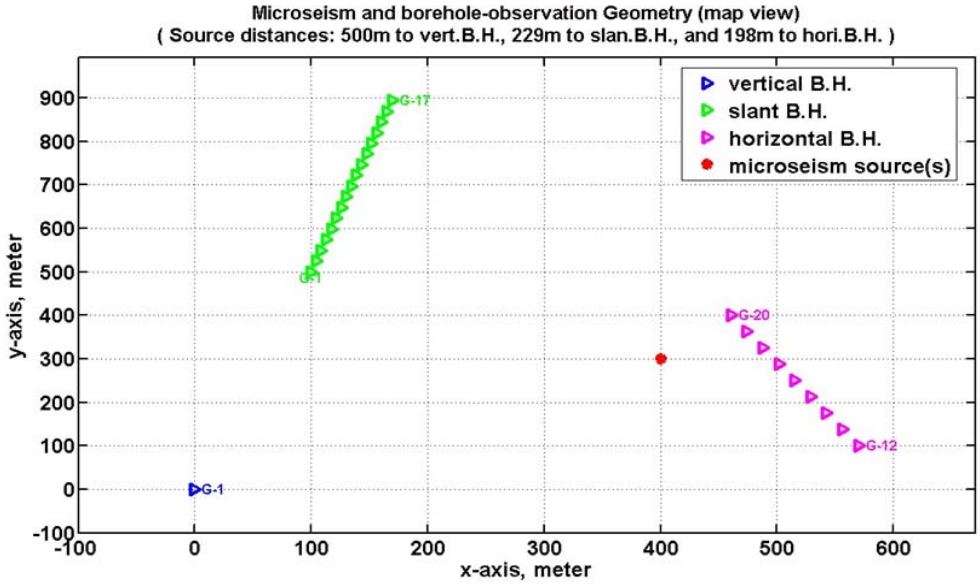

Figure 3.7: (a) The 3D geometry of multi-well monitoring of a single microseismic hypocenter, color-coded by the legend in (b) the map view.

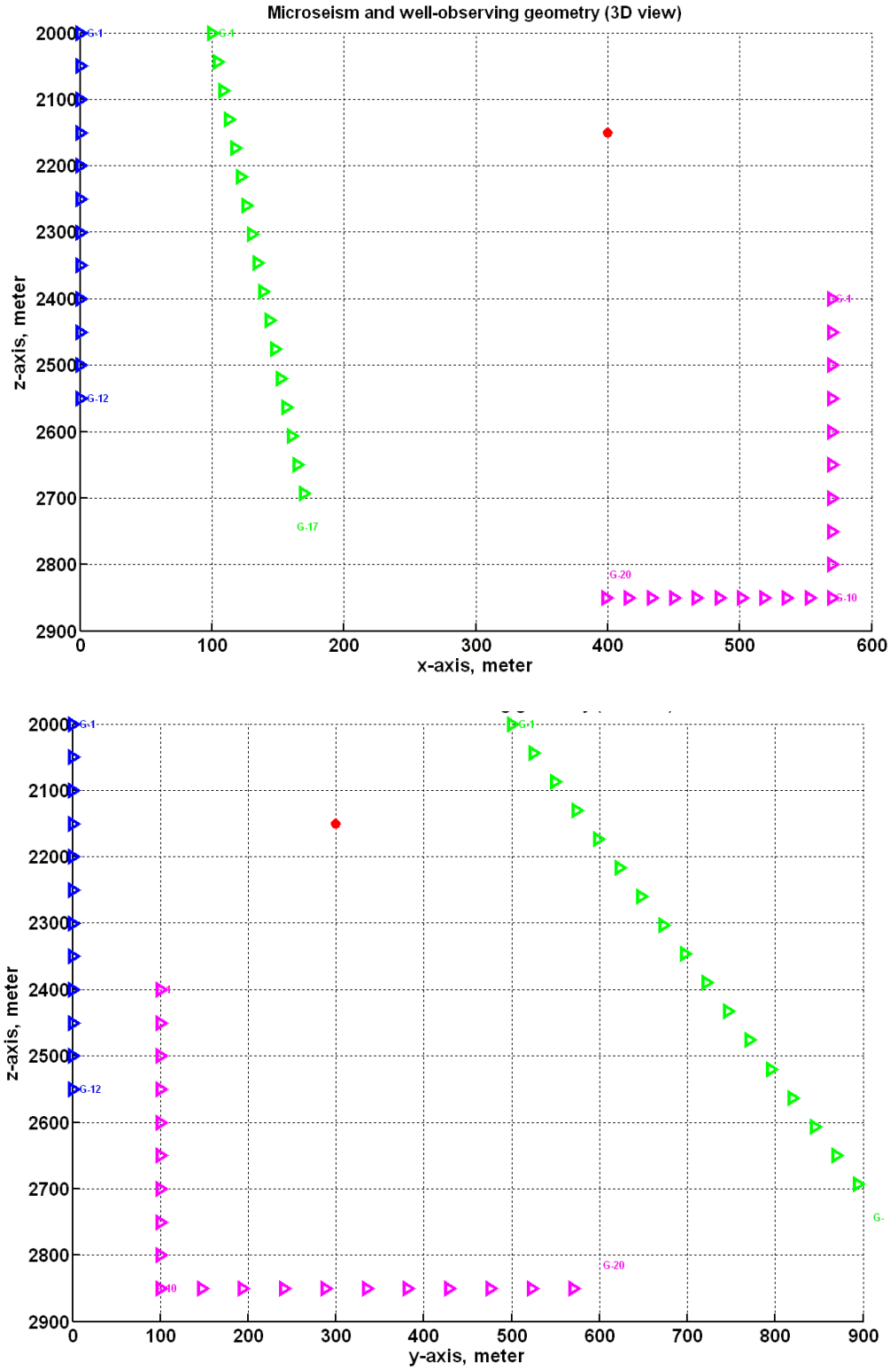

Figure 3.8: Section views of Figure 3.7

Synthetic microseismograms of a single arrival will be obtained in all 3 wells. Figure 3.9 show the result of data without any noise imposed. Three traces cyan, green and magenta are shown for each of 3C geophones in the three wells.

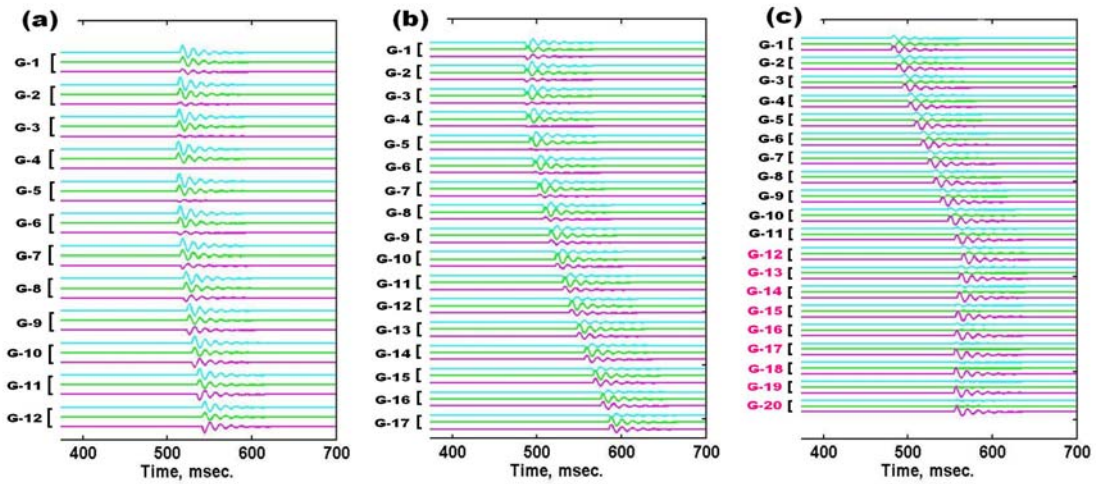

Figure 3.9: Noise-free 3C seismograms obtained with the simulated scenarios in Figure 3.11: (a) vertical well; (b) slanted well; (c) well with vertical and horizontal legs, where cyan traces are for x-components, green traces for y-components, and pink traces for z-components.

Seismograms of multi-arrivals and multi-types were also needed for testing the MER time picking ability on them in Chapter 3, although it was not a main focus in this thesis. Figure 3.10 shows the scenario of 2 microseismic sources emitting both P- and S- waves with even time of delay of 451 milliseconds, and Figure 3.11 shows the entire sets of 3C microseismograms generated in the three wells, with Gaussian noise at the level of SNR=8, using 4500 m/s and 3600 m/s for the P- and S-waves, respectively.

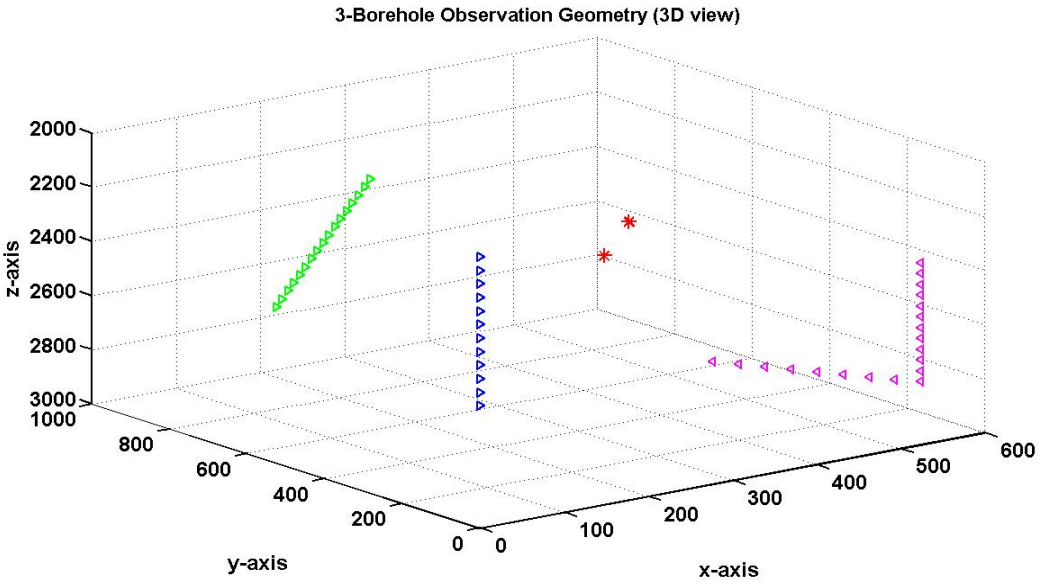

Figure 3.10: Simulating 3D geometry of multi-well monitoring for 2 microseismic sources (red stars). Three types of wells are color coded same as the legend of Figure 3.7.

In each recording file, it is likely that there is only noise but any arrival, and unlikely that there are more than two arrivals. However, the collection of microseismic events, as illustrated in the example of Figure 3.12 show a distribution of estimated locations that indicate a fracturing orientation. This distribution is of high interest to geologists and geophysicists, though it is not a subject of the research presentation herein.

(a)

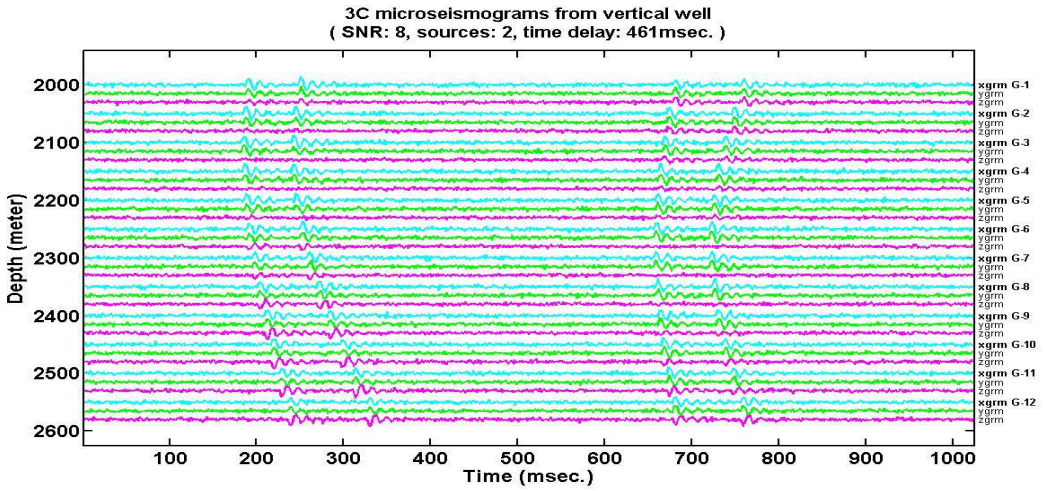

(b)

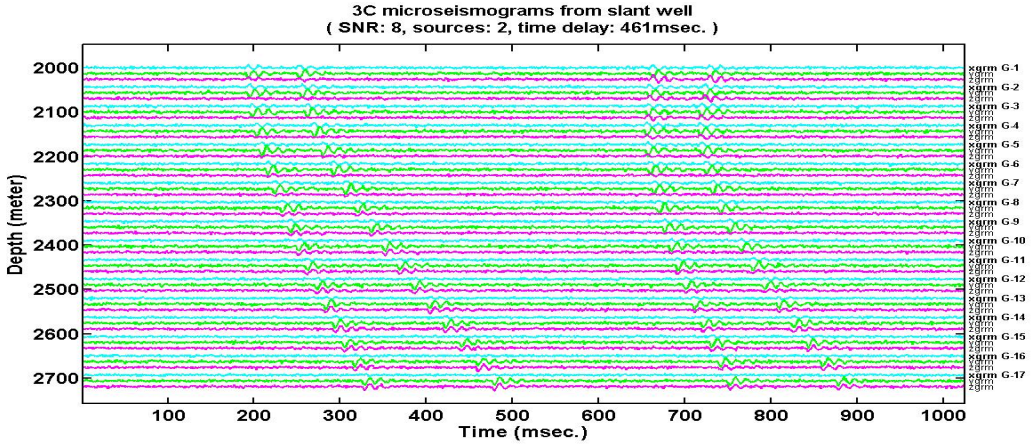

(c)

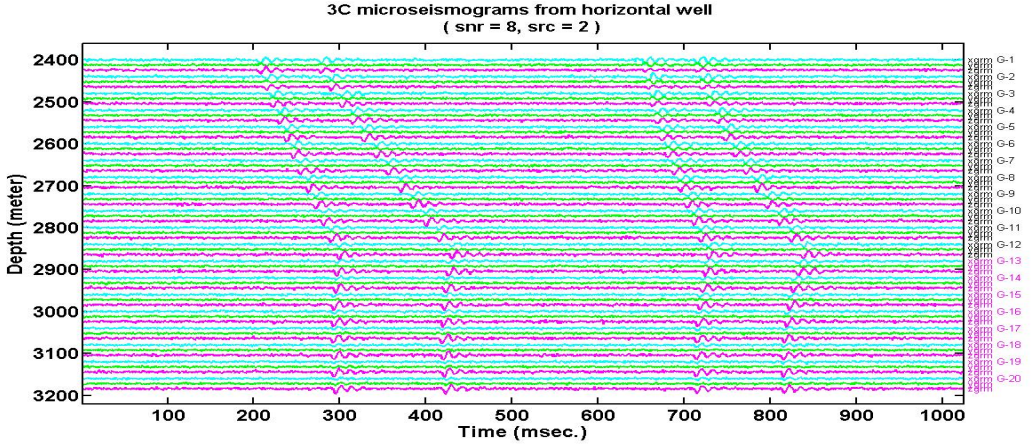

Figure 3.11: 3C data simulated with scenarios shown in Figure 3.10 at a GAUSSIAN noise of SNR=8: (a) a vertical well, (b) a slant well, and (c) a horizontal well, monitoring 2 microseismic sources that emit both P- and S- waves with event delay of 451 milliseconds.

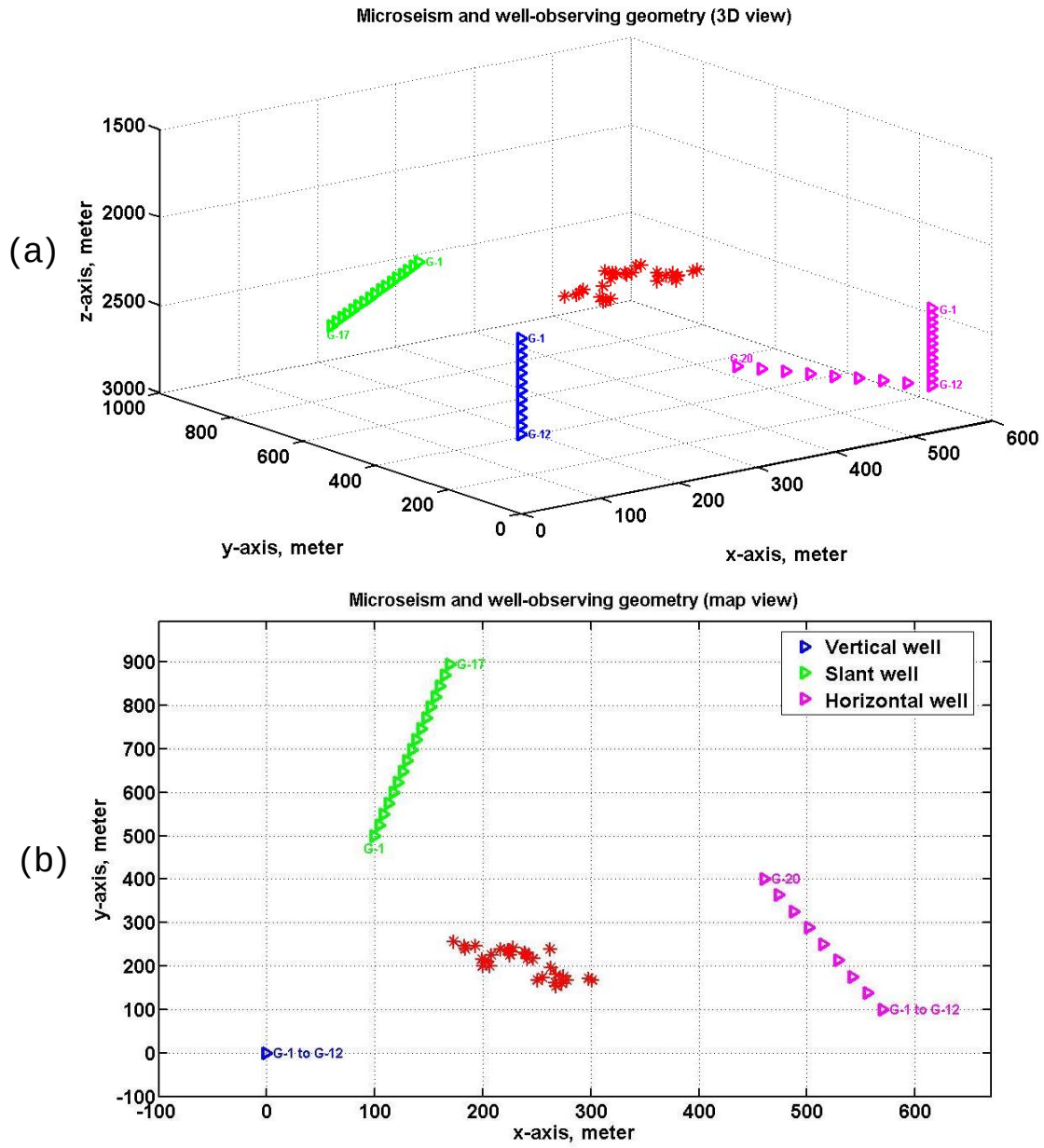

Figure 3.12: Multiple microseismic sources and the fracturing orientation.

As mentioned in Chapter 2, passive microseismic monitoring in hydrocarbon reservoirs is most likely through borehole arrays which contain far fewer geophones than regional seismic survey networks. However, monitoring the hydraulic fracture growth from the surface of larger array apertures increases the subsurface coverage. Stacking over a large number of stations effectively cancels the surface noise and enables seismic

signal detection at levels that are comparable to downhole techniques (Laking and Duncan, 2006). Therefore, simulating the surface survey of the underground microseisms induced by the hydraulic treatment also has been investigated. Figure 3.13 and Figure 3.14 show one of such cases in geometry setting.

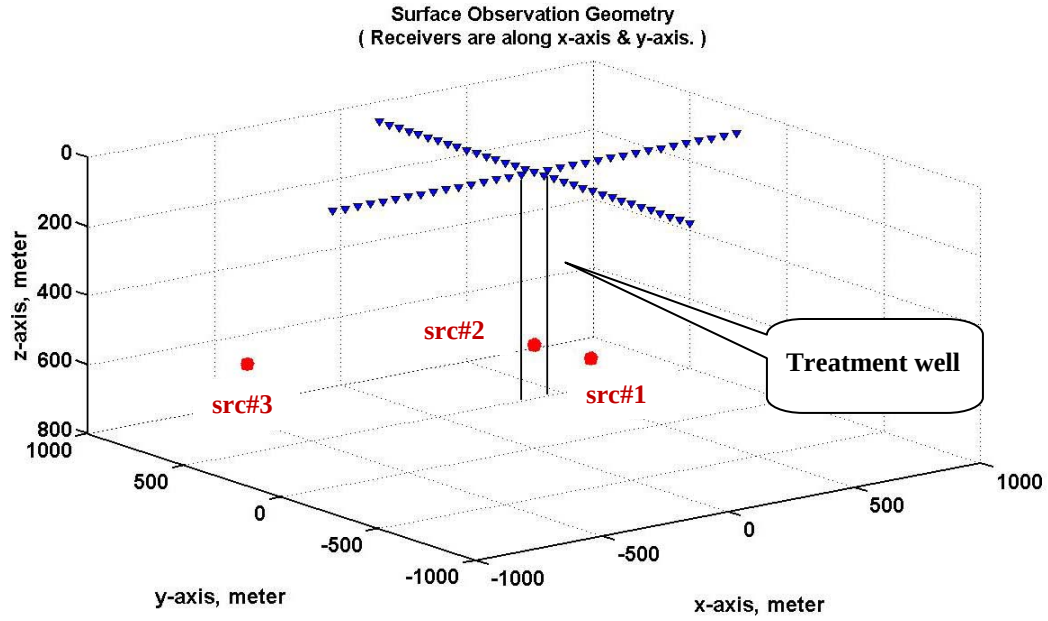

Figure 3.13: (a) the 3D geometry of surface monitoring arrays of geophones (blue triangles) and hydraulic microseismic hypocenters (red dots) underground denoted as src#1, src#2, and src#3.

The surface geophones are arranged in two cross lines: arm #1 and arm #2 along x-axis and y-axis respectively, with 33 geophones displaced with 50 meters on each arm. The hydraulic treatment well is located at the cross-point of the two lines or arms.

As indicated in Figure 3.13 and Figure 3.14, src#1 is simulated right inside the treatment well at (x=0 m, y=0 m, z=500 m), src#2 at (x=300 m, y=100 m, z=600 m), and src#3 at (x=-600 m, y=700 m, z=600 m). Figure 3.15 shows the seismograms received from src#1, Figure 3.16 from src#2, and Figure 3.17 from src#3, with the assumption of homogenous and isotropic velocity model with noise levels of SNR=1.5 or SNR=3.

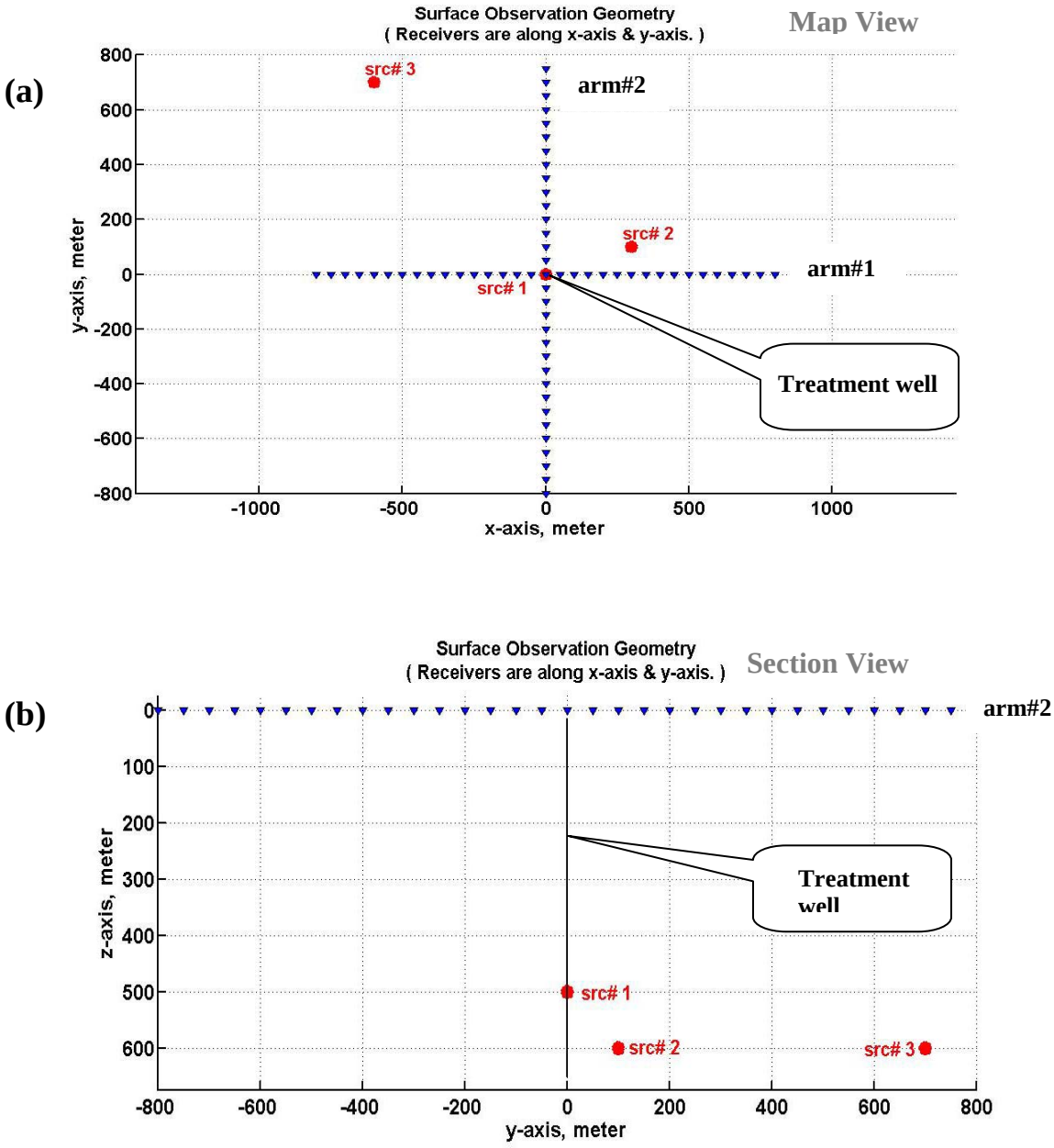

Figure 3.14: Section views of Figure 3.13 (a) the map plane and (b) the y-z plane.

(a)

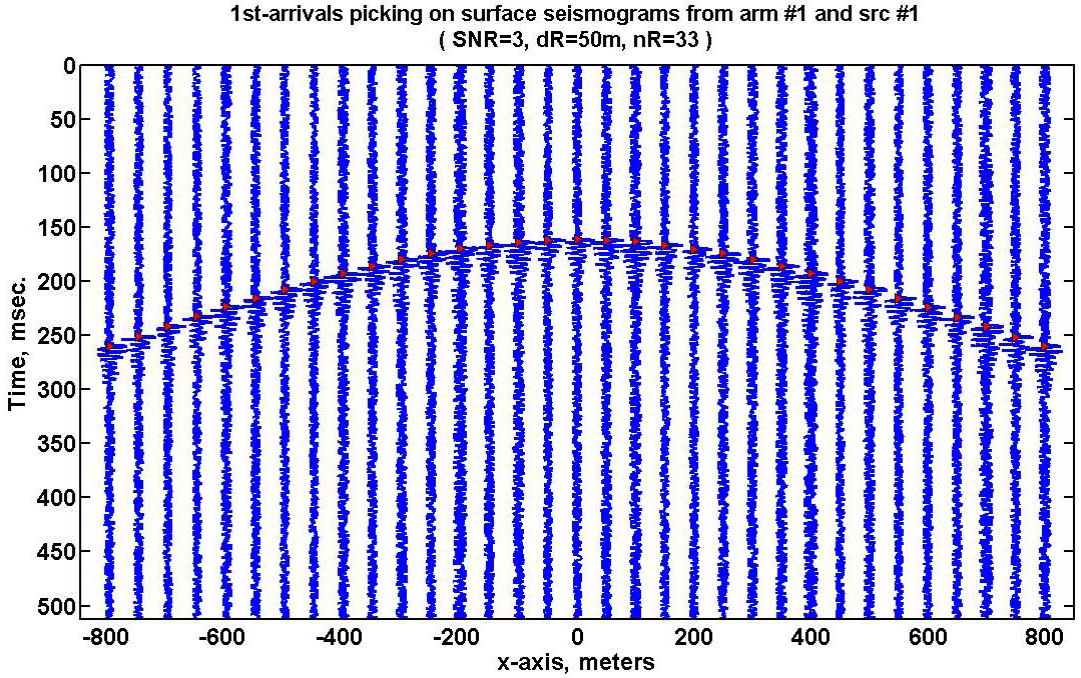

(b)

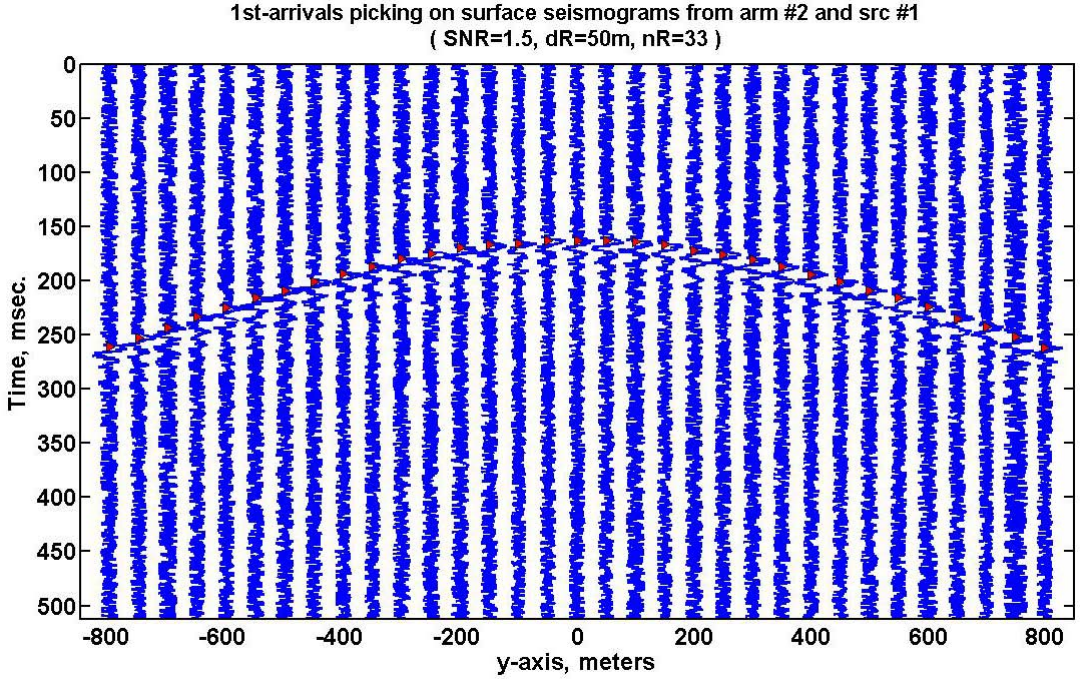

Figure 3.15: Data received at arm#1 (SNR=1.5) and arm #2 (SNR=3) from src #1 as indicated in Figure 3.13 or Figure 3.14.

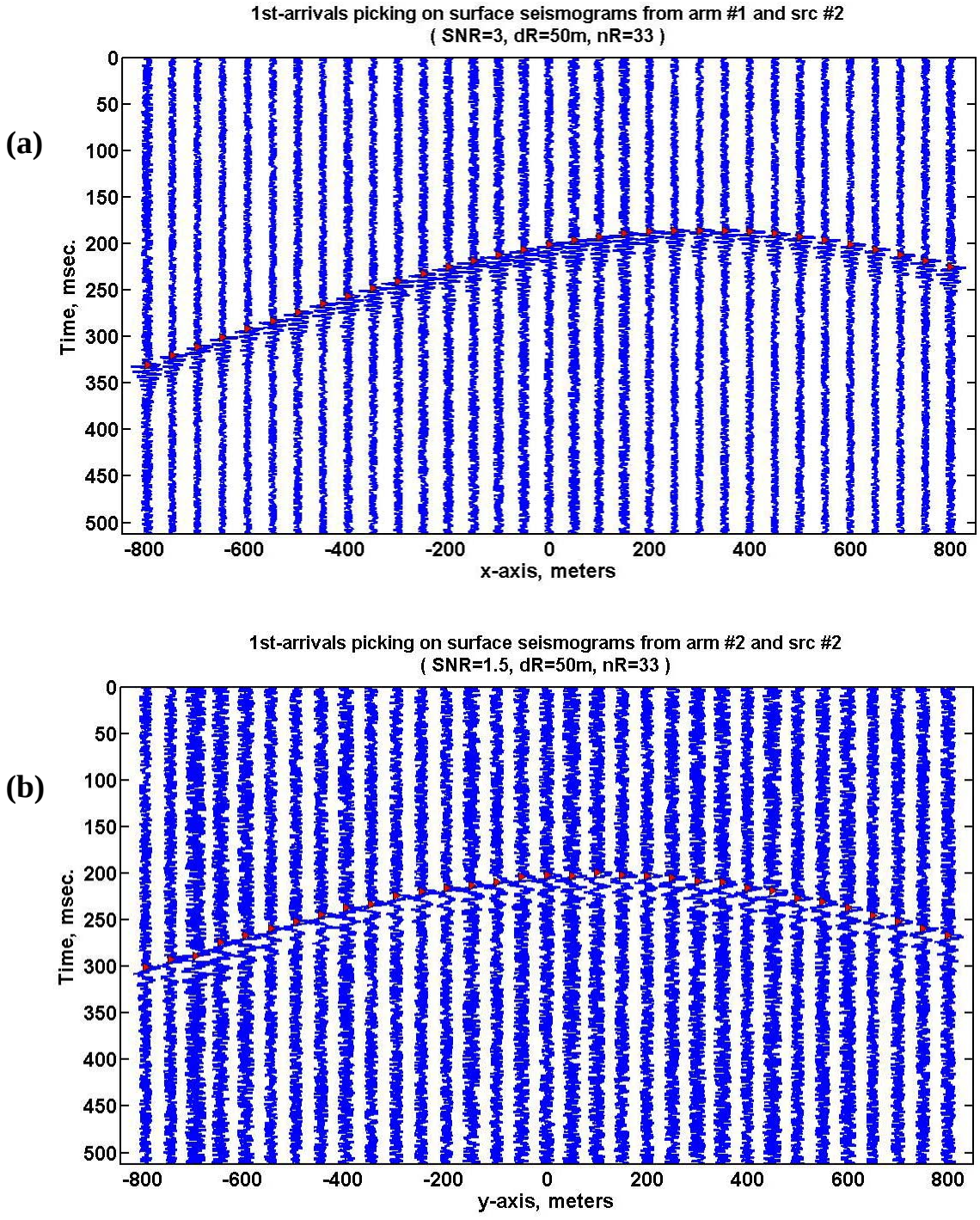

Figure 3.16: Data received at arm#1 (SNR=1.5) and arm #2 (SNR=3) from src #2 as indicated in Figure 3.13 and Figure 3.14.

(a)

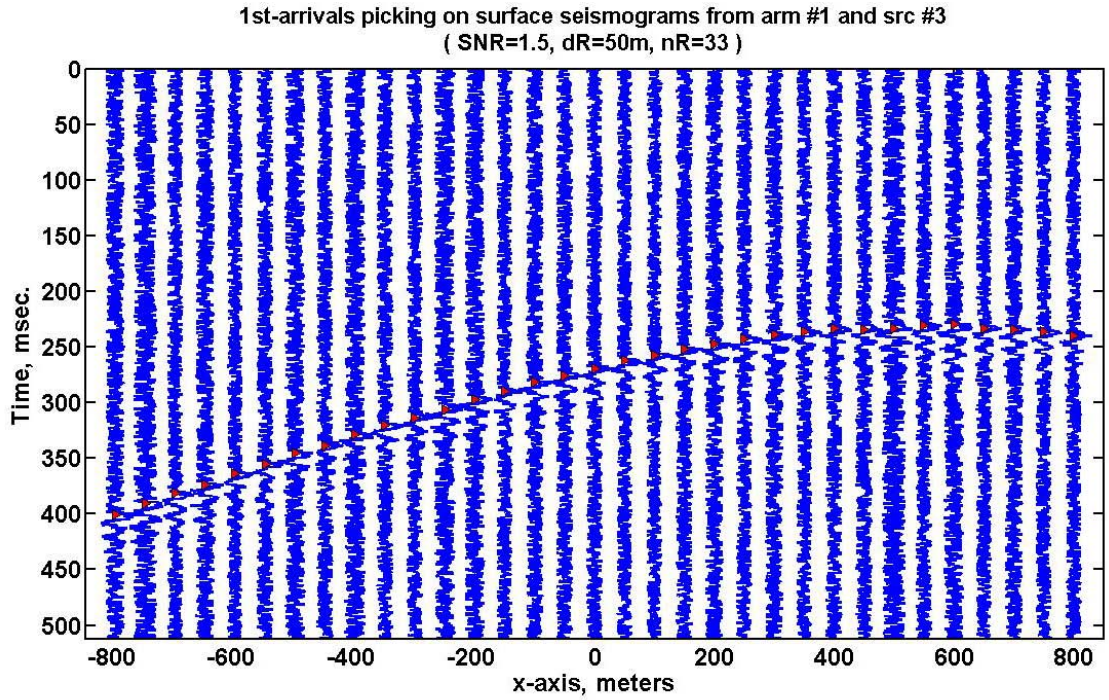

(b)

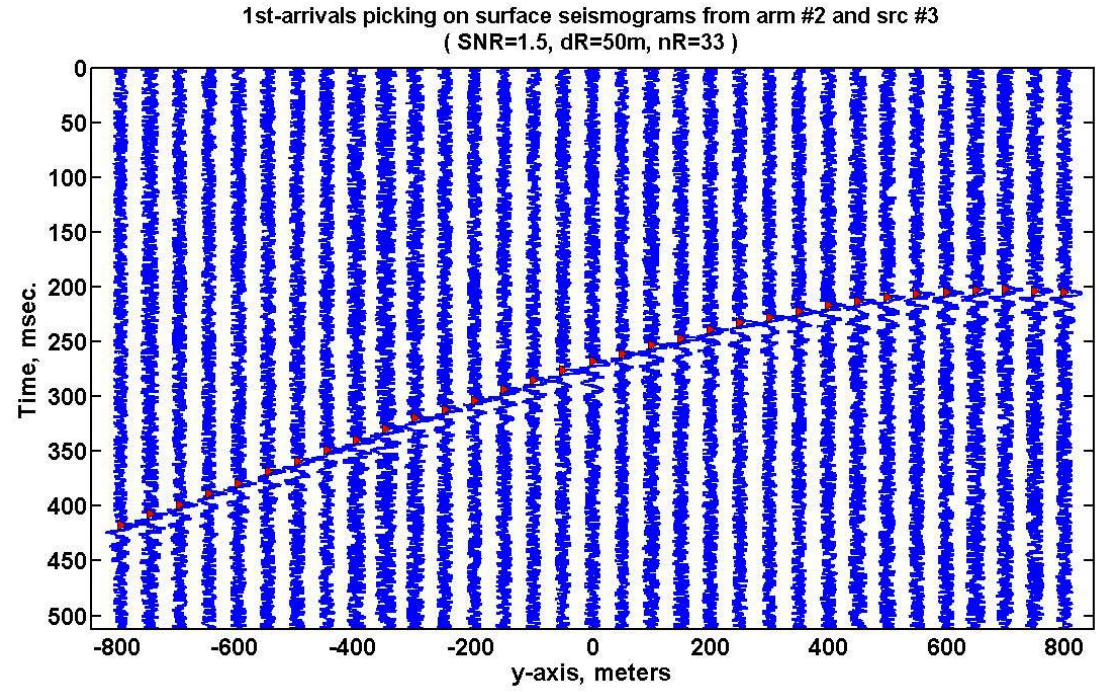

Figure 3.17: Data received at arm#1 (SNR=3) and arm #2 (SNR=3) from src #3 as indicated in Figure 3.13 and Figure 3.14.

Notice that unlike the data in the previous cases from well monitoring simulation, the noise imposed on the surface simulation is uniformly distributed (-.5 to 0.5). Also notice that as only the vertical component is recorded, and therefore polarization based downhole techniques are not applicable. As a contrast to the theme of methods in this thesis, we might take a look at the working approach of a conventional method for locating a microseismic hypocenter from surface data. Figure 3.18 shows the inversion results for data from src#1 as shown in Figure 3.12, Figure 3.19 shows for data from src#2 and Figure 3.20 for data from src#3.

It can be recognized in Figure 3.18 that the estimated location (x=29.9777 m, y=1.8594 m, z=511.6107 m) is well matched with the true location of src#1 (0, 0, 500), with the misfit ting error of 0.58791ms.

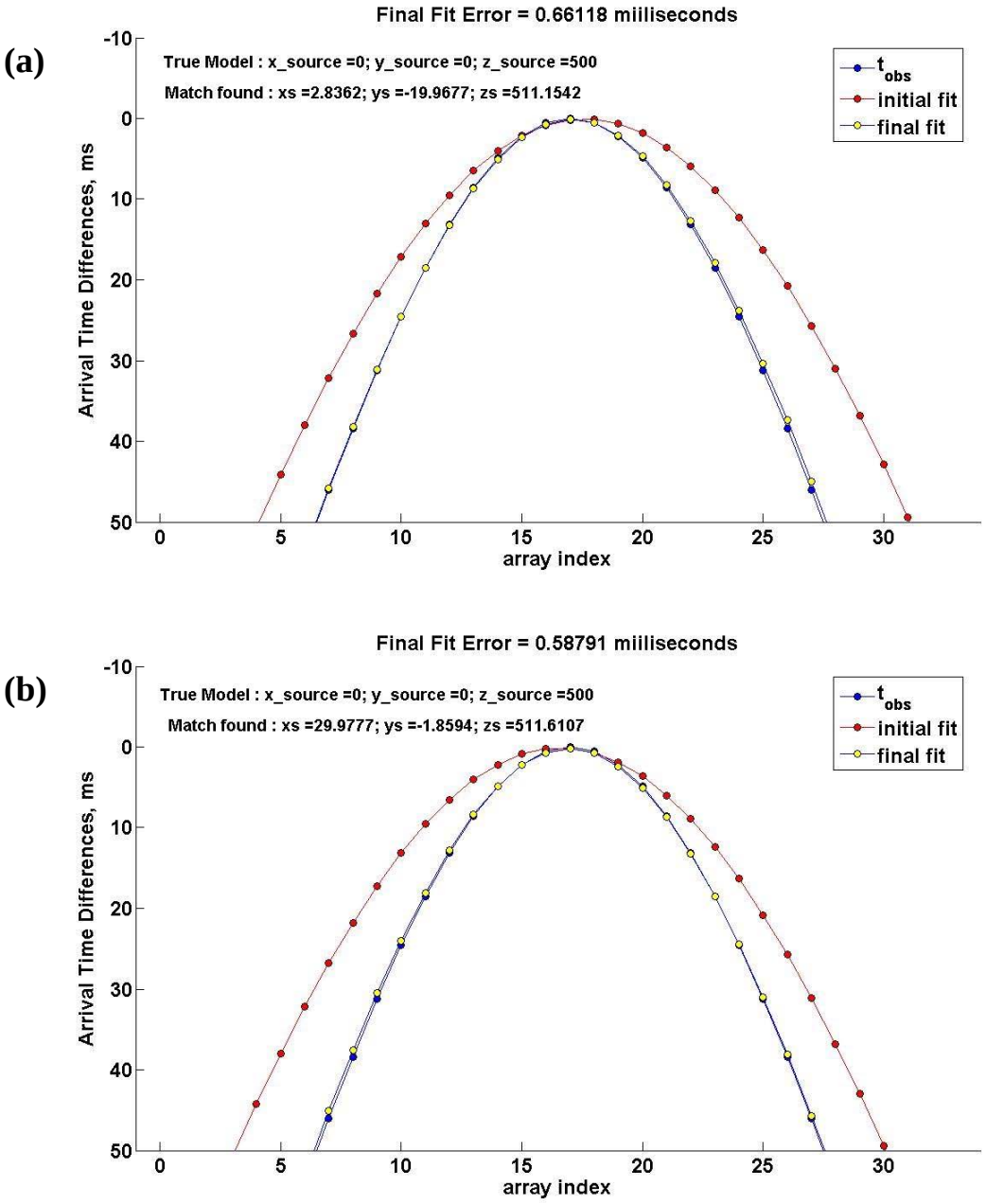

Figure 3.18: Inversion results from data received at arm1 (top) and arm2 (bottom) from src #1, as data shown in Figure 3.13 and Figure 3.14.

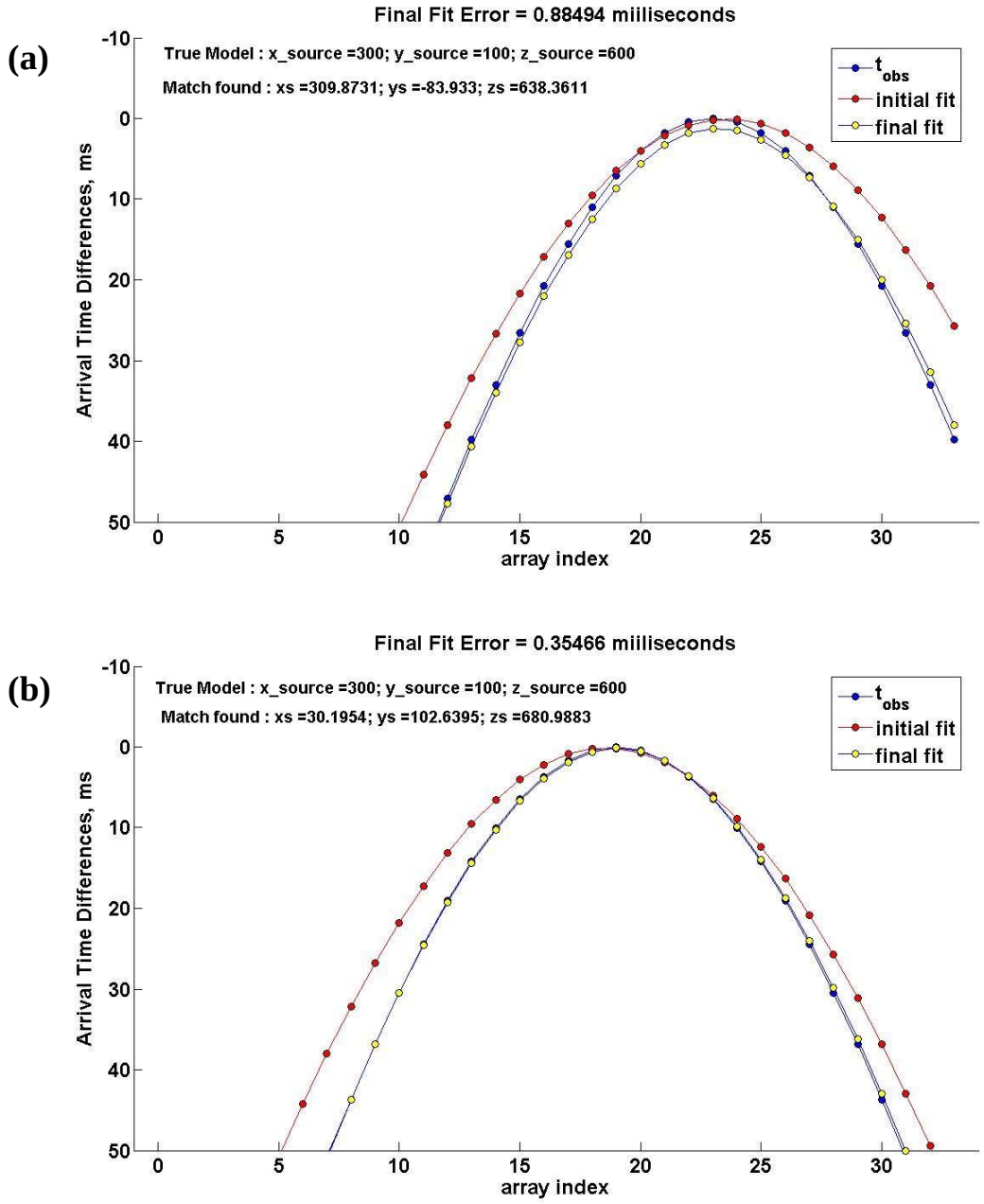

Figure 3.21: Inversion results for data at (a) arm 1 and (b) arm2 from src #2, as data shown in Figure 3.13 and Figure 3.14.

The estimated location from src#2, as shown in Figure 3.18, is not that optimal from data on both arms, due to the much bigger mismatch at y-axis from arm#1 and that at x-axis from arm#2.

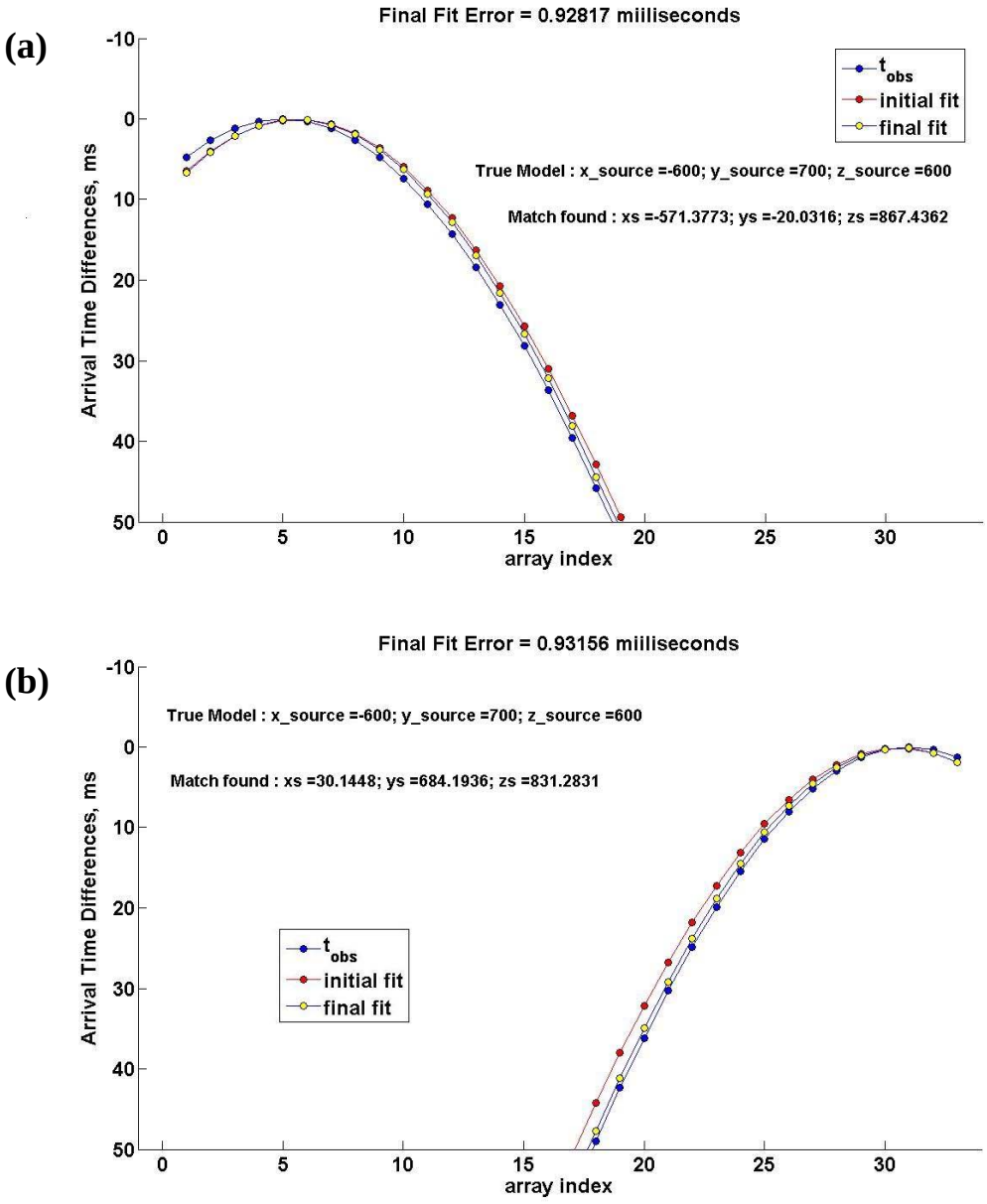

Figure 3.20: Inversion results for data at (a) arm 1 and (b) arm 2 from src #3, as data shown in Figure 3.13 and Figure 3.14.

From src#3, there still exist bigger mismatches at y-axis from arm#1 and x-axis from arm#2. However, there are many inversion algorithms existing and fitting for various particular situations. The appropriate choice can largely improve the location uncertainty of the estimated hypocenter. The method introduced in the rest of this thesis is quite different from conventional methods such as the inversion approach above.

3.6 Chapter summary

The modified energy ratio (MER) method was introduced and favoured to the standard STA/LTA formulation and other ER versions for automatic arrival time picking on microseismograms due to the higher noise tolerance (below SNR=3.5). Unlike the STA/LTA analysis, MER is not appropriate to use as an indication of signal to noise ratio.

The length of the energy-collection window is a critical attribute for the success of applying the MER analysis. It is suggested that testing might have to be done for the adjustment of the window length to a particular application, especially in the solution of picking multi-arrivals in multi-phases.

Chapter Four: Noise attenuation

Random noise limits the product quality of many seismic processing methods and procedures. Micro earthquakes produced by hydraulic fracturing of rock generally have low magnitudes of -2.0 or less on the Richter scale and produce microseismograms with low signal-to-noise ratios (SNR). Therefore, noise suppression on raw data prior to any other processing procedure, especially data with low SNR, is highly desirable.

In this chapter, noise attenuation with bandpass filtering, windowing by either minimum variances or modified energy ratios, stacking, matched filtering, and noise signal separation are introduced. An optimal approach was found to improve the MER method effectively, allowing reliable event picking in microseismograms with a SNR as low as1.5 as opposed to 3.5 using MER alone.

4.1 Bandpass filtering (*bp*-filter)

The frequency bandwidth of a synthetically induced microseismic source is typically assumed to be between 80 Hz or 200 Hz. Therefore frequency filtering is considered first to remove noise outside the target bandwidth. I will use one signal event at time 0.5 second that is inserted into Gaussian random noise giving a SNR of 3. This trace is bandpass filtered with a 20-40-120-140 Hz Ormsby filter centered at the dominant signal frequency of 80Hz.

Figure 4.1 illustrates the bandpass filtering effects on a single trace imposed by Gaussian noise. It can be observed that bandpass filtering has increased the SNR of the seismogram. Figure 4.1a show the noise trace on the left and its amplitude spectrum on the right. Figure4.1b contains similar images of the filtered trace and its spectrum.

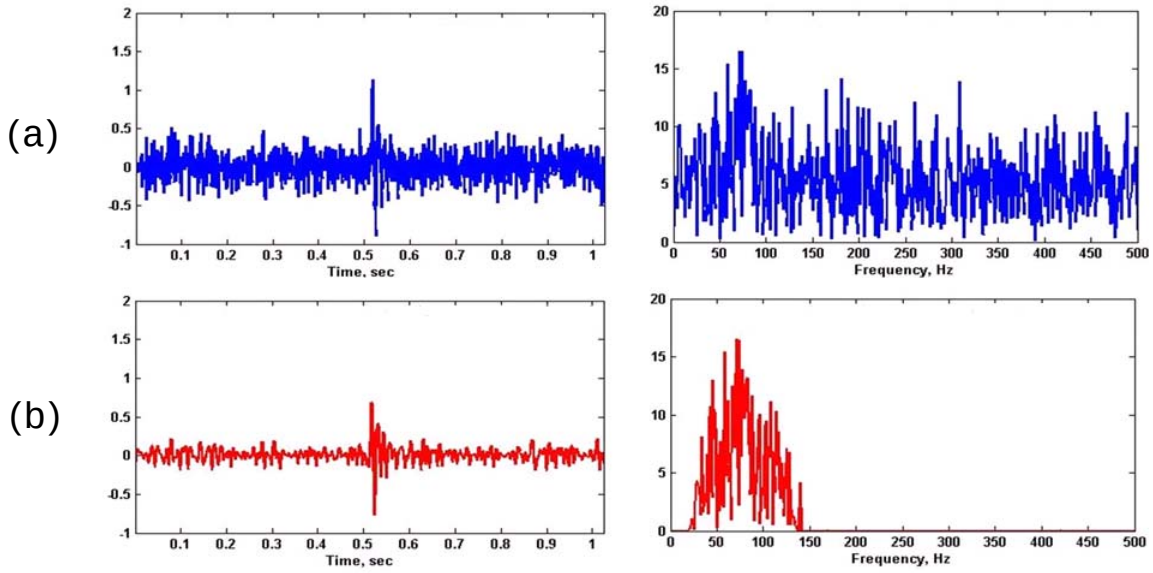

Figure 4.1: Bandpass filtering to reduce random noise. The blue plots in (a) show the trace spectrum and trace for a raw seismogram at a SNR=3. The red plots in (b) are the results after applying the Ormsby filter.

Bandpass filtering is always recommended once the signal frequency bandwidth is known.

4.2 Trace windowing, shifting, and initial stacking

Trace stacking or averaging is another common way to reduce random noise and to mitigate its adverse effect, as waveforms on a group of adjacent seismograms are usually similar and exhibit coherence. Their stacked amplitude is proportional to the trace number being stacked, say *n*. Random noise after stacking is proportional to the square root of the trace number,$\sqrt{n}$, hence the stacked SNR turns out to be $\frac{n}{\sqrt{n}} = \sqrt{n}$ times the original SNR.

The challenge for an automatic stacking process is to align the waveform on the traces by applying time shifts. The time shifts are found by choosing a reference trace

and then cross correlating the remaining traces in the group. The delay in the peak of the cross-correlation identifies the required time shift. Two alternative methods to align the traces, the minimum variance technique and the modified energy ratio technique, will be used and introduced.

4.2.1 Shifting by minimum variances (MVA)

The minimum variance technique for finding optimal shifts of coherent traces to a reference trace has been demonstrated in well-logging data (Han *et al*., 2009) which is similar to a semblance technique described by Sheriff (2006).

Figure 4.2 illustrates the technique using three high-frequency seismograms with similar waveforms *Rx1*, *Rx2*, and *Rx3* with linearly increasing delays as illustrated in part (a). The original traces had a SNR of 3. The traces were normalized and a suitable window chosen to isolate the first arrivals. The length and position of the window were based on the envelopes and dominant frequencies of the raw noisy seismograms. Trace *Rx3* was left unshifted as the reference trace, and then traces Rx2 and *Rx1* were shifted systematically by times of Δt and $2\Delta t$. The three traces were then added to form the average or sum trace $m(t)$. The difference or error between the average trace and each input trace at each time produced an index. The sum of the squared errors over all the time indices is the variance $var(\Delta t)$. The following equations were used to calculate $m(t, \Delta t)$ and $var\ (\Delta t)$ for many values of Δt until a minimum for $var(\Delta t)$ is found:

$$m(t, \Delta t) = [Rx1(t + 2\Delta t) + Rx2(t + \Delta t) + Rx3(t)]/3, \tag{4.1}$$

$$var(\Delta t) = \sum_{t=0}^{t\max} \{\ [m(t, \Delta t) - Rx1(t + 2\Delta t)]^2 + [\ m(t, \Delta t) - Rx2(t + \Delta t)]^2 + [\ m(t, \Delta t) - Rx3(t)]^2\ \} \tag{4.2}.$$

The variance is least when the windowed waveforms are in phase as illustrated by the minimum value of the variance as plotted in Figure 4.2b. The optimal average trace *m(t)* corresponding to the minimum variance is less noisy than the input traces, and can be used as the reference trace and then repeating the process. This method for finding the optimal shift and then shifting and stacking them for the noise attenuated sum trace is called minimum variance stacking, or *mv*-stack (Han *et. al*., 2008).

However, this technique is limited by noise. Figure 4.3 shows two panels of 15 traces with SNRs of 3.5 and 2.5 on the left. On the right are the time shifted traces with the aligned waveforms. Noise levels lead to unstable time shifts that do not correctly all traces. The lowest SNR level appears to be 3.5 for which the technique is successful; while higher noise levels lead to unstable time shifts that do not correctly align all traces, as shown in Figure 4.3b. Many tests were conducted with varying SNRs, but only two are shown to illustrate the limited SNRs. SNRs above 3.5 are successful in aligning the waveforms while those at or below 2.5 were successful.

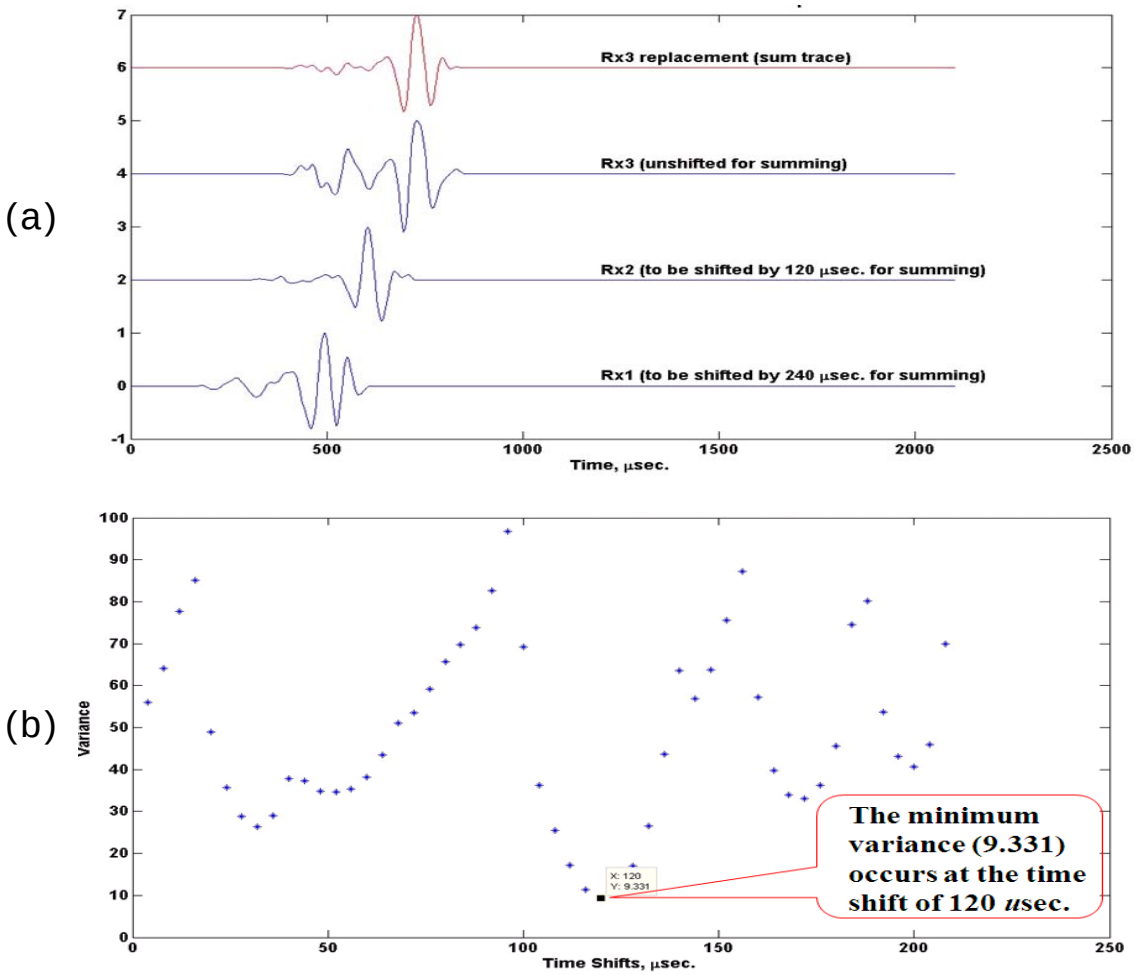

Figure 4.2: The minimum variance technique for trace shifting and stacking. Three traces (Rx1, Rx2, and Rx3) are shown in (a) the optimal shift $\Delta t = 120$ us corresponding to the minimum variance (9.331) is found through a series of calculation of (shift, variance) pairs in (b).

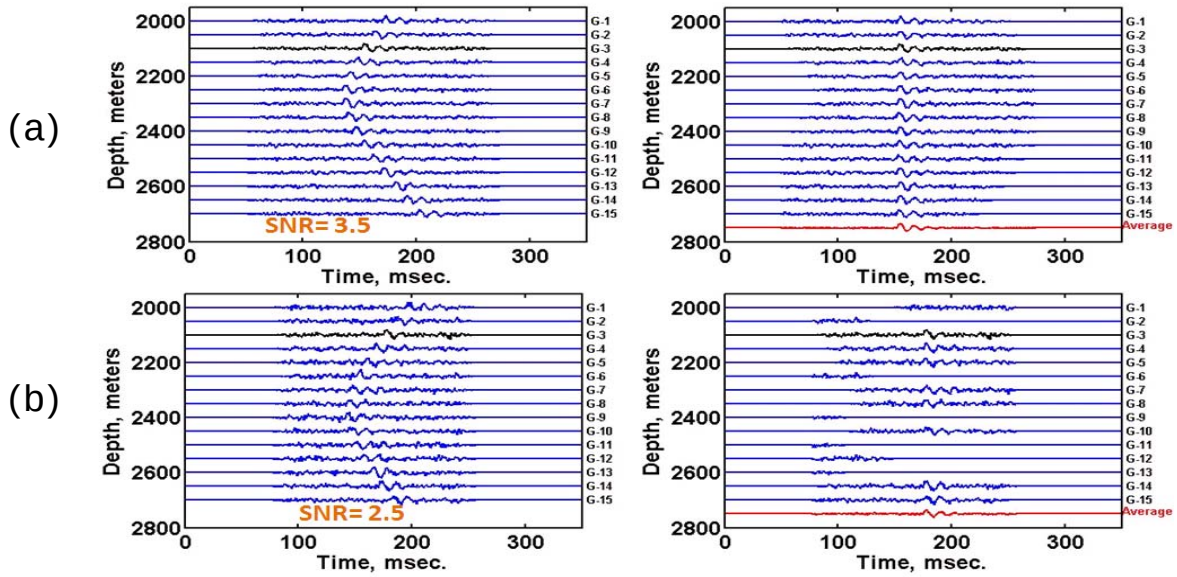

Figure 4.3: Noise limitation on the minimum variance technique with (a) containing traces with SNRs of 3.5 and (b) with SNRs of 2.5 he estimated alignments are shown on the right.

4.2.2 Shifting by modified energy ratios (MER)

The robustness of the MER method for event detection and arrival time-picking in the presence of random noise has been demonstrated previously and now presented in more details as an alternative to the minimum variance technique.

Define a window in the following way. The time picks were median-filtered to remove outliers. The minimum and maximum time values, t_{min} and t_{max} of the filtered data were then chosen. The dominant period of the seismic event is assumed to be T. Let t_1 be a value in the range $2T$ to $4T$. The leading edge of the window is defined from (t_{min} - t_1) and the trailing edge is defined from (t_{max} + t_1).

Many tests were conducted with the MER method at various SNRs. Figure 4.4 demonstrates that accurate time shifts and phase alignment based on the MER time picks

on seismograms with SNR as low as 2.5. Notice that the minimum variance technique is not able to appropriately shift all traces at such low noise level as shown in Figure 4.3. Figures 4.4 demonstrate that accurate time shifts and phase alignment based on the MER time picks on seismograms with SNR as low as 2.5. Notice that the minimum variance technique is not able to appropriately shift all traces at such low noise level as shown in the right of Figure 4.3 b.

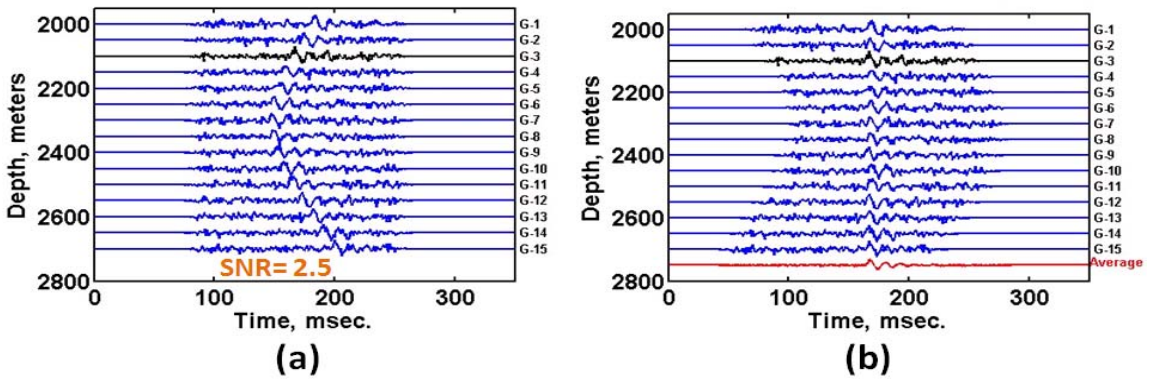

Figure 4.4: The MER technique for trace shifting and stacking. The MER technique can shift (a) seismograms with Gaussian noise of SNR=2.5 appropriately into (b) seismograms aligned with the average trace shown in red.

It is concluded that the windowing and shifting approach is favoured with the MER technique over the minimum variance technique for producing the initial stack trace or attenuating random noise.

4.3 Matched filtering and further stacking (*Mm*-stack)

Trace shifting and stacking based on the MER triggering technique is also limited by noise and it is difficult to align trace with SNR lower than 2.5. To further suppress random noise, matched filtering (Eisner *et al*. 2008), or cross-correlation, will be used to correct the inappropriately shifted traces. The event triggering effect of the MER technique at SNR=1.3 are shown in Figure 4.5, with red dots identifying the estimated

location of the waveform. The corresponding trace shifting of the seismograms results in Figure 4.6. The adjusted shifting by matched filtering technique results in Figure 4.6b.

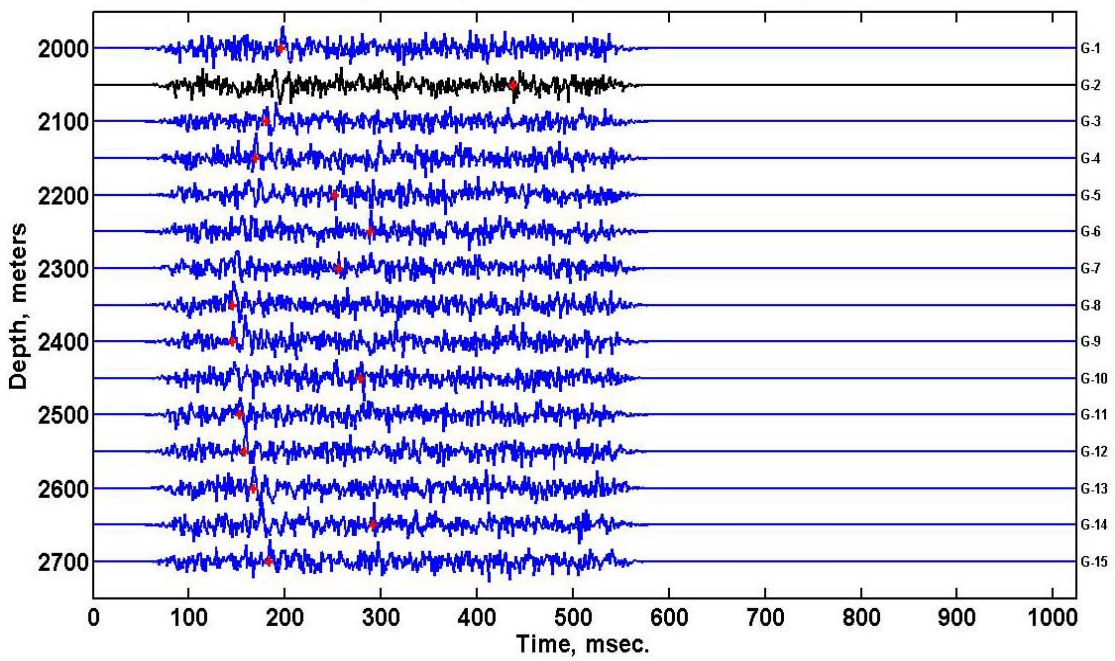

Figure 4.5: Inappropriate MER time picks on high noisy microseismograms (SNR≈1.3).

The initial MER time picks on high noisy seismograms of SNR=1.3 are not appropriate for trace G-2, G-5, G-6, G-7, G-10, and G-14 as observed in Figure 4.5. Then trace shifting was done by choosing a reference trace (shown in back) first and then shifting all other traces according to the initial MER time picks shown in Figure 4.5. As this preliminary trace shifting according to these inappropriately picked arrivals are not aligned correctly, as shown in Figure 4.6, hence the resulting sum trace (the red trace in the bottom of the figure) is not optimal.

(a)

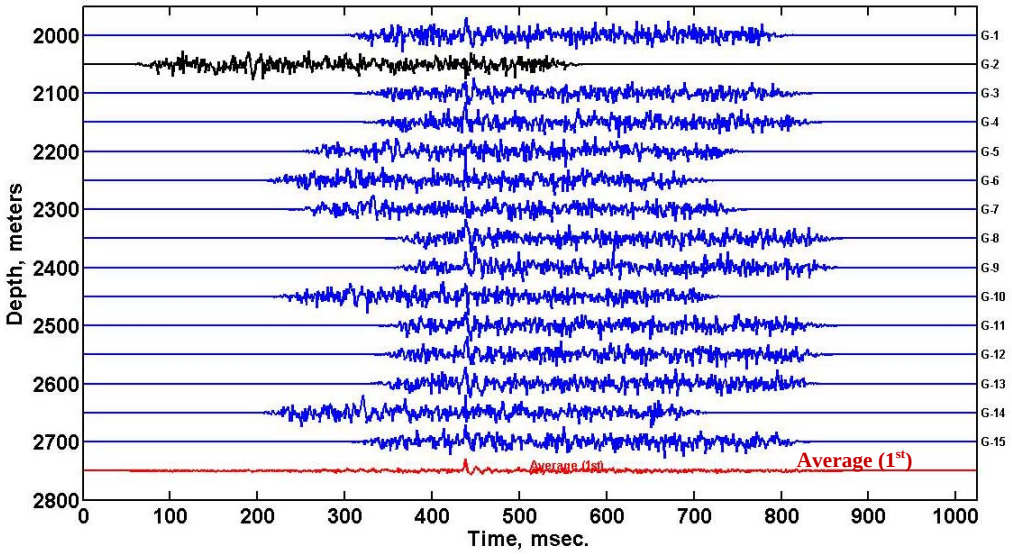

(b)

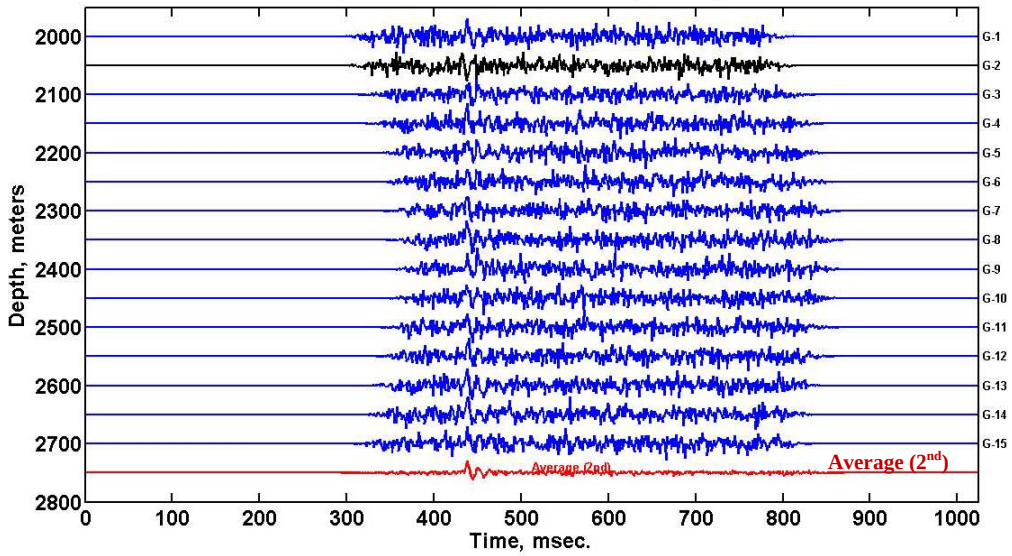

Figure 4.6: Inappropriate aligned traces based on MER picks. The temporal positions of true signals are indicated in red circles while miss-aligned or miss-shifted due to the miss-picked arrival times shown in Figure 4.5.

Matched filtering was used in the sense that the cross correlation of each pair of traces provides a numerical characterization of their similarity as a function of relative time shifts. The maximum value of the cross correlation defines the time shift at which two traces are most similar when aligned. This matched filtering process was also

applied for finding the shifting adjustment due to inappropriate arrival times inappropriately picked with the MER method in the following way:

$$xcor(\tau) = \sum_{t=0}^{tLen} g_i(t) * s(t+\tau), \tag{4.3}$$

where $xcor(\tau)$ represents the crosscorrelation evaluation at relative time shift τ between the i^{th} trace $g_i(t)$ and the initial sum traces$(t+\tau)$; $tLen$ represent the trace length.

As observed in Figure 4.5 and 4.6, there are 15 geophones in the research producing 15 traces or seismograms for testing experiments. All inappropriately shifted traces in Figure 4.6 (i.e., trace G-2, G-5, G-6, G-7, G-10, and G-14) are adjusted back to their right positions after the matched filtering process, as shown in Figure 4.6.

As all shifted traces turn out to have embedded seismic signals aligned, the sum trace achieves the optimal effect of noise attenuation by $\sqrt{15}$ times the SNR on raw data, hence has the SNR upgraded to 5.0 from 1.3. This stacked trace is shown as the bottom traces in Figure 4.6.

To this end, the stacking process has adopted the MER technique as well as the matched filtering technique, and will be referred as the *Mm*-stack process in the following text.

4.4 Noise and signal separation (NSS)

This procedure further suppresses random noise by separating each seismogram into a relatively noise-free component. That can be evaluated using hodogram analysis.

The synthetic seismogram of each trace $g_i(t)$ is generated by convolving the source signal with the reflectivity of the earth model and then adding noise $n_i(t)$, giving

$$g_i(t) = w(t) * r_i(t) + n_i(t) \tag{4.4}$$

where $g_i(t)$ is the i^{th} trace of seismograms, $w(t)$ is a source wavelet, * denotes the convolution operator, $r_i(t)$ is the reflectivity, and $n_i(t)$ is random noise. I now assume we have a group of aligned noisy traces as illustrated in Figure 4.7a, where the relative time shifts t_i are known. The alignment allows equation (4.3) to be simplified from

$$g_i(t) = a_i * w(t) + n_i(t) \tag{4.5}$$

where the reflectivity $r_i(t)$ is replaced by a scalar factor a_i.

The relative time delay of the arriving wavelet is first estimated from MER method as introduced in the previous chapter. These events are then aligned with the time shifts and stacked to obtain an estimate of the wavelet. The wavelet is then used to refine the estimated time shift and to estimate the amplitude of the wavelet on each trace. The stacked trace $s(t)$ is formed by summing the traces and dividing the number of traces (n).

$$\begin{aligned} s(t) &= \frac{1}{n}\sum_{i=1}^{n} a_i w_{ref}(t) + n_i(t) \\ &= \overline{a} * w_{ref}(t) + \frac{n(t)}{\sqrt{n}}. \end{aligned} \tag{4.6}$$

This stacked trace with reduced noise is shown at the bottom of Figure 4.7a. Taking the dot product of equation 4.4 with the stack trace *s(t)*, i.e., the cross-relation, we get

$$g_i(t) \cdot s(t) = a_i * w(t) \cdot s(t) + n_i(t) \cdot s(t). \tag{4.7}$$

The cross-relation of $n_i(t)$ with $s(t)$ tends to zero. With this assumption, a_i can be estimated from

$$a_i = [g_i(t) \cdot s(t)]/[w(t) \cdot s(t)]\ . \tag{4.8}$$

Knowing the amplitude of the individual wavelet is required to locate the direction of a microseismic event. As we will be using the hodogram method that also requires a wavelet, we create synthetic traces using the amplitude a_i and the estimated wavelet *s(t)* as illustrated in Figure 4.7(d).

With real data we do not know the reference signal $w(t)$. However, we can approximate $w(t)$ with *s*(*t*), which simplifies equation 4.3 as

$$a_i \sim [g_i(t) \cdot s(t)]/[s(t) \cdot s(t)] , \tag{4.9}$$

where a_i represents an estimated amplitude-scaling coefficient. The estimate of *w*(t) can then be used to refine the time picks on the original data to produce a better estimate of the time aligned traces.

The amplitude-scaling coefficient for each trace is then used to scale the wavelet to obtain a synthetic noise-free version of that trace

$$g_i^0(t) = a_i * s(t). \tag{4.10}$$

The difference between the original trace $g_i(t)$ and the synthetic trace $g_i^0(t)$ should be residual noise. In this way, each noisy trace is separated into synthetic component and noise. The signal component, $a_i * s(t)$, is noise-free to the extent that the dot product $n_i(t) \cdot s(t)$ is zero or very small.

Figure 4.7 displays results from applying the NSS process to the output of *Mm*-stack procedure. This figure shows the aligned microseismograms of (c) SNR ≈ 1.5 and the stack trace of SNR ≈ 5.8 (the red trace in the bottom of (c)). There appears to be little or no coherence between the stack trace and the noise components of (e), indicating that the dot product $n_i(t) \cdot s(t)$ is much less than the product $a_i * s(t)$. This implies that

NSS tends to preserve the true relative signal amplitudes of traces in each recording set of microseismograms.

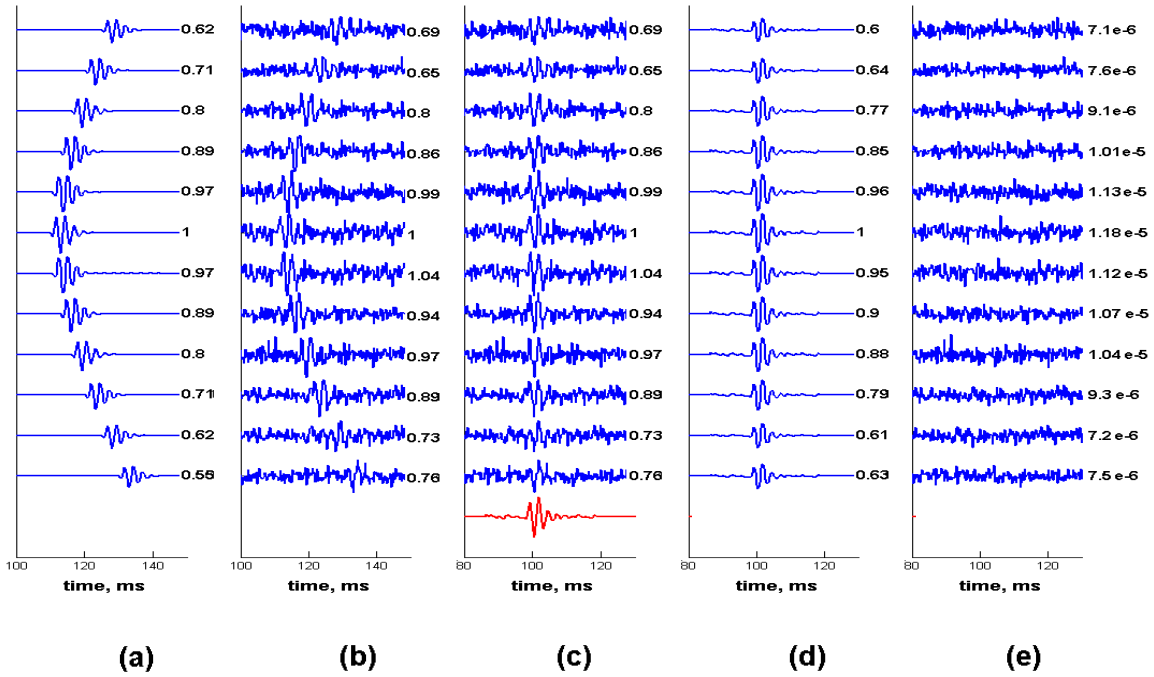

Figure 4.7: Noise attenuation and efficiency test. (a) seismograms of true waveforms; (b) noisy seismograms (c) noisy seismograms alignment after *bp*-filter and *Mm*-stack; the bottom red trace is the normalized stack trace; (d) signal component of noisy traces after NSS; (e) separated Gaussian noise components after NSS.

The NSS process could be iteratively applied to extract the signals until a certain threshold or criteria are reached. Further investigation and extensive experiments on this iteration effect would be interesting.

This noise-signal separation (NSS) method of estimating the noise-free components from a group of noisy seismograms attempts to preserve the relative signal amplitudes. The amplitudes are used to identify the direction back to the source. A number of methods to identify this direction are available, but I will use hodogram analysis for locating the microseismic hypocenters.

4.5 The optimal noise attenuation approach

It can be concluded that the optimal noise attenuation effect will be produced with the based on bandpass filtering (*bp*-filter), MER windowing and matched filtering (*Mm*-stack), then noise and signal separation (NSS). This joint procedure was implemented as the optimal noise attenuation approach to pre-process raw data prior to any method being proposed in this thesis. The efficacy of this approach can be demonstrated through the joint effect with the MER method and the noise attenuation effect examination on synthetic 3C microseismograms.

4.5.1 The joint and improving effect on MER analysis

Seismic event detection and arrival time-picking are the very first and critical step for microseismic monitoring and estimating the hypocenter location. The MER method was proposed and introduced in Chapter 3 as a sensitive energy transient trigger for accurately picking arrival times from raw microseismograms with SNR = 3.5 or higher.

Combining the optimal noise attenuation scheme with the MER time-picking procedure can efficiently lower the SNR on raw data to a 1.5 when 15 similar traces are available, as shown in Figure 4.8. In this case MER picking is limited to a SNR=3.5. However, the pre-processing of the optimal noise attenuation schema indeed upgrades the SNR of microseismograms from 1.5 to 5.8, and hence the post-processing of MER arrival time-picking can produce arrival times appropriately for all 15 traces as shown in Figure 4.8(b).

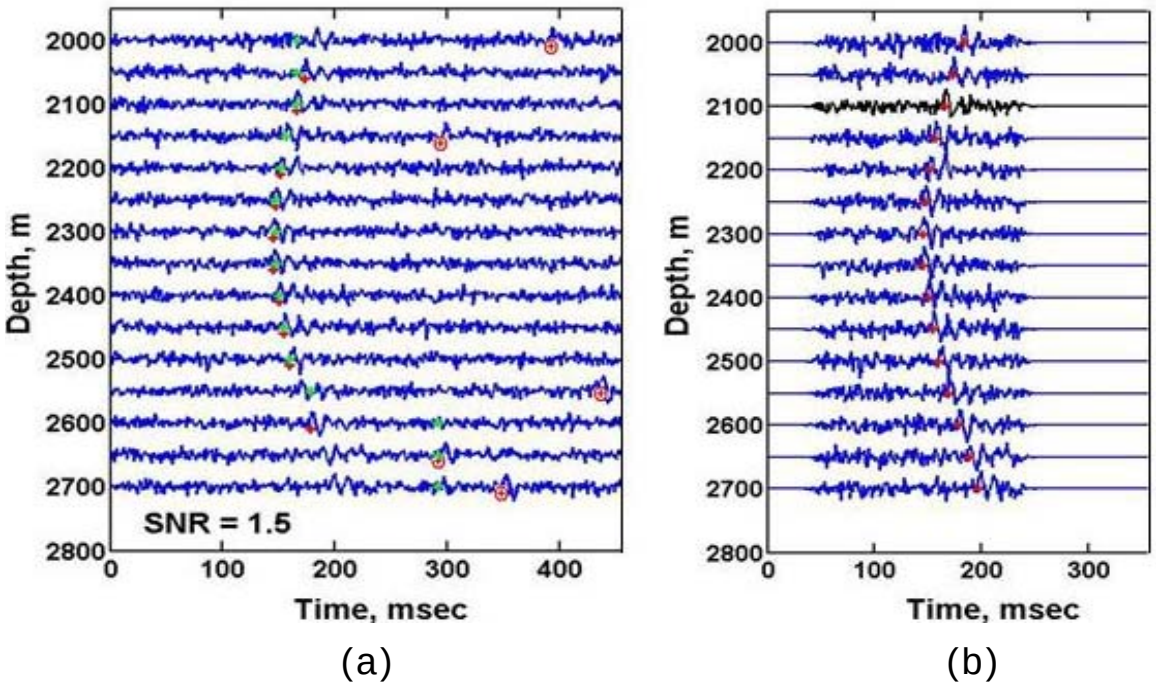

Figure 4.8: MER time-picking on noisy data (SNR=1.5) with noise attenuation pre-processing. Left: the inappropriately picked arrivals (circled in red) with the MER method alone. Right: with the optimal noise attenuation pre-processing, all initial red crosses (produced by MER again) becoming around the first breaks of arrivals in all traces.

4.5.2 The optimal noise attenuation effects on 3C seismograms

The joint effects of the optimal noise attenuation methods will be illustrated the 3-component (3C) data previously shown in Figure 3.10, and now displayed in Figure 4.9. The NSS method was applied separately to each of the three components, e.g. to all vertical components. Noisy traces from the three wells are displayed on the left hand side of (a), (b), and (c). The corresponding NSS processed data is shown on the right. Notice the preservation of amplitude and phase of the waveform is the right side of Figure 4.9.

The time delays t_i and amplitudes a_i could be sufficient to estimate a source location, however, the wavelet allows the use of the hodogram method to be used in locating a seismic event, as presented in the next chapter.

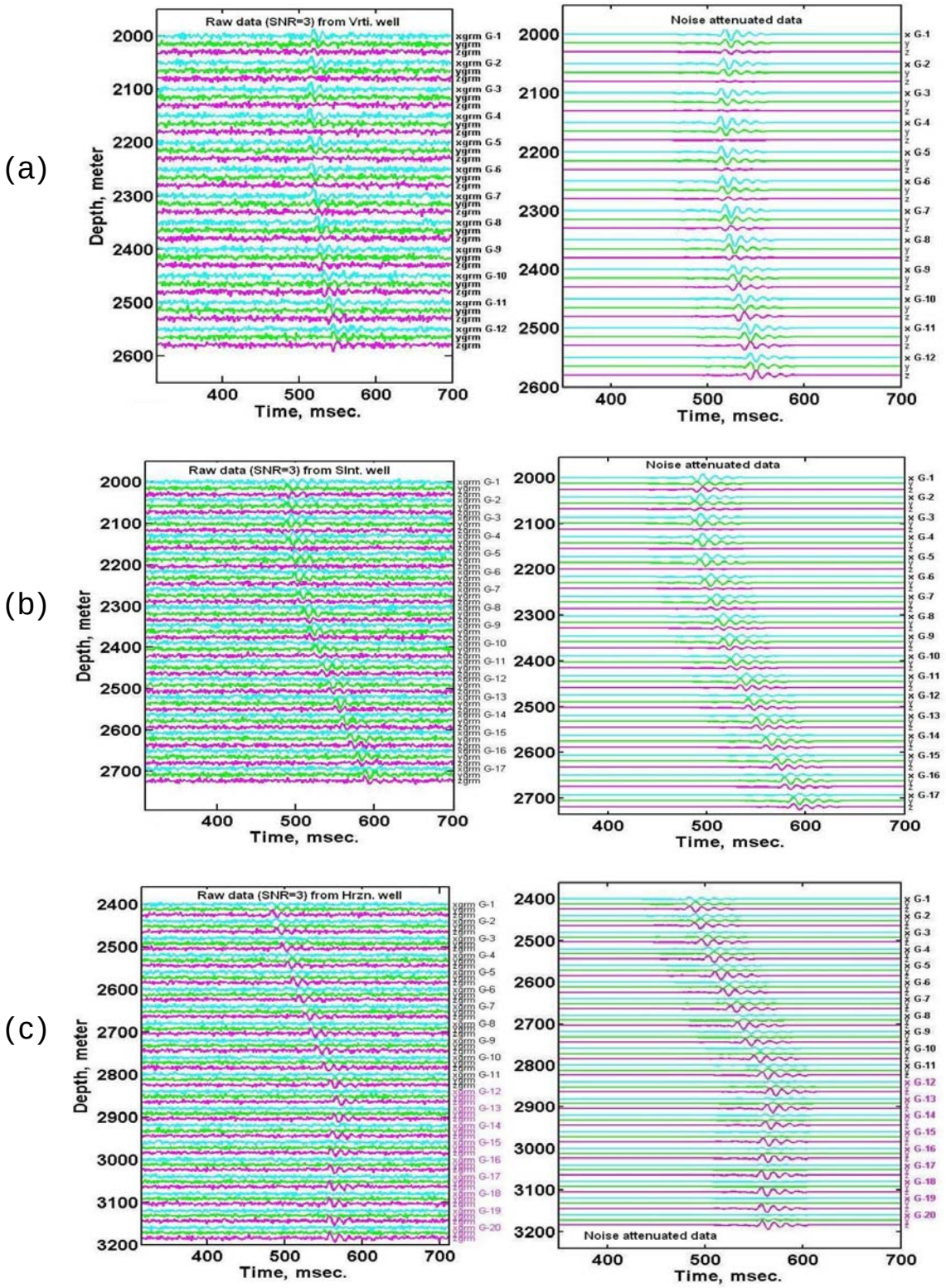

Figure 4.9: Noise attenuation effects (the right column) on noisy 3C data (the left column) obtained from (a) a vertical well, (b) a slant well, and (c) a horizontal well, respectively at a SNR=3.

4.6 Chapter summary

The optimal noise attenuation approach, including *bp*-filter, *Mm*-stack, and NSS, can effectively attenuate Gaussian noise and improve the data quality. Jointed with this schema, the MER time picking method can improve its noise tolerance from SNR=3.5 to SNR=1.5. Noise attenuation effects on the hodogram linearity and the location uncertainty will be demonstrated in Chapter 5 and Chapter 6 respectively. Hodogram analysis works when accurate relative arrival times are not known.

Chapter Five: Hodogram polarization analysis

Polarization analysis is commonly used in a three-component recording scenario to obtain the wave propagation direction incident at each recording site.

There are two common methods for polarization analysis: hodogram analysis and eigenvector analysis. Estimating the propagating azimuth and/or polarization from the hodogram orientation is generally much faster than using the eigenvector decomposition of covariance matrix from displacements of microseismograms (Flinn, 1965; Vidale, 1986). However, polarization analysis based on hodograms has a lower (worse) noise tolerance than an approach based on eigenvector/eigenvalues. Hodogram polarization analysis introduced in this chapter can however achieve the higher noise tolerance, by employing a weighted least squares regression technique along with the choice of noise attenuation schemas.

Two (planar and spatial) approaches, for two dimensional (2D) and three dimensional (3D) spaces respectively, are implemented and tested within the MATLAB environment.

5.1 The 2D approach of hodogram polarization analysis

A hodogram, as defined in Encyclopedic Dictionary of Exploration Geophysics (R. R. Sheriff, 1991), can be the figure described by the terminus of a moving vector, or a plot of the motion of a point as a function of a time, that is, a display of particle path, or a time-distance curve. In microseismic hodogram analysis, it usually means a parametric plot of recording components at a 3C geophone, varying with the common parameter of recording time, such as the *x* and *y* components composing of the 2D map hodogram, or *r*

and *z* components of the 2D radial hodogram. The orientation of such a planar plot will indicate the azimuth on the map, or dip on the radial section for the propagating wave front (or ray path) incident at a geophone. Reducing this 3D problem into two 2D planes is applicable if the receivers are confined to a vertical array and is referred to as the 2D approach.

At a given geophone, if the *x*-*y*-*z* component recording at the time index t_i is represented by the triplet $\left[g_x(t_i),\ g_y(t_i),\ g_z(t_i)\right]$, then the hodogram on the map view (or the map hodogram) is the parametric plot of $g_x(t_i)$ versus $g_y(t_i)$ with the time index as the parameter. Similarly, if the radial component is formed as

$$g_r(t_i) = sgn\left(g_x(t_i)\right) \cdot sgn\left(g_y(t_i)\right) \sqrt[2]{g_x(t_i)^2 + g_y(t_i)^2}\,, \tag{5.1}$$

then the hodogram on the radial section (or the radial hodogram) is the parametric plot of $g_r(t_i)$ and $g_z(t_i)$ at that given geophone.

A low-noise example of synthetic data, with a SNR=50, is shown on Figure 5.1, with (a) showing the three x-y-z components, (b) the hodogram projection on the map view, and (c) the hodogram projection on the radial section. The hodograms appear to be nearly straight lines, along which there are only very small disturbance due to Gaussian noise. Therefore the hodogram azimuth orientation on the map view, or the dip on the radial section is nearly straight lines, which clearly indicate the arrival direction of the incident wavefront.

Note that the information obtained from the hodogram analysis is independent of an accurate arrival time of the wavelet.

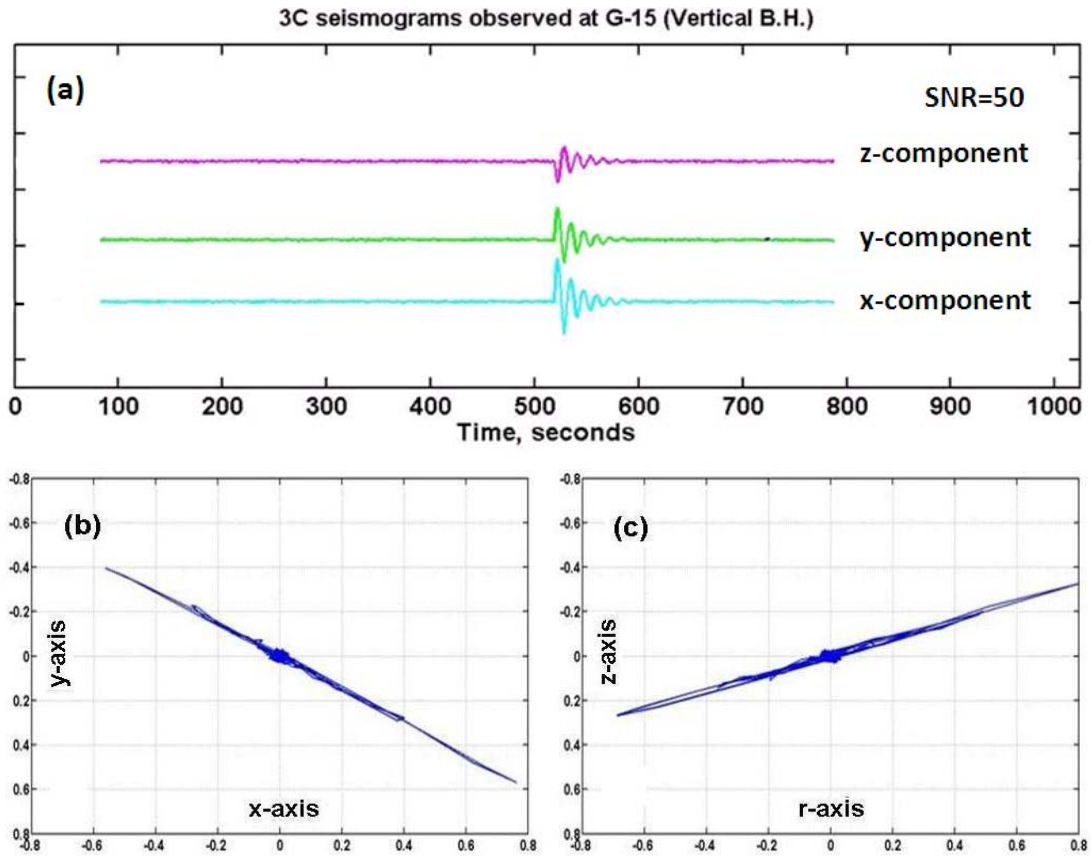

Figure 5.1: Hodograms from low-noise data. (a) Components of seismic recording at a single 3C geophone, with a very low Gaussian noise (SNR=50); (b) hodogram on the map view; (c) hodogram on the radial section.

However, such a high quality data (SNR=50) is hard to obtain from field acquisition in the real world. As the noise level increases, the dominant linearity of hodogram decays, as illustrated in Figure 5.2 for cases of (a) noise-free, (b) SNR=10, and (c) SNR=3 respectively.

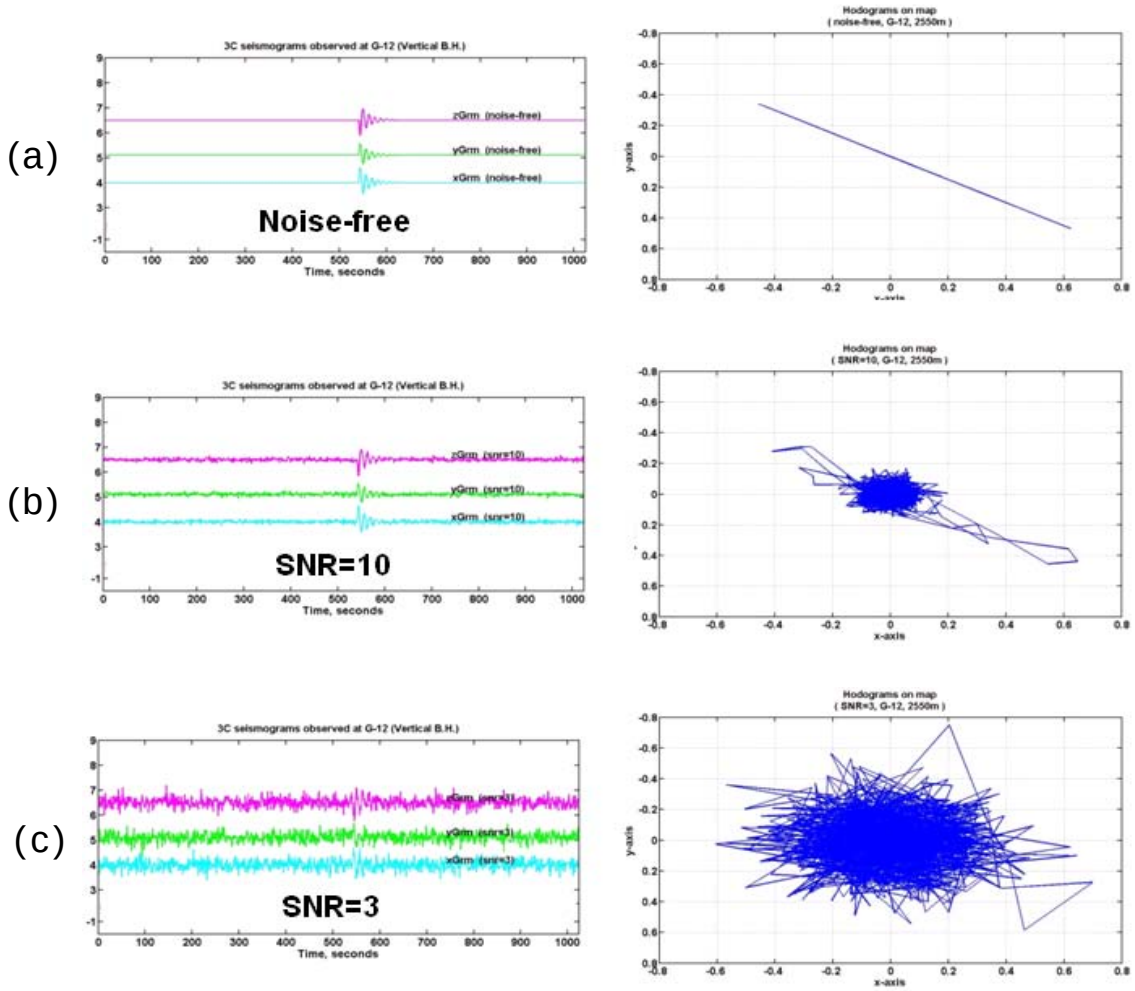

Figure 5.2: Gaussian noise effects on hodograms. Data components (left panel) and respective map hodograms (right panel) from a single 3C with three levels of Gaussian noise superimposed: (a) noise-free, (b) SNR=10, and (c) SNR=3.

Notice that a hodogram would be an exactly-straight line if the data is noise-free, as in the simulated result of Figure 5.2a, which is otherwise impossible to see from never-noise-free field data. The dominant linearity of the hodogram is much less obvious in Figure 5.2b and virtually impossible with higher-noise data, as the example in Figure 5.2c.

Hodogram polarization analysis is able to identify the dominant linearity of hodogram in both a 2D space and a 3D space. Weighted least squares regression

techniques have been theoretically verified as the maximum likelihood approximation to data with the presence of random noise (Aster *et. al.*, 2005), and has been used in this thesis to estimate the dominant linearity of a Gaussian-noisy hodogram with the following planar approach.

Assume that the dominant linearities of two planar hodograms from a 3C geophone are given by the linear equation $y = k_{map}x + b_{map}$ on a map where x and y are two parameters from two components $g_x(t_i)$ and $g_y(t_i)$ and the linear equation $z = k_{rad}r + b_{rad}$ on the radial section where r and z are from $g_r(t_i)$ and $g_z(t_i)$. Also assume there are n recording samples from each component at that given geophone, and then we can have the following linear systems:

$$\begin{cases} b_{map} + k_{map}\, g_x(t_1) = g_y(t_1) \\ b_{map} + k_{map}\, g_x(t_2) = g_y(t_2) \\ \vdots \\ b_{map} + k_{map}\, g_x(t_i) = g_y(t_i) \\ \vdots \\ b_{map} + k_{map}\, g_x(t_n) = g_y(t_n) \end{cases} \tag{5.2a}$$

and

$$\begin{cases} b_{rad} + k_{rad}\, g_r(t_1) = g_z(t_1) \\ b_{rad} + k_{rad}\, g_r(t_2) = g_z(t_2) \\ \vdots \\ b_{rad} + k_{rad}\, g_r(t_i) = g_z(t_i) \\ \vdots \\ b_{rad} + k_{rad}\, g_r(t_n) = g_z(t_n) \end{cases}. \tag{5.2b}$$

The recording components of seismic data have a zero mean and the lines of the linear equations above will pass through zero. Therefore the “b” components of each of the linear equations will be assumed to be zero, giving the following sets of equations.

$$\begin{cases} k_{map} g_x(t_1) = g_y(t_1) \\ k_{map} g_x(t_2) = g_y(t_2) \\ \vdots \\ k_{map} g_x(t_i) = g_y(t_i) \\ \vdots \\ k_m g_x(t_n) = g_y(t_n) \end{cases} \tag{5.3a}$$

and

$$\begin{cases} k_{rad} g_r(t_1) = g_z(t_1) \\ k_{rad} g_r(t_2) = g_z(t_2) \\ \vdots \\ k_{rad} g_r(t_i) = g_z(t_i) \\ \vdots \\ k_{rad} g_r(t_n) = g_z(t_n) \end{cases}. \tag{5.3b}$$

In matrix form they can be written as

$$\boldsymbol{G_x k_{map}} = \boldsymbol{d_y} \tag{5.4a}$$

and

$$\boldsymbol{G_r k_{rad}} = \boldsymbol{d_z} \tag{5.4b}$$

where $\boldsymbol{k_m}$ and $\boldsymbol{k_r}$ denote two vectors of a single parameter to be evaluated as the dominant linearities on map and radial sections respectively. $\boldsymbol{G_x}$ and $\boldsymbol{G_r}$ denote two column vectors:

$$\boldsymbol{G_x} = \begin{bmatrix} g_x(t_1) \\ g_x(t_2) \\ \vdots \\ g_x(t_i) \\ \vdots \\ g_x(t_n) \end{bmatrix} \tag{5.5a}$$

and

$$\boldsymbol{G_r} = \begin{bmatrix} g_r(t_1) \\ g_r(t_2) \\ \vdots \\ g_r(t_i) \\ \vdots \\ g_r(t_n) \end{bmatrix} \tag{5.5b}$$

On the map view and the radial section $\boldsymbol{d_y}$ and $\boldsymbol{d_z}$ denote vectors of the observation samples along *y* and *z* recording components at that given 3C geophone with following representations:

$$\boldsymbol{d_y} = \begin{bmatrix} g_y(t_1) \\ g_y(t_2) \\ \vdots \\ g_y(t_i) \\ \vdots \\ g_y(t_n) \end{bmatrix} \tag{5.6a}$$

and

$$\boldsymbol{d_z} = \begin{bmatrix} g_z(t_1) \\ g_z(t_2) \\ \vdots \\ g_z(t_i) \\ \vdots \\ g_z(t_n) \end{bmatrix}. \tag{5.6b}$$

The simple least squares solutions to Equation 5.4(a) and Equation 5.4(b) are to be

$$\boldsymbol{G_x}^{\boldsymbol{T}}\boldsymbol{G_x}\boldsymbol{k_{map}} = \boldsymbol{G_x}^{\boldsymbol{T}}\boldsymbol{d_y} \text{ or } \boldsymbol{k_{map}} = (\boldsymbol{G_x}^{\boldsymbol{T}}\boldsymbol{G_x})^{-\mathbf{1}}\boldsymbol{G_x}^{\boldsymbol{T}}\boldsymbol{d_y} \tag{5.7a}$$

and

$$\boldsymbol{G_r}^{\boldsymbol{T}}\boldsymbol{G_r}\boldsymbol{k_{rad}} = \boldsymbol{G_r}^{\boldsymbol{T}}\boldsymbol{d_z} \text{ or } \boldsymbol{k_{rad}} = (\boldsymbol{G_r}^{\boldsymbol{T}}\boldsymbol{G_r})^{-\mathbf{1}}\boldsymbol{G_r}^{\boldsymbol{T}}\boldsymbol{d_z}. \tag{5.7b}$$

Aster et al. (2005) provide a rigorous theoretical verification that the least squares solution to the damped linear system is the maximum likelihood solution to the primary linearity problem. Diagonal weighting matrices are used here to further dampen the random noise.

The weighted linear systems on the basis of equation 5.4a and equation 5.4b are applied and resulted into the following representations:

$$\boldsymbol{G_x^T W_{map} G_x k_{map} = G_x^T W_{map} d_y}$$

or

$$\boldsymbol{k_{map} = (G_x^T W_{map} G_x)^{-1} G_x^T W_{map} d_y} \quad (5.8a)$$

and

$$\boldsymbol{G_r^T W_{rad} G_r k_{rad} = G_r^T W_{rad} d_z}$$

or

$$\boldsymbol{k_{rad} = (G_r^T W_{rad} G_r)^{-1} G_r^T W_{rad} d_z} \quad (5.8b)$$

where $\boldsymbol{W_{map}}$ and $\boldsymbol{W_{rad}}$ are diagonal matrices with weighting diagonal components defined as $diag(\boldsymbol{W_{map}}) = [g_x^2(t_1) + g_y^2(t_1),\ g_x^2(t_2) + g_y^2(t_2), \dots\ g_x^2(t_i) + g_y^2(t_i) \dots,\ g_x^2(t_m) + g_y^2(t_m)]$ and $diag(\boldsymbol{W_{rad}}) = [g_r^2(t_1) + g_z^2(t_1),\ g_r^2(t_2) + g_z^2(t_2), \dots\ g_r^2(t_i) + g_z^2(t_i) \dots,\ g_r^2(t_m) + g_z^2(t_m)]$, on the map and the radial section respectively. Each component is evaluated from the 2-norm or Euclidean length of the line vector derived at a 3C geophone. Hence the dominant linearity in this way will be biased to the signal incident at that geophone, which further damp random noise.

Hodogram of high-noise data (SNR=3) exhibit little linear orientation on either plane of the map view and the radial section. Hence both are difficult to identify and derive accurately even with a rigorous mathematical method. Therefore, noise attenuation is required to enhance the hodogram linearity to obtain the sufficient confidence in the established parameters.

The joint procedure of both the pre-processing of noise attenuation and the following linearity approximation has been implemented within the MATLAB

environment. The joint effects are examined in Figure 5.3, where various noise attenuation methods are used.

It can be observed in Figures 5.3e and f that the NSS process produces a straight line (cyan) in each hodogram. This is because NSS uses an estimated replacement wavelet for each trace. However, the estimated wavelet is never perfect; there is a deviation between the true propagation (red lines) and the approximated direction (cyan lines). Hence it can be also observed that the linearity approximates (blue lines) coincide with the 'noise-free' or 'signal-only' hodograms (cyan lines).

It can also be observed in Figure 5.3 that the maximum noise attenuation is associated with the three-process approach, namely (f) is the combination of *bp*-filter, *Mm*-stack, and NSS. The second best approach is the two-process approach of (d) *bp*-filter and *Mm*-stack.

The best noise attenuation approach is then chosen to join with the weighted least squares regressing process and other post-processes to locate microseismic hypocenters. This 2D hodogram polarization analysis approach is used in synthetic experiments and tested in later chapters. However, including more noise attenuation increases the computational expense. Therefore the second best noise attenuation approach might be a more appropriate choice for projects with a large data volume.

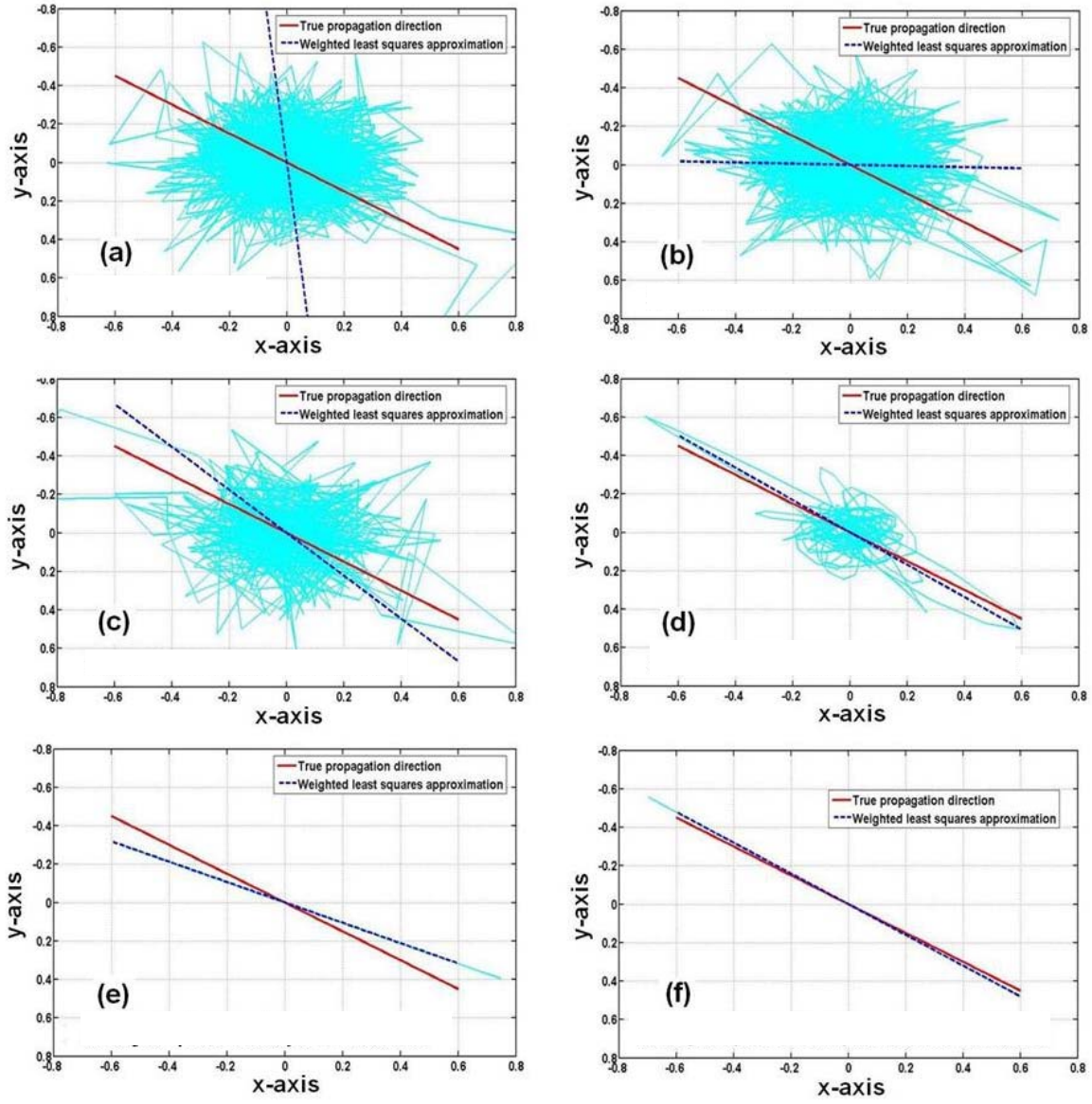

Figure 5.3: The hodogram linearity approximation using weighted least squares regression on (a) raw data and noise attenuation with (b) *bp*-filter, (c) *Mm*-stack, (d) *Mm*-stack and NSS, (e) *bp*-filter and NSS, and (f) *bp*-filter, *Mm*-stack, and NSS.

It should be emphasized that the 2D hodogram approach proposed above might be limited to a single and vertical well monitoring scenario. This Cylindrical system is applicable to the vertical well as illustrated in Figure 5.4(a). Ray paths between the source and receiver are shown confined to a vertical plane. Part (b) of this figure shows a plan view on the left and a radial plane on the right. When noise of SNR=3 is added to

the traces, the plan and radial view are shown in Figure 5.5. Now there is a fan of back projected ray paths on the plan view, and numerous intersections of the raypaths on the radial view.

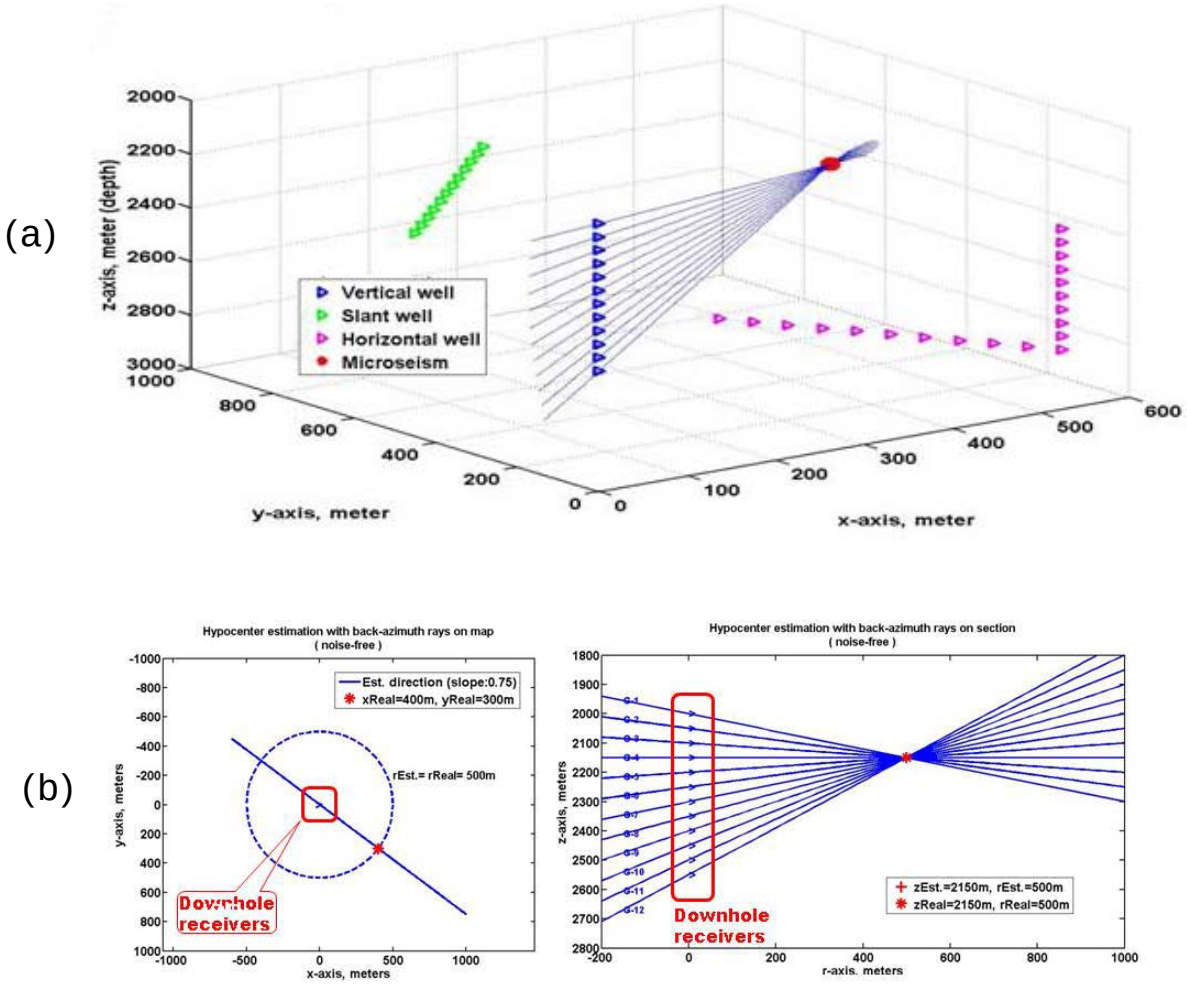

Figure 5.4: The limited applicability of the 2D approach of hodogram analysis. (a) For the vertical array of 3C geophones, raypaths consist of a strict vertical plane. (b) The plan view (left) and the radial section view (right) of part (a).

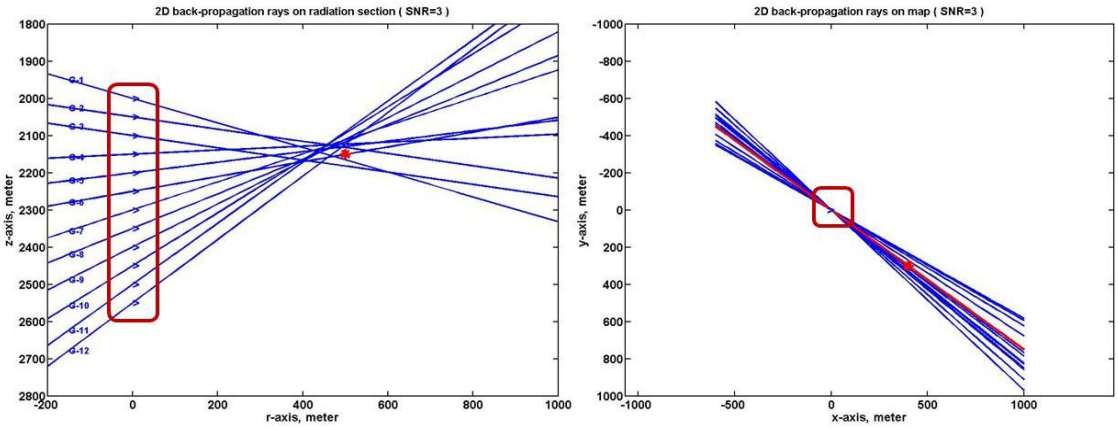

Figure 5.5: The effectiveness of the 2D approach of hodogram analysis on noisy data. Resulted from synthetic data at SNR=3, the approximated propagations from the radial section (left) and the map (right) are less deviated from true propagations as shown in Figure 5.4(b).

All the intersections on the radial plane can be used to provide a mean and standard deviations of the source location.

It is emphasized that projecting the ray paths on to a 2D vertical radial plane cause all the ray paths to intersect with each other, enabling a simple computation to identify the location. This is in contrast to the 3D volume where the raypaths, rarely, if ever, intersect.

Consequently, this 2D approach is efficient if the recording geometry is in a single vertical well and is not appropriate for a 3D multi-type and/or multi-well monitoring system. The solution for a 3D system of wells is presented in the following section.

5.2 The 3D approach of hodogram polarization analysis

When the geophones are not confined to a vertical well, a more general solution is required and referred to as the 3D approach. This 3D approach is on the base of the

weighted least squares regression. The following linear equations define a line in 3D space that represents a ray path. They are used to extract the dominant linearity of a 3D hodogram, where (*x*, *y*, *z*) is any point on the line, i.e.,

$$\begin{cases} x_0 + a \cdot n_x = x \\ y_0 + a \cdot n_y = y. \\ z_0 + a \cdot n_z = z \end{cases} \tag{5.9}$$

The triplet (x_0, y_0, z_0) is a known point on the line, such as the center of a hodogram and (n_x, n_y, n_z) is a set of direction numbers (unit vectors) to be evaluated at each time sample, with the variable parameter a along the expected direction. Within microseismic monitoring scenarios herein, each component of (n_x, n_y, n_z) will be evaluated independently for each geophone by the following linear systems:

$$\begin{cases} a_1 n_x = g_x(t_1) - g_x(t_0) \\ a_2 n_x = g_x(t_2) - g_x(t_0) \\ a_3 n_x = g_x(t_3) - g_x(t_0) \\ \vdots \\ a_m n_x = g_x(t_m) - g_x(t_0) \end{cases} \tag{5.10a}$$

$$\begin{cases} a_1 n_y = g_y(t_1) - g_y(t_0) \\ a_2 n_y = g_y(t_2) - g_y(t_0) \\ a_3 n_y = g_y(t_3) - g_y(t_0) \\ \vdots \\ a_m n_y = g_y(t_m) - g_y(t_0) \end{cases} \tag{5.10b}$$

$$\begin{cases} a_1 n_z = g_z(t_1) - g_z(t_0) \\ a_2 n_z = g_z(t_2) - g_z(t_0) \\ a_3 n_z = g_z(t_3) - g_z(t_0) \\ \vdots \\ a_m n_z = g_z(t_m) - g_z(t_0) \end{cases} \tag{5.10c}$$

where $(g_x(t_i), g_y(t_i), g_z(t_i))$ represents the components of recording respectively at the time t_i for that given geophone. In matrix form they may be written as

$$\begin{bmatrix} a_1 \\ a_2 \\ a_3 \\ \vdots \\ a_m \end{bmatrix} n_x = \begin{bmatrix} g_x(t_1) - g_x(t_0) \\ g_x(t_2) - g_x(t_0) \\ g_x(t_3) - g_x(t_0) \\ \vdots \\ g_x(t_m) - g_x(t_0) \end{bmatrix} \; or \; \boldsymbol{Gn_x = d_x} \tag{5.11a}$$

$$\begin{bmatrix} a_1 \\ a_2 \\ a_3 \\ \vdots \\ a_m \end{bmatrix} n_y = \begin{bmatrix} g_y(t_1) - g_y(t_0) \\ g_y(t_2) - g_y(t_0) \\ g_y(t_3) - g_y(t_0) \\ \vdots \\ g_y(t_m) - g_y(t_0) \end{bmatrix} \; or \; \boldsymbol{Gn_y = d_y} \tag{5.11b}$$

$$\begin{bmatrix} a_1 \\ a_2 \\ a_3 \\ \vdots \\ a_m \end{bmatrix} n_z = \begin{bmatrix} g_z(t_1) - g_z(t_0) \\ g_z(t_2) - g_z(t_0) \\ g_z(t_3) - g_z(t_0) \\ \vdots \\ g_z(t_m) - g_z(t_0) \end{bmatrix} \; or \; \boldsymbol{Gn_z = d_z}, \tag{5.11c}$$

where $\boldsymbol{G}$ represent the reference parameters of a_i determined by the 2-norm or Euclidean length of $\left[g_x(t_i) - g_x(t_0),\ g_y(t_i) - g_y(t_0),\ g_z(t_i) - g_z(t_0)\right]$, which is $\sqrt[2]{g_x^2(t_i) + g_y^2(t_i) + g_z^2(t_i)}$. As in the 2D case the amplitudes are assumed to have zero mean.

The least squares solution to the above formula are then:

$$\boldsymbol{n_x} = (\boldsymbol{G^T G})^{-1} \boldsymbol{G^T d_x}, \tag{5.12a}$$

$$\boldsymbol{n_y} = (\boldsymbol{G^T G})^{-1} \boldsymbol{G^T d_y}, \tag{5.12b}$$

$$\boldsymbol{n_z} = (\boldsymbol{G^T G})^{-1} \boldsymbol{G^T d_z}. \tag{5.12c}$$

To strengthen the signal and further suppress the direction deviation due to random noise, a diagonal weighting matrix is added for each component representation as:

$$\boldsymbol{G^T W_x G n_x} = (\boldsymbol{G})^T \boldsymbol{W_x d_x}, \tag{5.13a}$$

$$\boldsymbol{G^T W_y G n_y} = \boldsymbol{G^T W_y d_y}, \tag{5.13b}$$

$$\boldsymbol{G^T W_z G n_z = G^T W_z d_z},\tag{5.13c}$$

where $\boldsymbol{W_x}$, $\boldsymbol{W_y}$, and $\boldsymbol{W_z}$ are the diagonal weighting matrices determined by

$$diag(\boldsymbol{W_x}) = [g_x^2(t_1), \dots g_x^2(t_i), \dots g_x^2(t_m)],\tag{5.14a}$$

$$diag(\boldsymbol{W_y}) = [g_y^2(t_1), \dots g_y^2(t_i), \dots g_y^2(t_m)],\tag{5.14b}$$

$$diag(\boldsymbol{W_z}) = [g_z^2(t_1), \dots g_z^2(t_i), \dots g_z^2(t_m)].\tag{5.14c}$$

Solutions to the above linear systems are still the weighted sample or observational average

$$\boldsymbol{n_x = (G^T W_x G)^{-1} G^T W_x d_x},\tag{5.15a}$$

$$\boldsymbol{n_y = (G^T W_y G)^{-1} G^T W_y d_y},\tag{5.15b}$$

$$\boldsymbol{n_z = (G^T W_z G)^{-1} G^T W_z d_z},\tag{5.15c}$$

where weights are similar but more noise tolerant than solutions represented by equations 5.12.

In a simple earth model with a homogenous and isotropic velocity, propagation rays are linear, and in a noise-free environment should point back to the hypocenter location as illustrated in Figure 5.6(a). Lines that represent raypaths pass through the source and each geophone. The perspective view is on the left and a map view on the right. However, noise will once again perturb the estimated direction of the raypaths from the true directions. The deviation is random and dependent on the noise level, as illustrated in Figure 5.6(b), which has a SNR=10. With this high SNR, the estimated ray paths tend to propagate back to the source location. Estimating that location is discussed in Chapter 6.

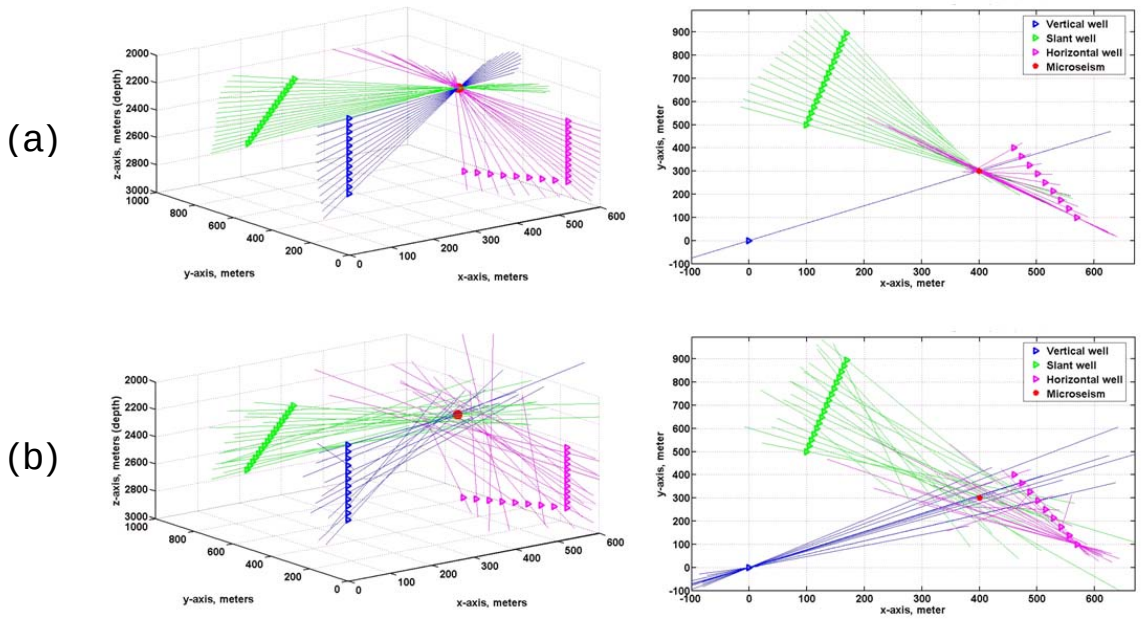

Figure 5.6: Illustration the vectors of each solution of the 3D hodogram polarization analysis at 2 noise levels (a) noise-free and (b) SNR=10, with three (color-coded) wells.

Pre-processing for noise attenuation is also required by the 3D approach of hodogram analysis herein similar to that required for the 2D method.

The applicability of this 3D approach of hodogram polarization analysis is much broader than the 2D approach. It is applicable for multi-type and multi-well microseismic monitoring scenarios, and overcomes the limitation associated with the 2D approach to the single vertical well observation.

5.3 Chapter summary

Both 2D and 3D approaches of hodogram polarization analysis proposed in this chapter employ the optimal noise attenuation schema introduced in Chapter 4, including *bp*-filter, *Mm*-stack, and NSS. The joint procedure of noise attenuation and weighted least squares regression on synthetic microseismograms demonstrate that the hodogram

analysis methodology can obtain the expected noise tolerance at SNR=3 by either approach. With noise present, the weighted least squares regression technique provides a maximum likelihood approximates to propagation directions incident at all 3C geophones.

Chapter Six: Back-propagation analysis for locating the hypocenter

Back-propagation analysis traces P-wave propagation incident at every recording site backward to the location of the microseismic event. It is proposed as an alternative to the commonly used $\tau_s - \tau_p$ method, in which the recording distance to a source is located using the difference in the travel times of the S and P wave arrival times along with the velocities for both the P- and S- wave energy.

Back-propagation methods are presented for both the 2D and 3D approaches. These approaches don't have to indentify and pick travel times of the S-wave energy that is usually contaminated by the preceding P-wave codas. These methods use a statistical optimization approach to define the mean and standard deviation of the estimated hypocenter location.

The 2D planar approach assumes the geophones are in a vertical well. The azimuthal direction to the source location is estimated from map view hodogram. The back-propagated rays are then assumed to b in a vertical plane at this azimuthal analysis of each receiver hodogram analysis from each receiver plots the raypath directions in the radial plane. The intersections of these raypaths provide a mean and standard deviation estimate of the source location.

The 3D approach estimates the source location for an arbitrary location of the geophones. The direction of the ray path from the geophone to the source is estimated from 3D hodogram anomaly. However, in 3D space these raypaths rarely intersect, requiring a spatial process to find an estimated source location from two, non-intersecting ray paths.

Testing of these algorithms uses a model with isotropic and homogeneous velocities. Seismograms were created from a known source to each receiver location and random noise added. The accuracy of the estimated source location was then evaluated for different noise levels.

Back-propagation analysis in either approach uses a statistical optimization method to define the mean location and provide a statistical estimate for the more accurate hypocenter location.

6.1 The 2D approach of back-propagation analysis

Once the seismic propagation direction is obtained from hodogram analysis, ray paths from geophones back towards the seismic hypocenter can be plotted, as shown in Figure 6.1 a, where they are confined to a vertical plane. Pairs of the ray paths on the vertical plane produce intersection points that provide initial estimates of the source locations as illustrated in Figure 6.1b. This figure shows the ray paths in 3D space, along with other receivers in other wells that are not used.

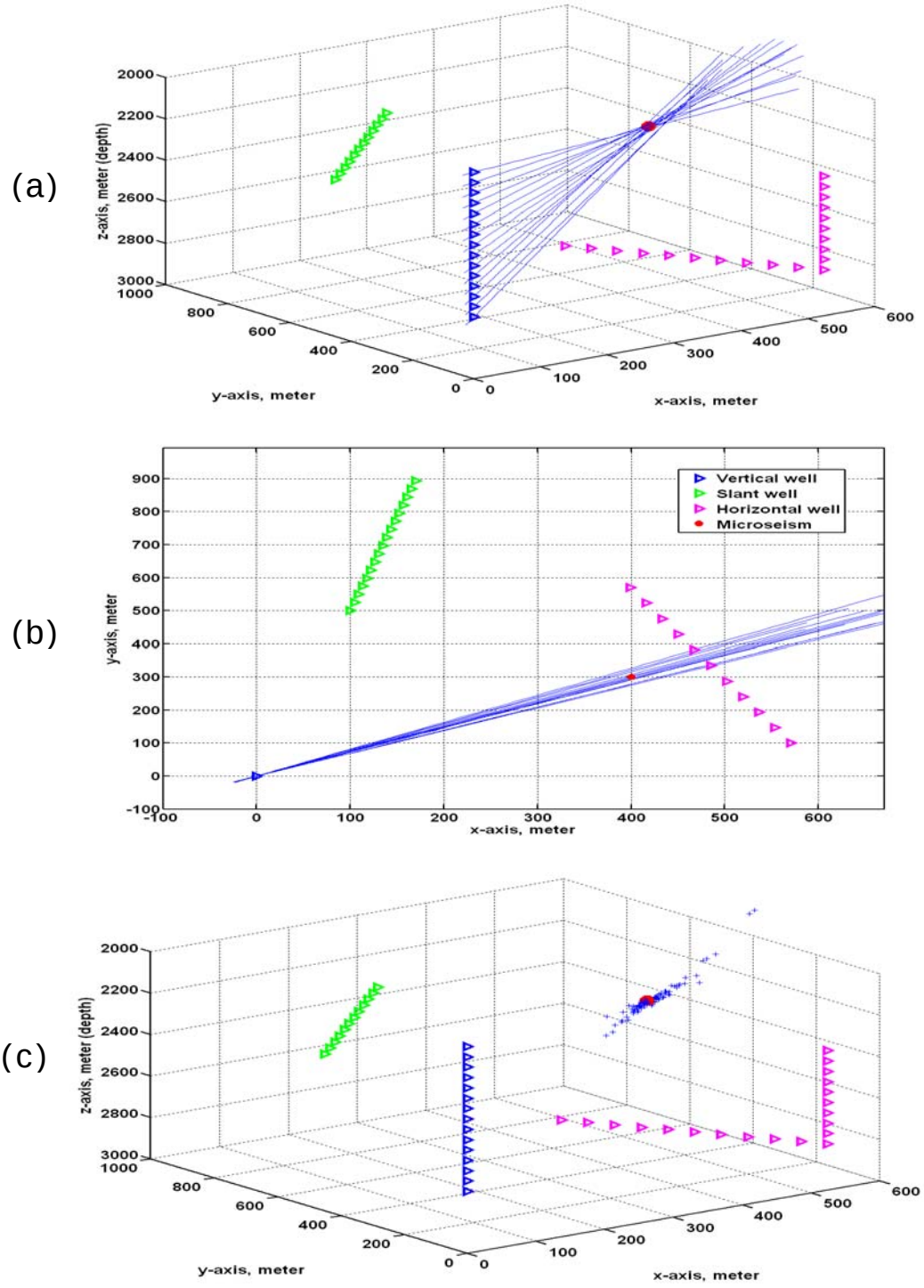

Figure 6.1: Illustration of the 2D approach of back-propagation analysis (in 3D view). It is based on (a) propagations (blue lines) in a vertical array of 3C geophones (blue triangles) to a single microseism (red dot), (b) the map projection of propagation raypaths, and (c) nearest points (blue crosses) of mutual raypaths to be projected on the radial section. The well is shown in a 3D volume with receivers in other wells (non-blue triangles) that are not used.

The 2D approach of back-propagation analysis is approached with the same two planes as used in this hodogram analysis, i.e., the vertical radial section and the map view section.

It should be noted that the planar or 2D approach of back-propagation analysis is appropriate only for a single vertical well and not for applications with for example the slant well (green triangles in Figure 6.1), and/or the combination horizontal well (pink triangles in Figure 6.1).

6.1.1 Determining clustering azimuths on map plane

The 2D hodogram analysis of the map view provides azimuthal estimates from each receiver. A vertical array of 15 geophones produces 15 azimuthal directions when projected on the map view. In the absence of noise all raypath are in a vertical plane as illustrated in Figure 6.2. The vertical well is located at (0, 0).

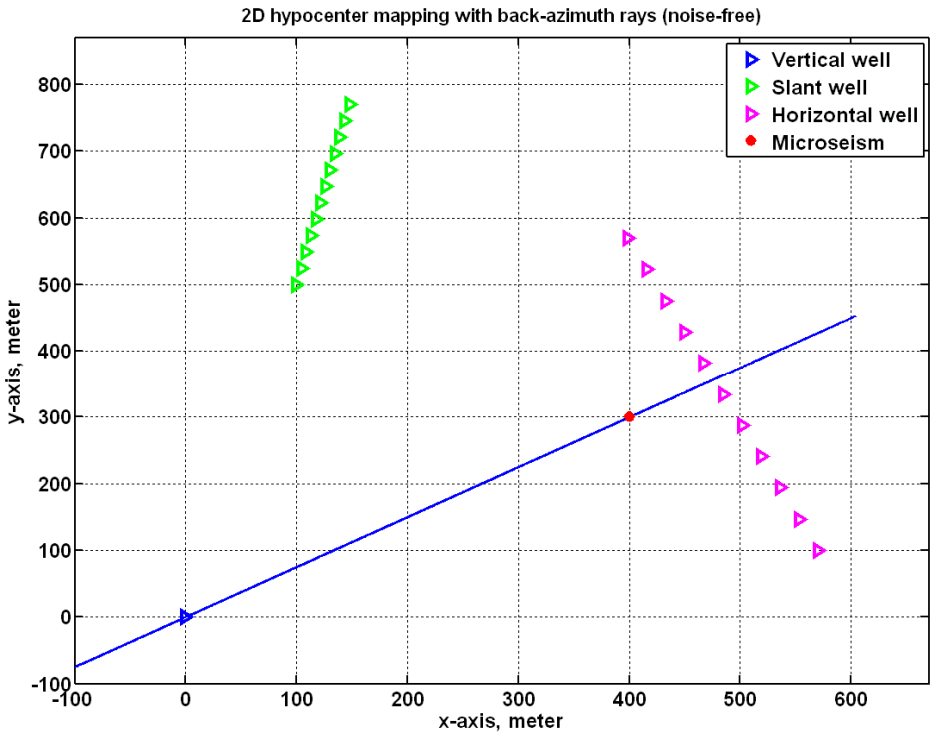

Figure 6.2: A map view of the raypaths in the absence of noise. The angular location of the Cartesian coordinate system for the vertical well (blue triangle) to the injection well (red dot) defines the *x*-axis, but only for the vertical well.

The true azimuth γ, is the angle clock wise from North. I will use a 2D Cartesian coordinate system where the clustering raypaths from the receiver well to the injection well define the *x*-axis. The angle θ will be the measure counter clockwise from this *x*-axis. We can then average the angles to get a mean value.

The azimuthal direction is defined as θ in the Cartesian coordinates system with one vector *x* and *y* given by:

$$x = cos(\theta), \tag{6.1a}$$

$$y = sin(\theta). \tag{6.1b}$$

For convenience, I will use the slope. The functions $cos(\theta)$ and $sin(\theta)$ can be expressed in terms of the slope l of the hodogram on the *x*-*y* plane:

$$cos(\theta) = \mathrm{l}/\sqrt{(l^2+1)}, \tag{6.2a}$$

$$sin(\theta) = l/\sqrt{(l^2+1)}. \tag{6.2b}$$

The Gaussian random noise along *x*-axis and *y*-axis are distributed with standard deviations σ_x and σ_y, giving the azimuth estimates that are randomly deviated from the true azimuth with a standard deviation σ_l. The quantity t_l, with the following definition, is also random and has a Student's ***t*** distribution of

$$t_l = \frac{l-\overline{m_l}}{s_r/\sqrt{n}}, \tag{6.3}$$

where *n* represents for the total number of azimuth samples in the *x*-*y* plane, *l* the sample variable of each individual azimuth, $\overline{m_l}$ the sample mean, and s_r an estimate of the standard deviation σ_l as defined by

$$s_l = \sqrt{\frac{\sum_{i=1}^{n}(l_i-\overline{m_l})^2}{n-1}}. \tag{6.4}$$

To remove the anomalous azimuths, the probability density is then calculated by the following formula:

$$f(t_l|n) = \frac{\Gamma\left(\frac{n+1}{2}\right)}{\Gamma\left(\frac{n}{2}\right)}\frac{1}{\sqrt{n\pi}}\frac{1}{\left(1+\frac{l^2}{n}\right)^{\frac{n+1}{2}}} \tag{6.5}$$

where Γ represents the gamma function (i.e. $\Gamma(x) = \int_0^\infty \xi^{x-1}e^{-\xi}d\xi$).

Hence the previous sample mean $\overline{m_l}$ could be updated to u_l, which is obtained by back-tracing from the mode of the density approximation of azimuth samples by $f(t_l|n)$.

As shown in Figure 6.4, clustering azimuths (blue lines) are located with the criterion:

$$|l - u_l| <= s_l \tag{6.6}$$

where l is the sample variable representing each individual azimuth value , u_l is obtained by back-tracing from the mode of the density approximation by $f(t_l|n)$ from all azimuth samples with the Student's $\boldsymbol{t}$ distribution, and s_l is the standard deviation estimate as defined above.

All incident propagations on the map view (blue and cyan lines) are becoming more clustered around the true azimuth (the red line), as the noise levels are also getting less with decreasing noise levels.

The statistical optimization has been implemented with an iterative option for an improved accuracy of the azimuth estimation. However, as the sample base of azimuths is small in this testing scenario herein and may also be small in practice, therefore the iterative option may not make much difference on the map plane.

(a)

SNR=2

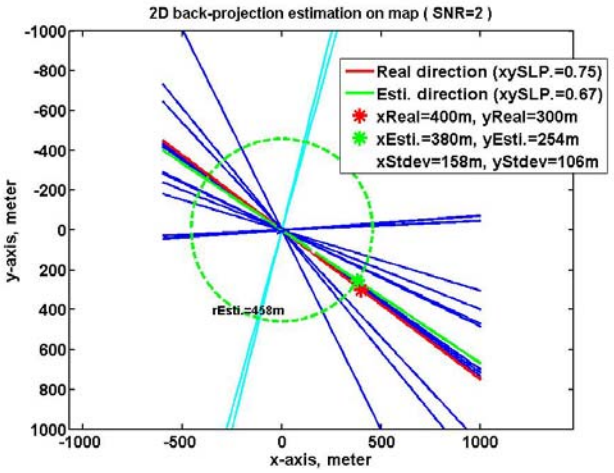

(b)

SNR=2.5

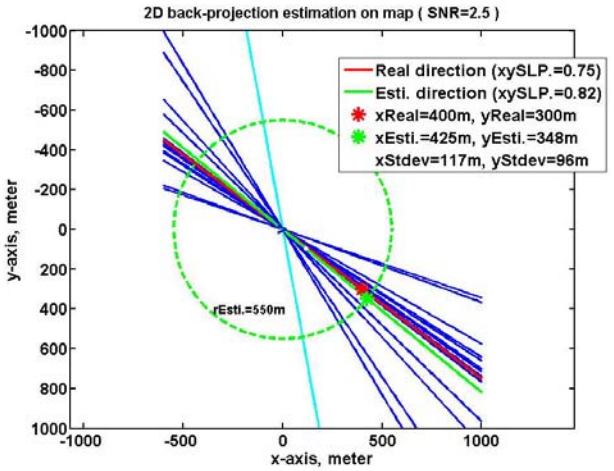

(c)

SNR=3

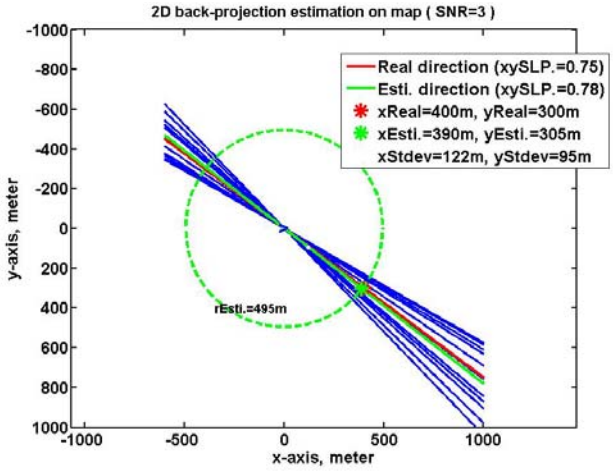

Figure 6.2: Statistical optimization on map. Clustering azimuths (blue lines) and outliers (cyan lines) are determined first, then the azimuth estimate (the green line) to the true azimuth (the red line) is located only from the clustering ones, at three noise levels as (a) SNR=2, (b) SNR=2.5, and (c) SNR=3.

After the azimuth angle θ is determined on the map plane, other two cylindrical coordinates (r_s, z_s) from the well to the source has to be estimated on the radial section as introduced in the following section.

6.1.2 Determining the clustering of mutual intersections on radial plane

I continue the analysis of the geophone configuration of fifteen geophones deployed in a vertical well to monitor a single microseism. The vertical array is located at the radial distance of zero with geophones equally spaced from depths of 2000 m to 2700m, as illustrated in Figure 6.3. The source is at a radial distance of 500 m and a depth of 2150m.

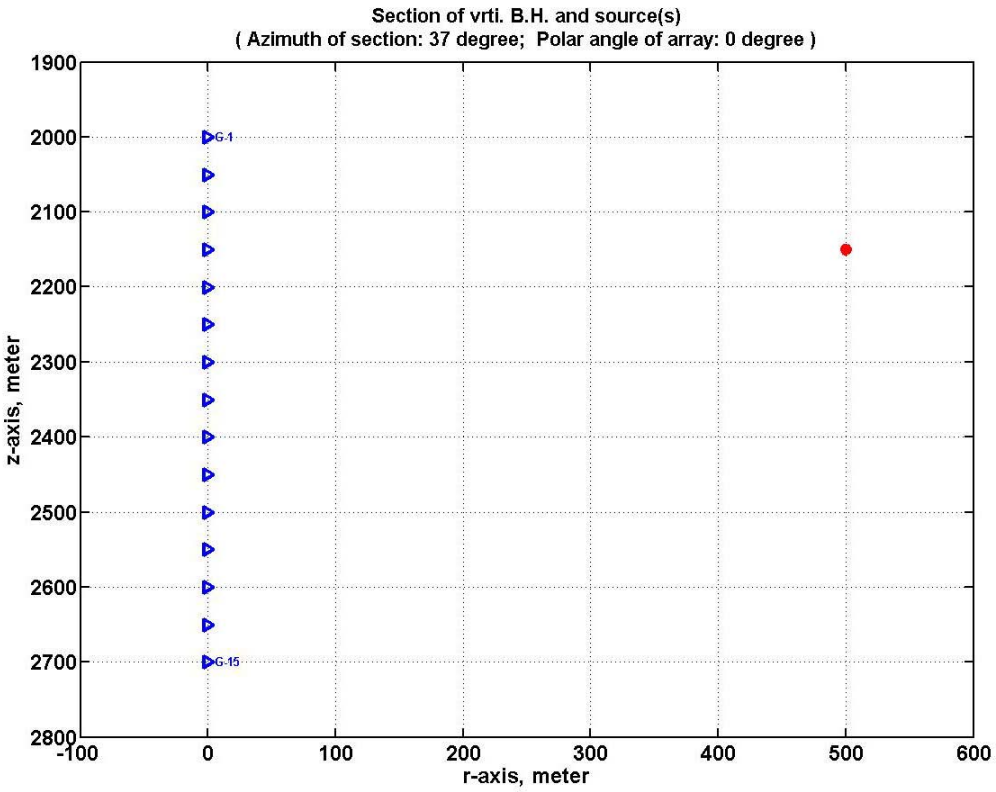

Figure 6.3: The radial section of a single vertical well (blue triangles) monitoring for a single microseismic source (the red dot) has an azimuth of 37 degree, the blue line as shown in Figure 6.2.

With the assumption of a homogenous and isotropic velocity earth, thus there are 15 seismic propagation rays back to the source from all 15 geophones, and each of them can be simply constructed in the radial section by

$$z = z_j + l_j(r - r_j) \tag{6.7}$$

where $(r_j,\ z_j)$ represents the j^{th} geophone location and l_j represents the slop of the propagation ray at that geophone.

Assume there are no parallel rays, and then the combination of all ray pairs out of a total of 15 raypaths, commonly denoted as C_2^{15}, will give 105 mutual intersections. Each intersection is obtained from a corresponding ray pair by

$$\begin{cases} z = z_i + l_i(r - r_i) \\ z = z_j + l_j(r - r_j) \end{cases} \tag{6.8}$$

where (r_i, z_i) and (r_j, z_j) denote two different geophone locations with ray slopes of l_i and l_j passing that two geophones respectively.

To investigate the random noise effect, Gaussian noise is added as a disturbance along *r* and *z* components, randomly and independently, with the standard deviations of σ_r and σ_z respectively. Consequently, the mutual intersections deviated from the hypocenter are assumed to be normally distributed with the expected values of m_r and m_z for the radial distance and depth respectively. According to the sampling theorem, the quantities t_r and t_z from all intersection samples on the radial section or the *r*-*z* plane can be considered to be independent and having a Student's ***t*** distribution with $n - 1$ degrees of freedom (Aster *et al*. 2005):

$$t_r = \frac{r - \bar{m}_r}{s_r/\sqrt{n}}, \tag{6.9a}$$

and

$$t_z = \frac{z-\bar{m}_z}{s_z/\sqrt{n}}, \tag{6.9b}$$

where n represents for the total sample number of intersections available in the radial plane, r and z for the sample variables, $\bar{m}_r$ and $\bar{m}_z$ for the sample means, and s_r and s_z are estimates of the standard deviations σ_r and σ_z , along r and z component traces respectively, as defined by:

$$s_r = \sqrt{\frac{\sum_{i=1}^{n}(r_i-\bar{m}_r)^2}{n-1}}, \tag{6.10a}$$

and

$$s_z = \sqrt{\frac{\sum_{i=1}^{n}(z_i-\bar{m}_z)^2}{n-1}}. \tag{6.10b}$$

If n goes to infinity, and these equations converge to a standard normal distribution, however our data trends to a Student's t distribution, which typically has fatter tails, which are considered to contain the outliers of the clustering intersections.

To construct the confidence intervals of clustering intersections surrounding the hypocenter, the probability densities are calculated along the r-and z-axes respectively by the following formulae:

$$f(t_r|n) = \frac{\Gamma\left(\frac{n+1}{2}\right)}{\Gamma\left(\frac{n}{2}\right)}\frac{1}{\sqrt{n\pi}}\frac{1}{\left(1+\frac{r^2}{n}\right)^{\frac{n+1}{2}}} \tag{6.11a}$$

and

$$f(t_z|n) = \frac{\Gamma\left(\frac{n+1}{2}\right)}{\Gamma\left(\frac{n}{2}\right)}\frac{1}{\sqrt{n\pi}}\frac{1}{\left(1+\frac{z^2}{n}\right)^{\frac{n+1}{2}}} \tag{6.11b}$$

where Γ represents the gamma function (i.e. $\Gamma(x) = \int_0^\infty \xi^{x-1}e^{-\xi}d\xi$).

Thus the previous sample means, $\bar{m}_r$ and $\overline{m}_z$, could now be updated by μ_r and μ_z which are back-tracing values with the maximum probability densities, i.e. $f_{max}(t_r|n)$ and $f_{max}(t_z|n)$ along *r* and *z* axes respectively.

The following criteria are then used to determine the clustering intersections that are closely surround the hypocenter, i.e.,

$$|r - u_r| <= s_r, \tag{6.12a}$$

and

$$|z - u_z| <= s_z. \tag{6.12b}$$

Notice that this above procedure can be applied iteratively, while the optimal iteration number has to be adjusted in practice by a trade off between the need to preserve enough samples for statistical analysis and the desire to cut more outliers to achieve less location uncertainty. The best number of iterations for testing with the geometry in Figure 6.3 was found to be 2. Figure 6.4 contains the estimated hypocenter locations on the radial section for SNRs of 2, 2.5, and 3. Notice that the spread of intersections surrounding the hypocenter shrinks as the noise level decreases from SNR=2 to 2.5 and then 3. The selected intersections are in blue, and the rejected anomalies are in cyan.

(a)

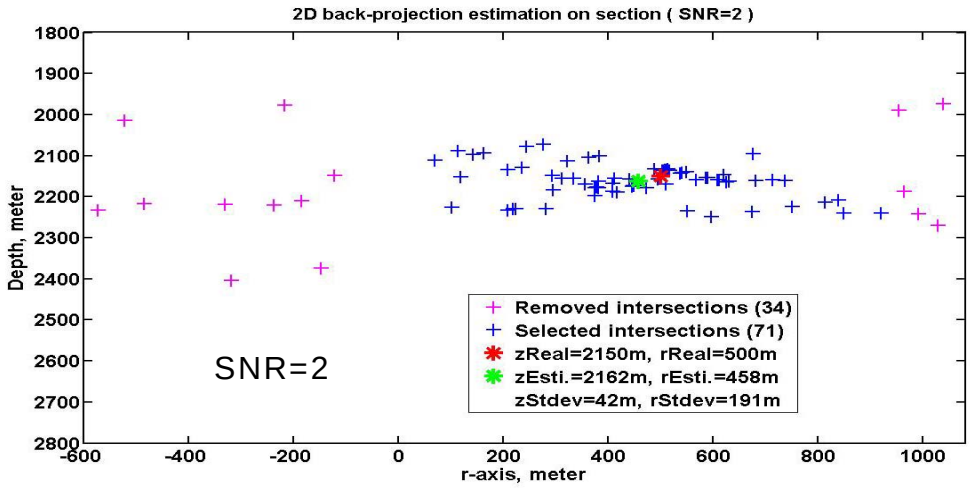

(b)

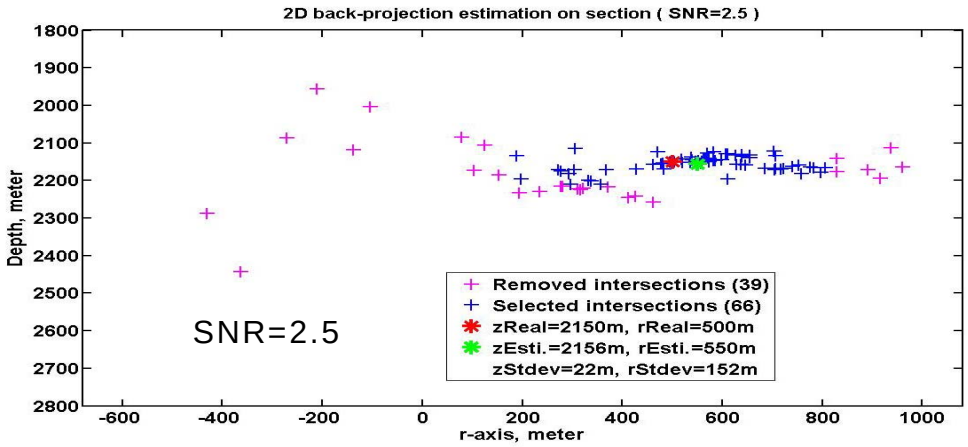

(c)

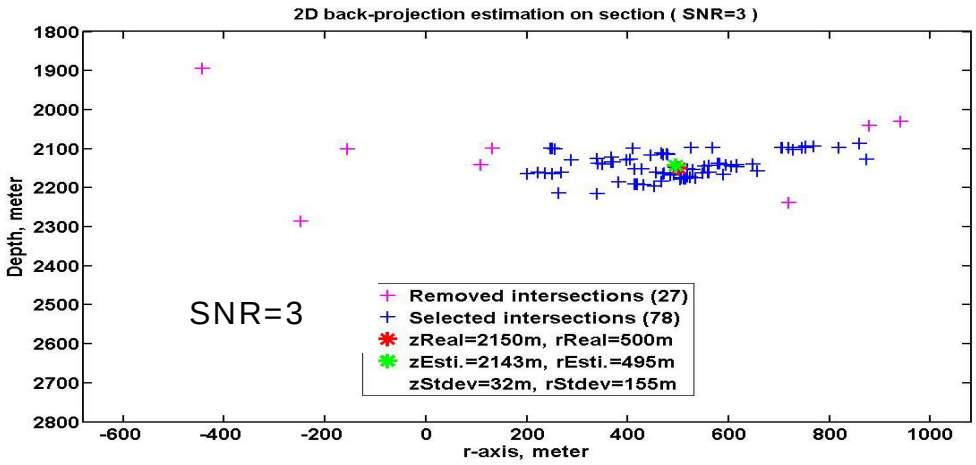

Figure 6.4: Statistical optimization on radial section. Clustering intersections (blue crosses) and outliers (pink crosses) are determined first, then the hypocenter estimate (the green star) to the true location (the red star) is located only from the clustering ones, at three noise levels as (a) SNR=2, (b) SNR=2.5, and (c) SNR=3.

In Figure 6.4 c, the noise tolerance of SNR=3 produces an estimated location of r=495 m and z=2143 m and a standard deviations of $\sigma_r = 155\ m$ and $\sigma_z = 32\ m$ for all selected intersections. This compares favourably with that true location at r=500m and z=2150m.

The overall effectiveness of the 2D back-propagation analysis was investigated under three different displacements (Δz =10 m, 25 m, and 50 m) of the vertical geophone array with two noise levels (SNR=10 and 3). The statistics, as shown in **Table 6.1**, results from 100 random cases for each combination of testing parameters.

In Table 6.1, each set of the hypocenter location estimate (x_s, y_s, z_s) are listed with the mean value first and then the standard deviation.

Table 6.1: Experimental statistics of hypocenter location uncertainty by the 2D approach of hodogram and back-propagation analysis.

Signal to Noise Ratio	Δz (m)	x_s (m)	y_s (m)	z_s (m)
SNR=10	10	**390** ± 28	**292** ± 22	**2148** ± 7
	25	**398** ± 13	**298** ± 10	**2151** ± 3
	50	**401** ± 8	**301** ± 7	**2149** ± 4
SNR=3	10	**264** ± 58	**195** ± 43	**2122** ± 14
	25	**386** ± 37	**286** ± 30	**2151** ± 12
	50	**410** ± 27	**301** ± 23	**2152** ± 15
Hypocenter	Location:	400 m	300 m	2150 m

Intuitively, we expect that larger recording apertures and lower noise levels should result in lower location uncertainties, as confirmed by the statistical results in Table 6.1. It can be observed that as the noise level increases from SNR=10 to SNR=3,

the standard deviation is increasing as well. While standard deviations within a group of each SNR, decrease as the geophone displacement increases from Δz =10 m, to 25m and then 50m, and the mean values of location estimates are getting closer to the true location (x_s=400 m, y_s=300 m, z_s=2150 m) respectively.

In addition to confirming the influence of those parameters that significantly affect the location uncertainty, the statistical summary in Table 6.1 also demonstrates the stability of this 2D approach of back-propagation analysis under expected conditions, by producing the least uncertain locations out of 100 random cases.

It should also be noted that the 2D approach of back-propagation analysis is appropriate only for a single vertical well monitoring scenario, but not for applications with for example the slant well where the ideal or noise-free propagations from multiple receivers to a single source is not in a vertical plane but a slant plane, and for another example the horizontal well where the ideal or noise-free propagations is even not in one plane but two planes, one out of the vertical portion and another out of the horizontal or slant portion of 3C geophones.

In contrast to the limited applicability using the 2D approach, the 3D approach can fit a broad range of applications, as introduced below.

6.2 The 3D approach of back-propagation analysis

The 3D approach estimates the source location directly in a spatial space, instead of two planes in a planar space with the 2D approach.

As illustrated in Figure 6.5, the 3D approach is also a polarization based technique that base on the incident propagation directions from 3C microseismograms as

the raypaths shown in part (a). Then the idea of mutual intersections in the 2D approach is to be converted in the 3D approach. However, most spatial raypaths do not intersect especially when noise background is strong. Therefore, we derive the nearest points to non-intersecting raypaths to compensate the insufficient intersections.

Under ideal or noise-free conditions, the spatial rays, representing the incident propagations at all receivers should have then all intersected at the source location, with the present of a homogenous and isotropic velocity model. However, with the slightest addition of noise and with the limited machine accuracy, the probability of these rays intersecting in 3D space is very small. This is in contrast to the radial section in the 2D approach where intersection is guaranteed.

Consequently we seek to find a point that is closest to the two rays. The point is at the center of a line that has minimum distance between the two rays, as illustrated in Figure 6.6. This figure shows two lines (blue) that represent the two rays, a line (red) that is the minimum distance between the two rays, and the center point (black star) on this line.

The center point is the desired point that is closest to both rays and is referred to as the nearest point or spatial intersection. There are many numerical methods that can be used to find this point. Some methods use axis rotation as illustrated in Figure 6.5b (Pirzadeh and Toussaint, 1998) and some use calculus to find the minimum distance (Bard and Himel, 2001; Sunday, 2010).

The method used here is based on an analytic solution to a variant version of a linear system for every pair of all propagation rays presented in 3D space, as introduced below.

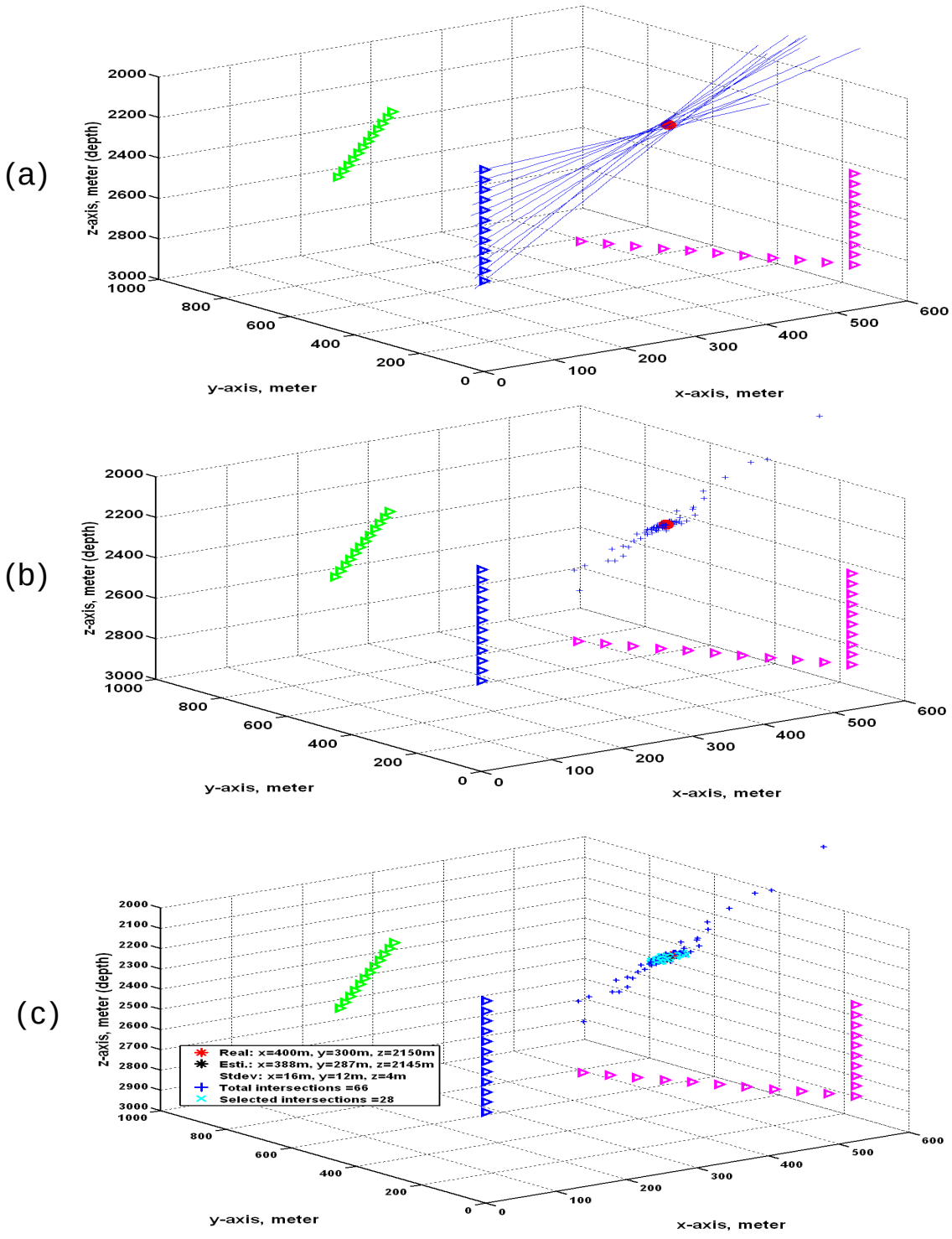

Figure 6.5: Illustration of the 3D approach of back-propagation analysis. With a single vertical well monitoring of a single microseism, the 3D approach derives (a) raypaths (blue lines) first, then (b) nearest points (blue crosses) of mutual raypaths, and finally (c) hypocenter locations from clustering points (cyan crosses) surrounding the hypocenter. The legend in part (c) shows some information about the location estimates.

(a)

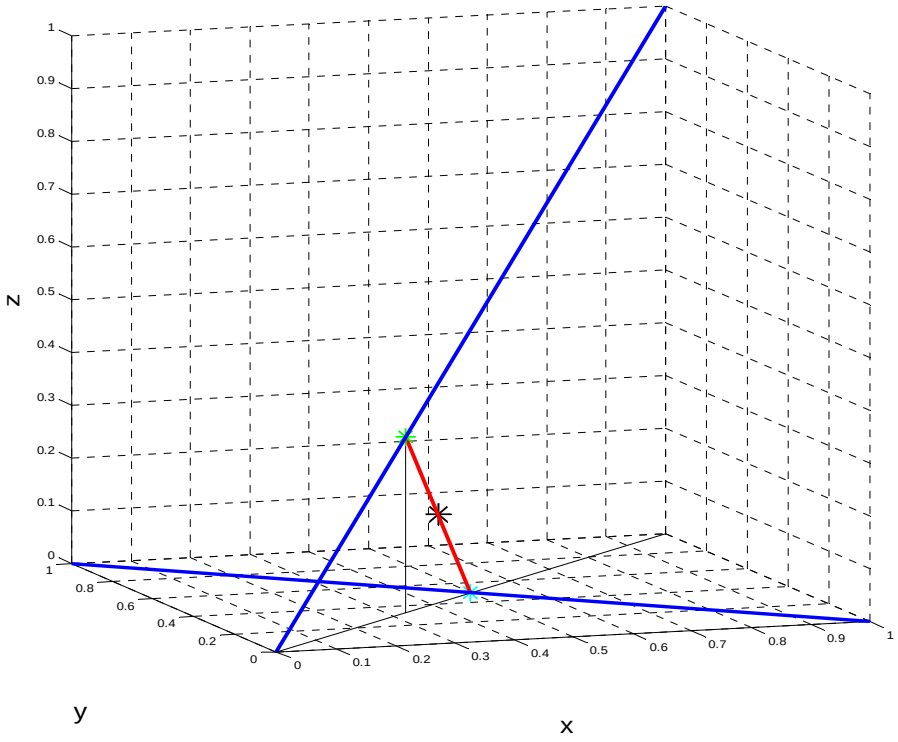

(b)

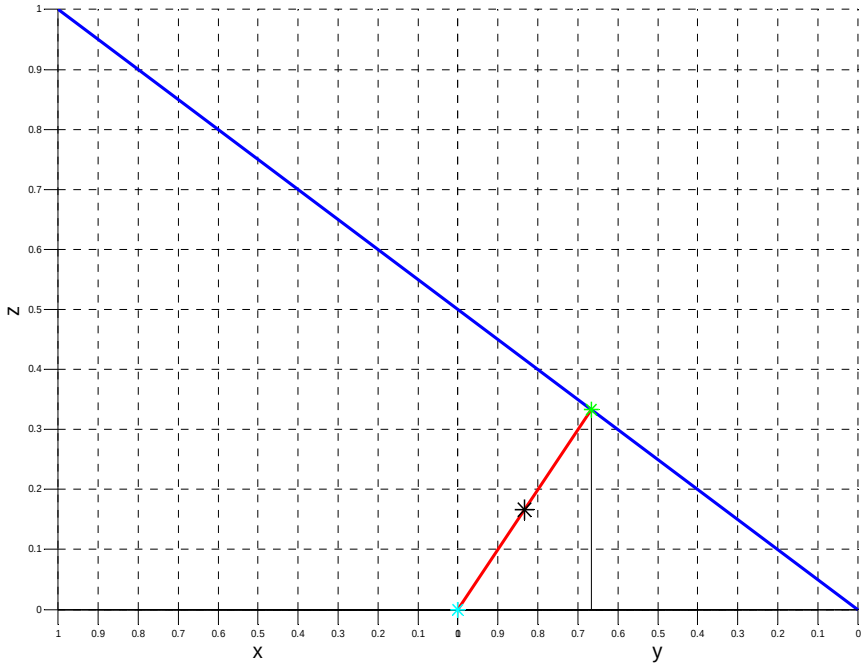

Figure 6.6: The 3D view (a) analytic geometry for computing the nearest approach to two spatial lines (blue lines). The nearest point (black star) to two non-intersecting lines (in blue) is obtained by taking the middle point of two closest on-line points (cyan and green stars). Part (b) shows the projection along the horizontal line located at the green star. This geometrical view can be used to define the shortest distance line and the spatial intersection.

6.2.1 Locating mutual intersections or nearest points in 3D volume

Consider two straight lines in 3D space, l_1 and l_2, originating from two geophone locations:

$$\boldsymbol{r_1} = (x_1,\ y_1,\ z_1) \tag{6.13a}$$

and

$$\boldsymbol{r_2} = (x_2,\ y_2,\ z_2). \tag{6.13b}$$

The spatial directions of both lines, denoted by $\boldsymbol{u_1}$ and $\boldsymbol{u_2}$, are indicated by direction cosines as

$$\boldsymbol{u}_1 = \left(u_{x1},\ u_{y1},\ u_{z1}\right) \tag{6.14a}$$

and

$$\boldsymbol{u_2} = \left(u_{x2},\ u_{y2},\ u_{z2}\right) \tag{6.14b}$$

respectively. The linear equations for both lines can be then constructed as

$$(x_s, y_s, z_s) = (x_1, y_1, z_1) + a_1 \cdot \left(u_{x1}, u_{y1}, u_{z1}\right) \tag{6.15a}$$

and

$$(x_s, y_s, z_s) = (x_2, y_2, z_2) + a_2 \cdot \left(u_{x2}, u_{y2}, u_{z2}\right) \tag{6.15b}$$

where a_1 and a_2 are variable parameters, indicating distances from the microseismic source to the two recording sites respectively. However there is an error in the estimate of unit vectors, due to noise that is denoted as $\boldsymbol{n_1}(n_{x1}, n_{y1}, n_{z1})$ and $\boldsymbol{n_2}(n_{x2}, n_{y2}, n_{z2})$, i.e.,

$$(x_s, y_s, z_s) = (x_1, y_1, z_1) + a_1 \cdot \left(u_{x1}, u_{y1}, u_{z1}\right) + a_1 \cdot (n_{x1}, n_{y1}, n_{z1}) \tag{6.16a}$$

and

$$(x_s, y_s, z_s) = (x_2, y_2, z_2) + a_2 \cdot \left(u_{x2}, u_{y2}, u_{z2}\right) + a_2 \cdot \left(n_{x1}, n_{y1}, n_{z1}\right). \tag{6.16b}$$

In an expanded form, these equations become

$$x_s = x_1 + a_1 u_{x1} + a_1 n_{x1}$$

$$y_s = y_1 + a_1 u_{y1} + a_1 n_{y1}$$

$$z_s = z_1 + a_1 u_{z1} + a_1 n_{z1}$$

$$x_s = x_2 + a_2 u_{x2} + a_2 n_{x2}$$

$$y_s = y_2 + a_2 u_{y2} + a_2 n_{y2}$$

$$z_s = z_2 + a_2 u_{z2} + a_2 n_{z2}. \tag{6.16c}$$

Assuming the random noise presented, finding the intersection of these two lines or an optimal approximate to them both is solved with a linear system out of these expanded equations by the following matrix form

$$\boldsymbol{Gm} = \boldsymbol{d} \tag{6.17}$$

where $\boldsymbol{G}$ denotes a six by five matrix in the following form:

$$G = \begin{bmatrix} 1 & 0 & 0 & -u_{x1} - n_{x1} & 0 \\ 0 & 1 & 0 & -u_{y1} - n_{y1} & 0 \\ 0 & 0 & 1 & -u_{z1} - n_{z1} & 0 \\ 1 & 0 & 0 & 0 & -u_{x2} - n_{x1} \\ 0 & 1 & 0 & 0 & -u_{y2} - n_{y2} \\ 0 & 0 & 1 & 0 & -u_{z2} - n_{z2} \end{bmatrix}, \tag{6.18a}$$

and column vectors of $\boldsymbol{m}$ and $\boldsymbol{d}$ are defined respectively in the following forms

$$\boldsymbol{m} = \begin{bmatrix} x_s \\ y_s \\ z_s \\ a_1 \\ a_2 \end{bmatrix}, \tag{6.18b}$$

and

$$\boldsymbol{d} = \begin{bmatrix} x_1 \\ y_1 \\ z_1 \\ x_2 \\ y_2 \\ z_2 \end{bmatrix}. \tag{6.18c}$$

Testing the 3D solution was evaluated with synthetic data simulated from a 3-type 3-well monitoring scenario for a single microseism, where there are 12, 10, and 22 geophones in vertical-, slant-, and horizontal-well respectively, as color-coded in the following figures. These 44 geophones produce a total of total 946 spatial approximates, as shown in Figure 6.7a, where the SNR=3.

The optimal noise attenuation approach previously introduced in Chapter 4 is integrated with the 3D approach and its effectiveness can then be evaluated via spatial applications, as shown in Figure 6.7. Comparing Figure 6.7a and Figure 6.7b, it is apparent that spatial intersections from noise attenuated data are much more closely clustering around the hypocenter than raw data.

However, even joint with this effective noise attenuation process, there are still many intersections with a large deviation from the hypocenter location, which are considered as outliers and are identified by a statistical approach that is introduced in the following section.

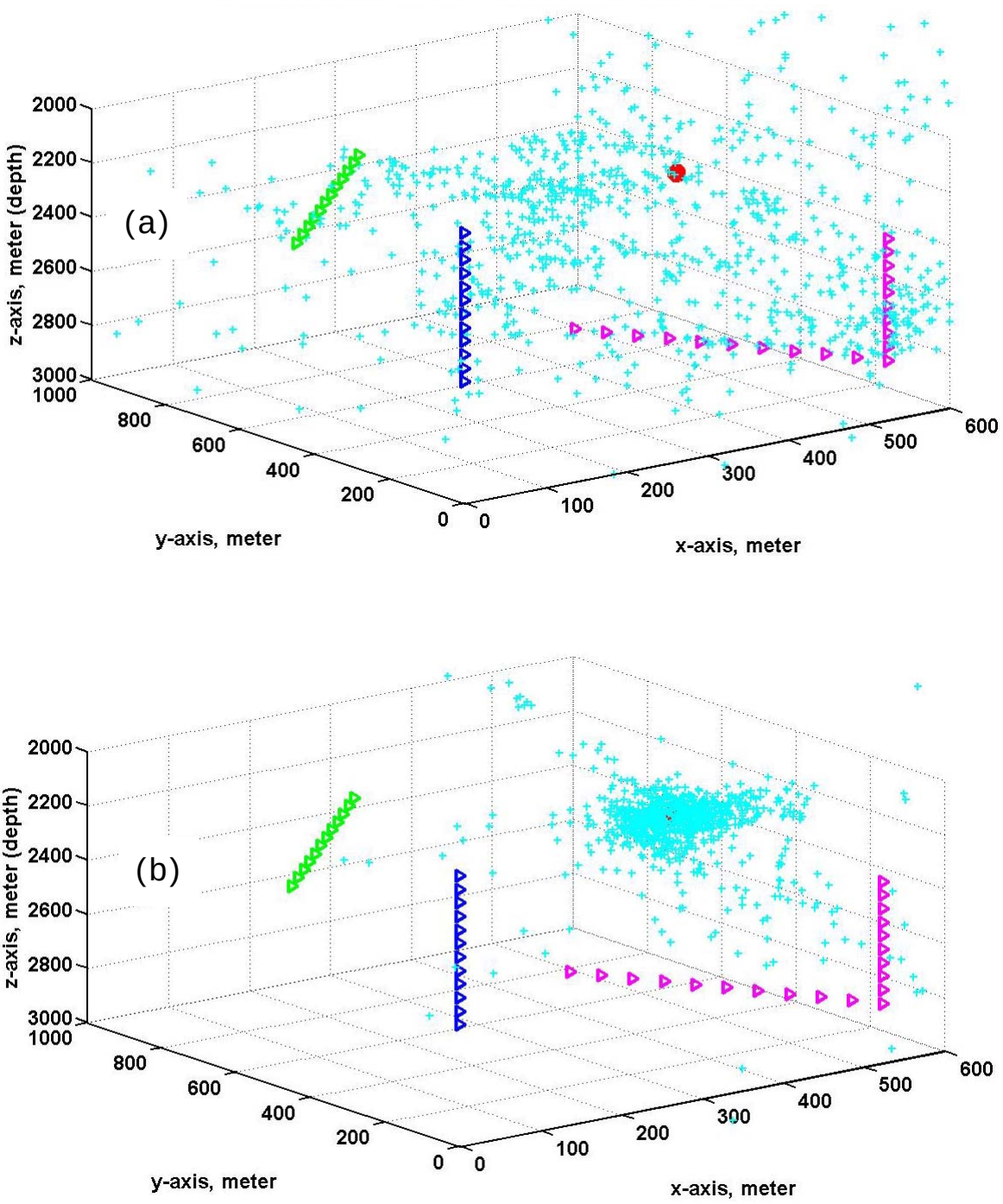

Figure 6.7: Spatial intersections and SVD approximates. With all 3 wells (vertical coded by blue, slant by green, and horizontal by pink triangles) monitoring for a single microseism (the red dot), total 946 intersections or SVD approximates are resulted from (a) raw data and (b) noise attenuated data.

6.2.2 Determining the spatial clustering of mutual intersections or nearest points

Spatial clustering intersections are determined essentially by the same idea of statistical optimization as the planar approach for locating the clustering intersections on radial section, with variants to adapt to the spatial approach.

As random noise along triaxial component traces at each geophone are considered to be independent, all spatial intersections deviated from the single microseismic hypocenter are assumed to be normally distributed along each component trace, and thus the following quantities are independent of each other and have a Student t distribution with n-1 degrees of freedom:

$$t_x = \frac{x-\bar{m}_x}{s_x/\sqrt{n}}, \tag{6.19a}$$

$$t_y = \frac{y-\bar{m}_y}{s_y/\sqrt{n}}, \tag{6.19b}$$

$$t_z = \frac{z-\bar{m}_z}{s_z/\sqrt{n}}, \tag{6.19c}$$

where n represents the total number of samples of intersection available in 3D space, *x*, *y*, and *z* represent sample variables, $\bar{m}_x$, $\bar{m}_y$, and $\bar{m}_z$ are sample means, and s_x, s_y, and s_z are estimates of standard deviations σ_x, σ_r, and σ_z , along the *x*, *y*, and *z* axes respectively, with:

$$s_x = \sqrt{\frac{\sum_{i=1}^{n}(x_i-\bar{m}_x)^2}{n-1}}, \tag{6.20a}$$

$$s_y = \sqrt{\frac{\sum_{i=1}^{n}(y_i-\bar{m}_y)^2}{n-1}}, \tag{6.20b}$$

$$s_z = \sqrt{\frac{\sum_{i=1}^{n}(z_i-\bar{m}_z)^2}{n-1}}. \tag{6.20c}$$

The probability densities are then calculated along the *x*-*y*-*z* axes respectively by the following formulae:

$$f(t_x|n) = \frac{\Gamma\left(\frac{n+1}{2}\right)}{\Gamma\left(\frac{n}{2}\right)} \frac{1}{\sqrt{n\pi}} \frac{1}{\left(1+\frac{x^2}{n}\right)^{\frac{n+1}{2}}}, \tag{6.21a}$$

$$f(t_y|n) = \frac{\Gamma\left(\frac{n+1}{2}\right)}{\Gamma\left(\frac{n}{2}\right)} \frac{1}{\sqrt{n\pi}} \frac{1}{\left(1+\frac{y^2}{n}\right)^{\frac{n+1}{2}}}, \tag{6.21b}$$

$$f(t_z|n) = \frac{\Gamma\left(\frac{n+1}{2}\right)}{\Gamma\left(\frac{n}{2}\right)} \frac{1}{\sqrt{n\pi}} \frac{1}{\left(1+\frac{z^2}{n}\right)^{\frac{n+1}{2}}}, \tag{6.21c}$$

where Γ represents the gamma function (i.e. $\Gamma(x) = \int_0^\infty \xi^{x-1} e^{-\xi} d\xi$).

Hence previous sample means, $\bar{m}_x$, $\bar{m}_y$, and $\bar{m}_z$, could now be updated by μ_r, μ_r, and μ_z, which are obtained from back-tracing from modes of maximum probability densities, i.e. $f_{max}(t_x|n)$, $f_{max}(t_y|n)$, and $f_{max}(t_z|n)$, respectively.

The clustering intersections more closely surrounding the hypocenter are selected by the following criteria:

$$|x - u_x| > s_x, \tag{6.22a}$$

$$|y - u_y| > s_y, \tag{6.22b}$$

$$|z - u_z| > s_z. \tag{6.22c}$$

The above processing series can be applied iteratively, while the optimal number of iteration depends on the particular application and the trade-off between the need to preserve enough samples for statistical analysis and the desire to cut more outliers to achieve less location uncertainty. Figure 6.8 shows the different and similar aspects between iterations=2 and iterations=3 times of statistical optimization.

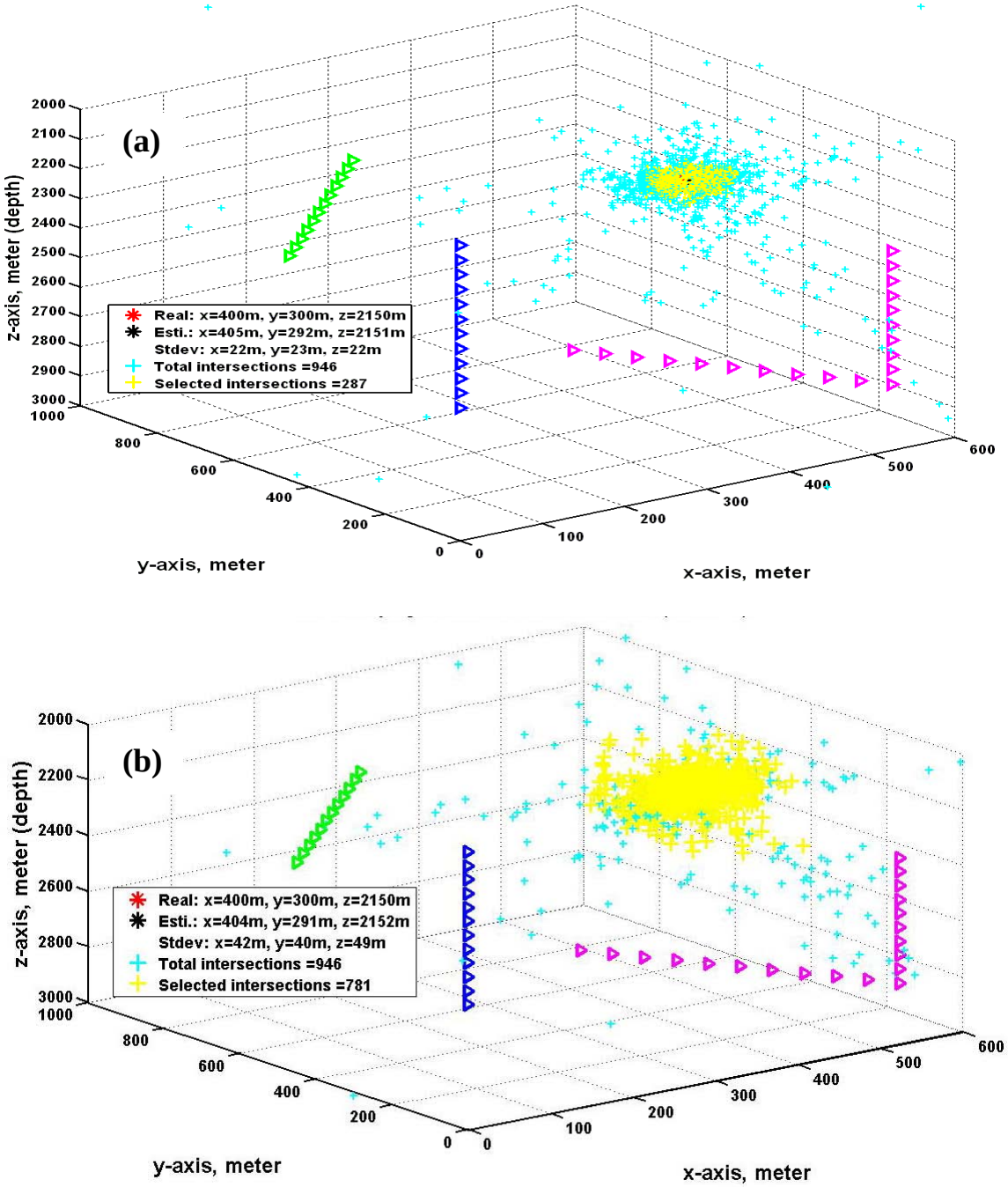

Figure 6.8: Statistical optimization within 3D approach at (a) iterations = 3 and (b) iterations = 2.

It can be observed in Figure 6.8 that as the number of iterations decrease from 3 to 2, the selected intersection (or nearest) points increase from 287 to 781 with the same initial points of 946, the standard deviations increase from 22m to 42m, from 23m to 40m, and

from 22m to 49m along x-, y-, and z-axis respectively. However, the hypocenter location estimates resulted at both iterations are much closer, as illustrated in the legends, with 405m and 404m from the true *x*-coordinate of 400m, 292m and 291m from the true *y*-coordinate of 300m, and 2151m and 2152m from the true *z*-coordinate of 2150m. Therefore, to save the computational cost, the iteration number is chosen to be 2, as resulted and shown in Figure 6.8b. Figure 6.8b, where the real and estimated hypocenter locations are all obscured by those points (cyan and yellow crosses), could be more visible in section views as shown in Figure 6.9.

The 3D method for locating the hypocenter can be applied separately to each single well; there are a greatly reduced number of “intersections” as shown in Figure 6.10.

(a)

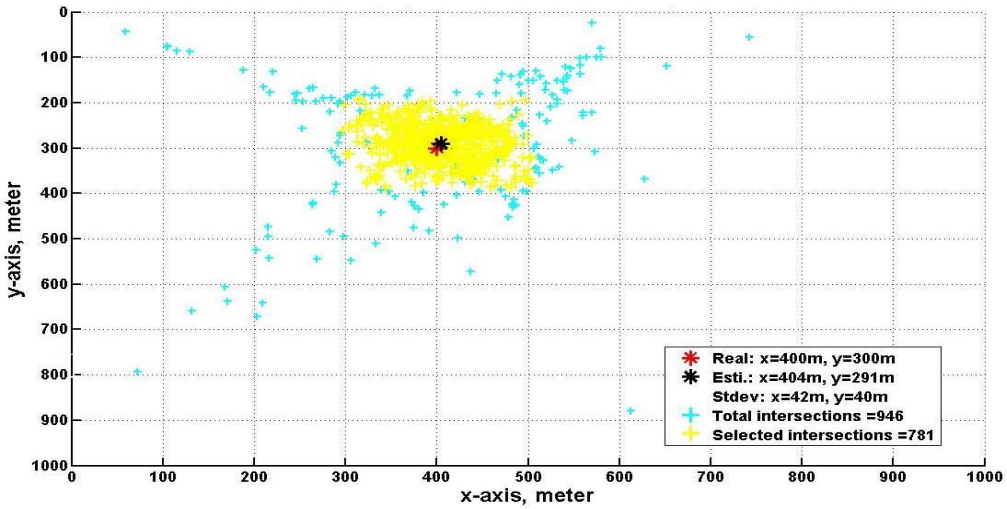

(b)

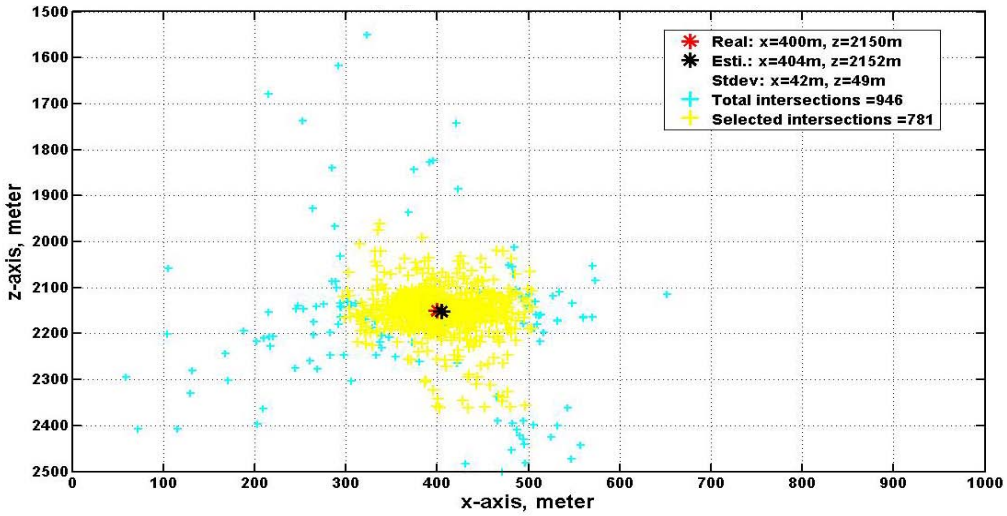

(c)

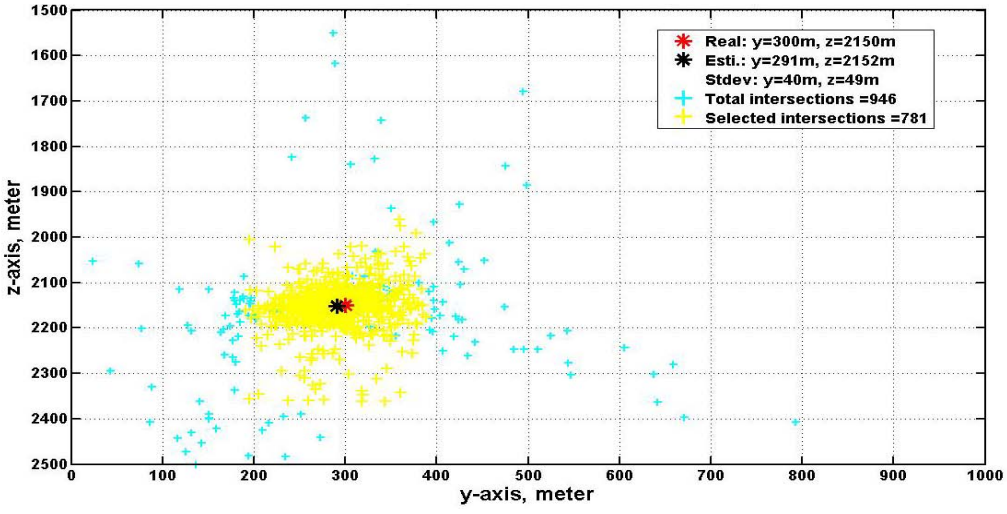

Figure 6.9: Statistical optimization (section views). Projections of Figure 6.7(b) on (a) map or *x-y* plane, (b) *x-z* plane, and (c) *y-z* plane.

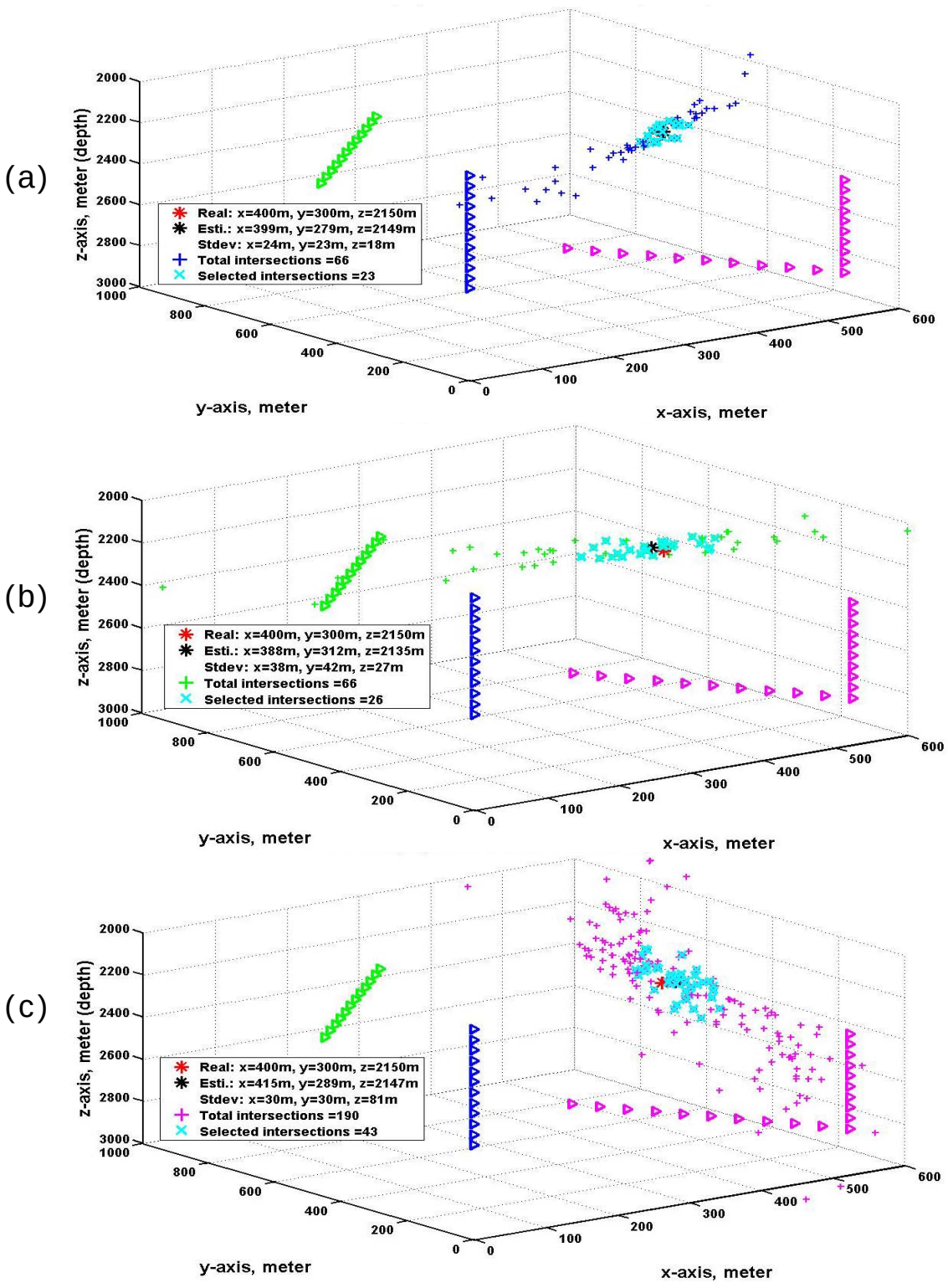

Figure 6.10: The 3D approach of back-propagation analysis derives hypocenter location-estimations (back stars) with (a) the vertical well (blue triangles) alive, (b) the slant well (green triangles) alive, and (c) the horizontal well (pink triangles) alive, monitoring a single microseismic hypocenter at locations (red stars) of the same Cartesian coordinates.

The overall effectiveness of the 3D back-propagation analysis was investigated under three different displacements (Δz =10 m, 25 m, and 50 m) of the vertical, slant, and horizontal geophone arrays together with two noise levels (SNR=10 and 3). The statistics of hypocenter location uncertainty, as shown in **Table 6.2**, results from 30 random cases accumulated for each combination of testing parameters.

It can be observed that as the noise level increases from SNR=10 to SNR=3, the standard deviation is increasing as well, about 2.5 times. However, unlike the 2D approach statistics shown in Table 6.1, standard deviations within the either group of SNRs almost stay at the same level as the geophone displacement increases from Δz =10 m, to 25m and then 50m, and the mean values of location estimates are just getting little closer to the true location (x_s=400 m, y_s=300 m, z_s=2150 m) respectively.

Table 6.2: Experimental statistics of hypocenter location uncertainty by the 3D approach of hodogram and back-propagation analysis.

Signal to Noise Ratio	Δz (m)	x_s (m)	y_s (m)	z_s (m)
SNR=10	10	**400** ± 1.8	**299** ± 2.2	**2150** ± 2.1
	25	**400** ± 1.9	**299** ± 1.7	**2150** ± 1.7
	50	**400** ± 2.5	**300** ± 2.4	**2150** ± 2.3
SNR=3	10	**405** ± 9.0	**294** ± 6.4	**2153** ± 8.2
	25	**405** ± 5.0	**295** ± 6.6	**2155** ± 5.7
	50	**405** ± 7.7	**299** ± 8.9	**2158** ± 7.8
Hypocenter	Location:	400 m	300 m	2150 m

The statistical summary in Table 6.2 also demonstrates the stability of this 3D approach of hodogram and back-propagation analysis under expected conditions, by producing the least uncertain locations out of 50 accumulated random cases. The comparison of Table 6.1 to Table 6.2 indicates us that the 3D approach is much more stable than the 2D approach at worst situations such as SNR=3 and dR=10m or SNR=10 and dR=10m. It also indicates that the 3D approach has much stronger noise tolerance than the 2D approach. And, as mentioned previously, the 3D approach has a broader applicability than 2D approach, and is not limited to the single vertical well monitoring scenarios.

6.3 Chapter summary

Back-propagation analysis is preceded by noise attenuation, hodogram polarization, weighted least squares, SVD, and statistical optimization. The 3D approach has a broader range of applicability appropriate for multi-well multi-type monitoring and the 2D approach spends less computing intensity but only appropriate for single vertical well monitoring.

Tests with a homogenous and isotropic velocity model have produced the hypocenter estimates with much lower location uncertainties by both 2D and 3D approaches implemented with MATLAB software.

Chapter Seven: Conclusion and discussion

The primary goals of this thesis are (1) detection of first arrivals, (2) noise reduction, and (3) hypocenter location.

Weak energy is a character of artificially induced microseisms in a hydrocarbon reservoir, and challenges any hypocenter location method to function appropriately and/or efficiently at low signal to noise ratios. Seeking a more sensitive event-detection trigger was the first step in dealing with the weak energy. As a result, the modified energy ratio (MER) analysis is proposed as being able to capture microseismic arrivals more efficiently at lower signal to noise ratios than other algorithms of energy ratios (ER), including the standard STA/LTA analysis.

To further raise the noise tolerance, several noise attenuation schemes were studied in order to find an optimal one, which significantly improved the arrival-picking accuracy. Once the MER method was joined with the optimal noise attenuation schema, the noise tolerance increased from SNR=3.5 to SNR=1.5.

It should be noted that determining the energy-collecting window length for MER analysis requires more care than for STA/LTA analysis, and hence is subject to change for a particular case, especially for picking multi-arrivals in multi-phases. Further work to determine a general solution fitting various cases would be valuable.

The hodogram analysis method delivers propagation polarization from the first P-wave triaxial incidences at each geophone. The back-propagation analysis then estimates the hypocenter location from the clustering intersections approximated and selected by the SVD technique and the statistical analysis.

Hodogram analysis has the advantage of lower computing cost over eigenvector/eigenvalue analysis, as no matrix regression calculation is involved in any process. Another advantage of using hodogram analysis is the maximum likelihood approximation to polarization information from noisy data, by employing the weighted least squares regression technique.

The back-propagation analysis is then proposed and implemented in both 2D and 3D approaches, as alternatives to τ_S-τ_P methods, to locate the hypocenter. Unlike τ_S-τ_P methods, either approach of back-propagation analysis needs only the first P-arrivals, but not the later S-arrivals. Hence, the computation at cost for picking S arrivals needed by τ_S-τ_P methods is saved by using back-propagation analysis. Another associated advantage is that picking arrivals on noisy data is avoided, as the first P-wave coda usually contaminates the following S-wave. Hence back-propagation analysis has a more confident base to proceed on, and does not necessitate a more sophisticated noise attenuation approach that would otherwise increase the overall computing expense.

Back-propagation analysis is considered being stable and robust for imposed mutual intersections of all spatial back-propagation rays by singular value decomposition (SVD) solutions, along with the further regression to the true location by employing a statistical analysis procedure as well.

The 3D hodogram and back-propagation approach provides the flexibility to handle multi-type and multi-well microseismic monitoring applications.

The overall procedure, encapsulated by noise attenuation, MER time-picking, hodogram polarization analysis, and back-propagation analysis, is stable and requires minimal computational effort, comparing the alternatives.

The development of both 2D and 3D hodogram and back-propagation methods for hypocenter location used only a homogenous and isotropic velocity model in this thesis research. However, the adaption to a layered velocity model should not be difficult theoretically, requiring the combination of refraction and ray-bending results at each layer according to Snell's law.

APPENDIX

Three-well monitoring of a single microseism

Data generation

i. Set up values for flexible parameters:

Source: A single microseism that emits P-wave only, and locates at (400m, 300m, 2150m) in 3-dimensional Cartesian system.

Well: Three wells are used with s vertical well with 12 geophones, a slant well with 15 geophones, and a horizontal well with 20 geophones where 12 are in vertical part and 8 in horizontal part.

The vertical well and the single microseismic source form a vertical section that is setup with the azimuth angle of 37 degree.

The slant well is set up with the azimuth angle of 80 degree.

The horizontal well is set up with the azimuth angle of 110 degree.

All geophones in three wells are displaced in 50 meter.

Model: A homogeneous and isotropic velocity earth with P-wave velocity of 4500m/s.

Noise: Gaussian noise at SNR=3

ii. Data results

Synthetic data results are shown in Figure A1.1 and Figure A1.2.

Methodology testing Phase 1

MER analysis, hodogram analysis, and back-propagation analysis without noise attenuation, as shown in Figure A1.3 and Figure A1.4.

Methodology testing Phase 2

MER analysis, hodogram analysis, and back-propagation analysis with noise attenuation, as shown in Figure A1.5 and Figure A1.6.

Methodology testing Phase 3

Statistical optimization is applied on the results from phase 2, as shown in Figure A1.7 and Figure A1.8.

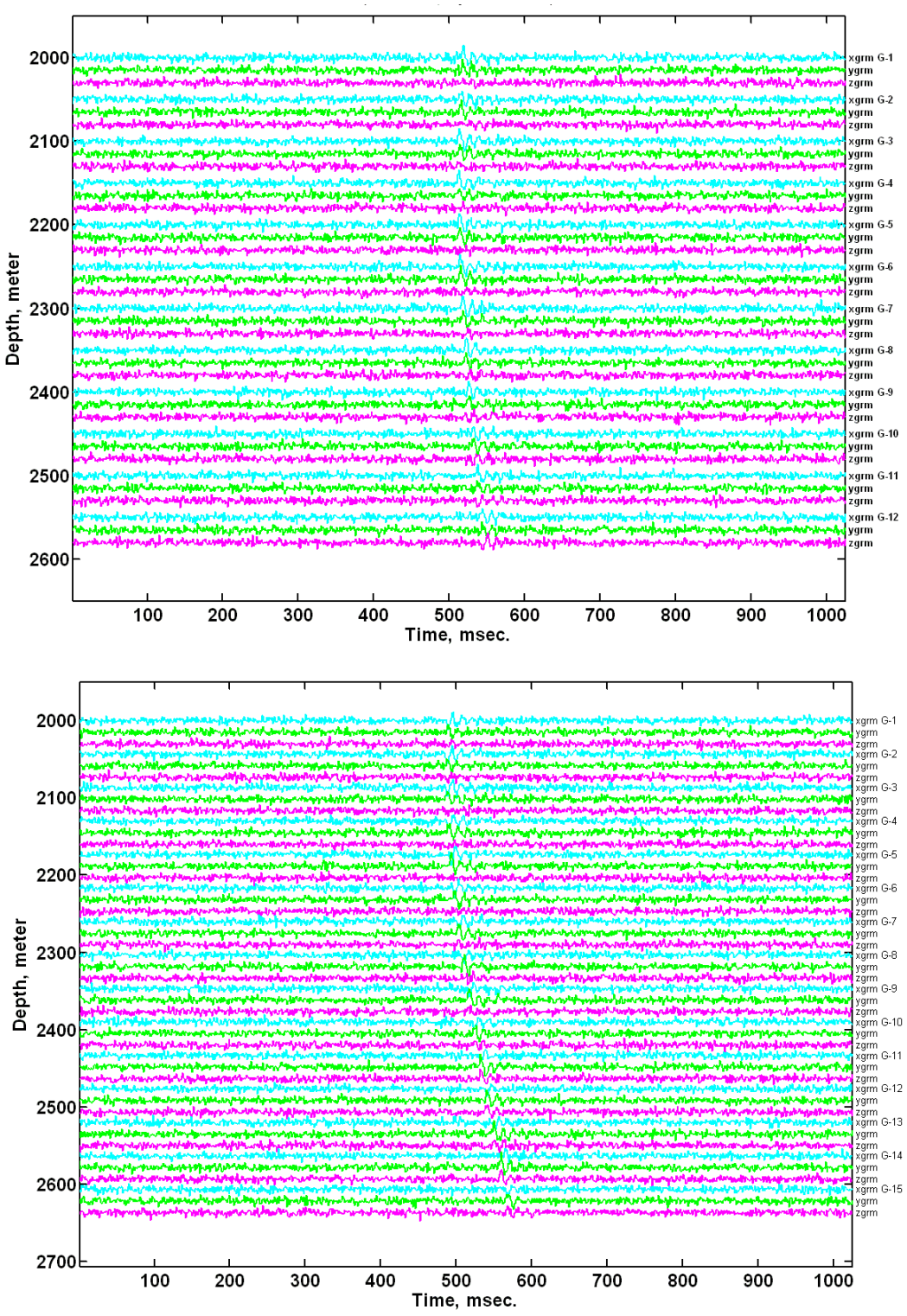

Figure A1.1: Synthetic data from (a) the vertical well, and (b) the slant well.

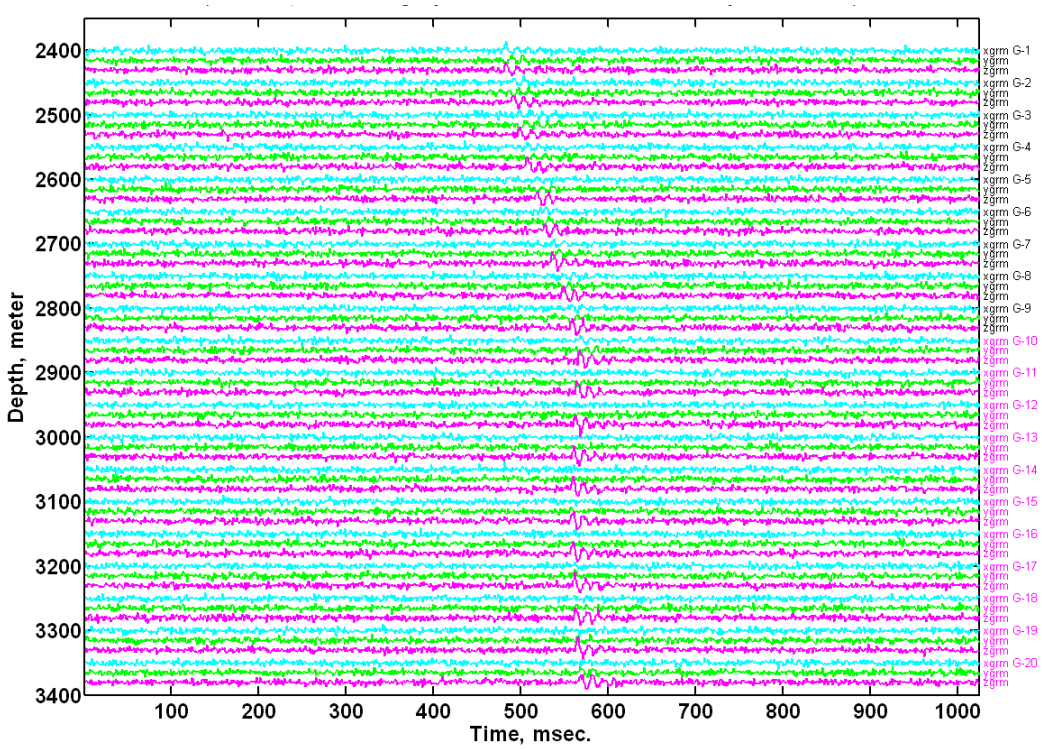

Figure A1.2: Synthetic data from the horizontal well.

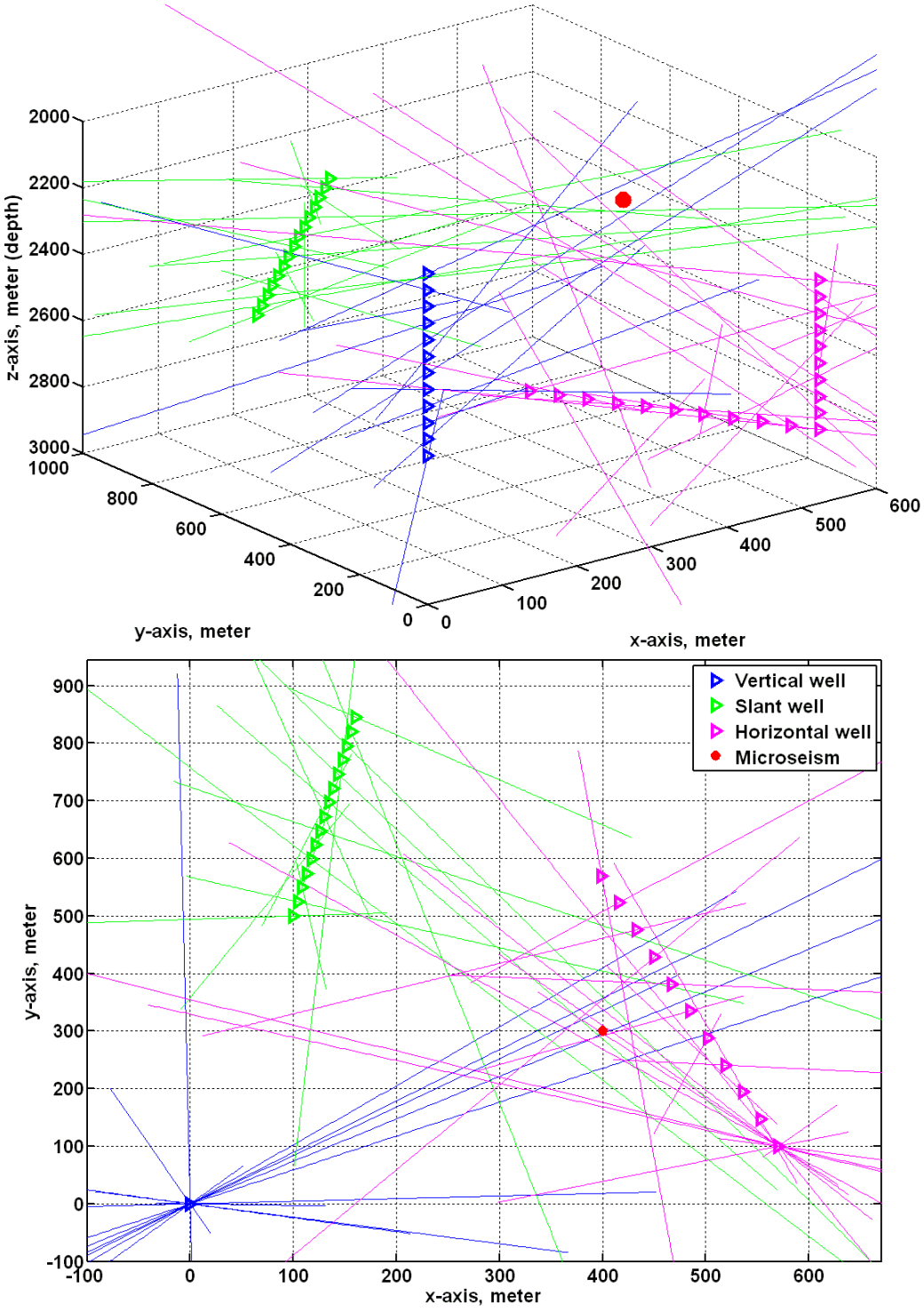

Figure A1.3: 3D and map views of raypaths of incident propagation derived on raw data from three wells.

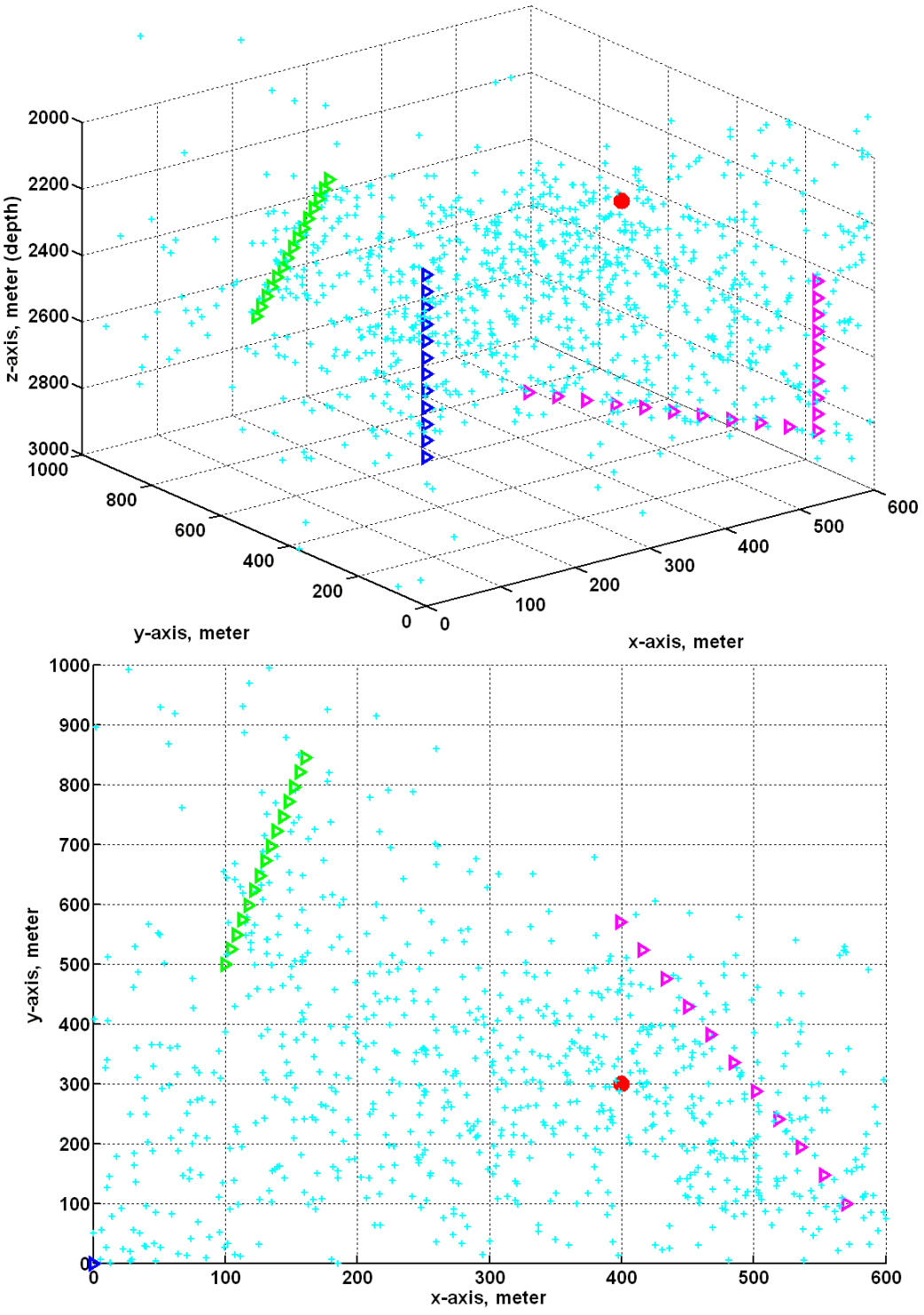

Figure A1.4: 3D and map views of nearest points of mutual raypaths of incident propagation, derived on raw data from three wells.

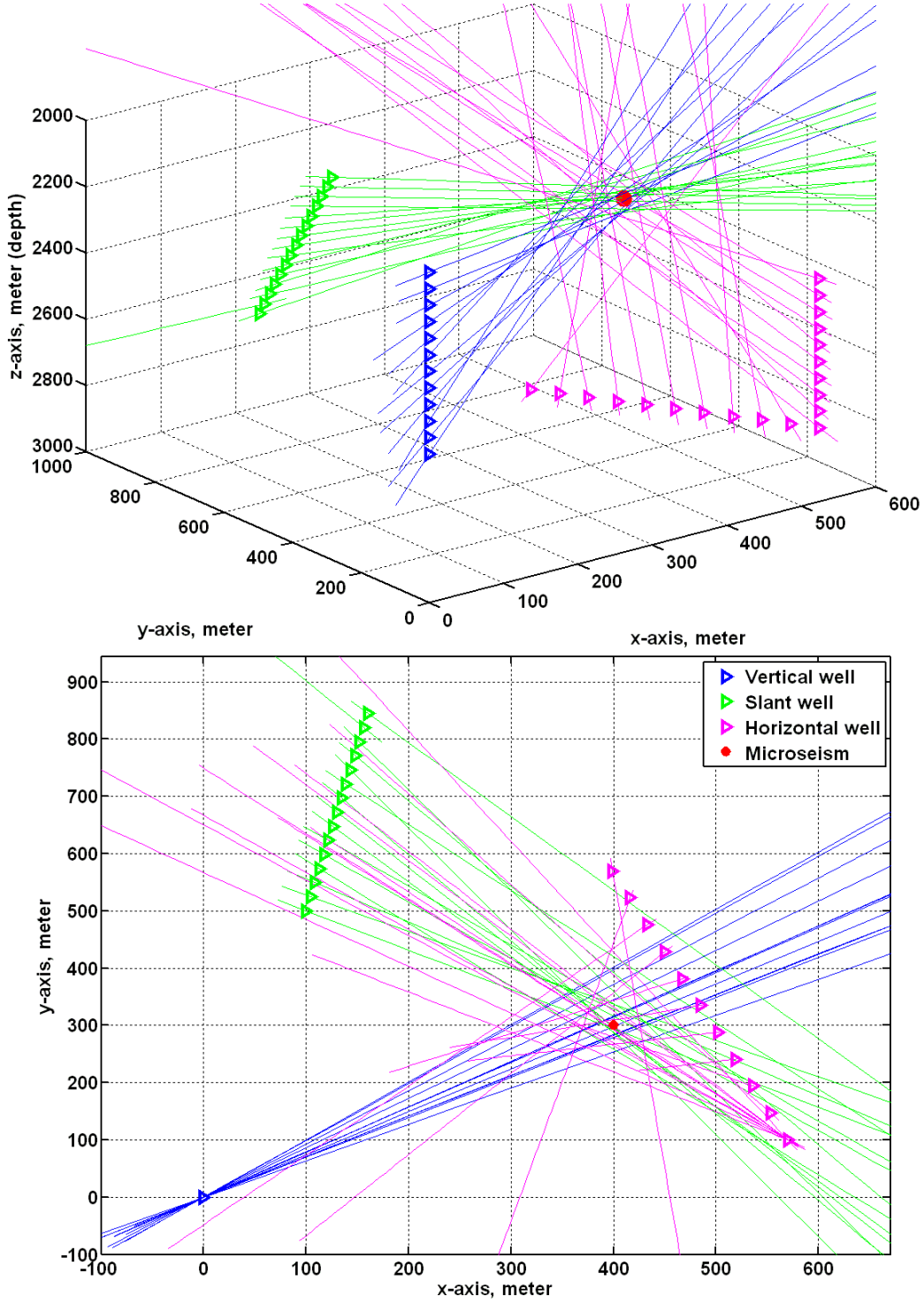

Figure A1.5: 3D and map views of raypaths of incident propagation derived on noise attenuated data from three wells.

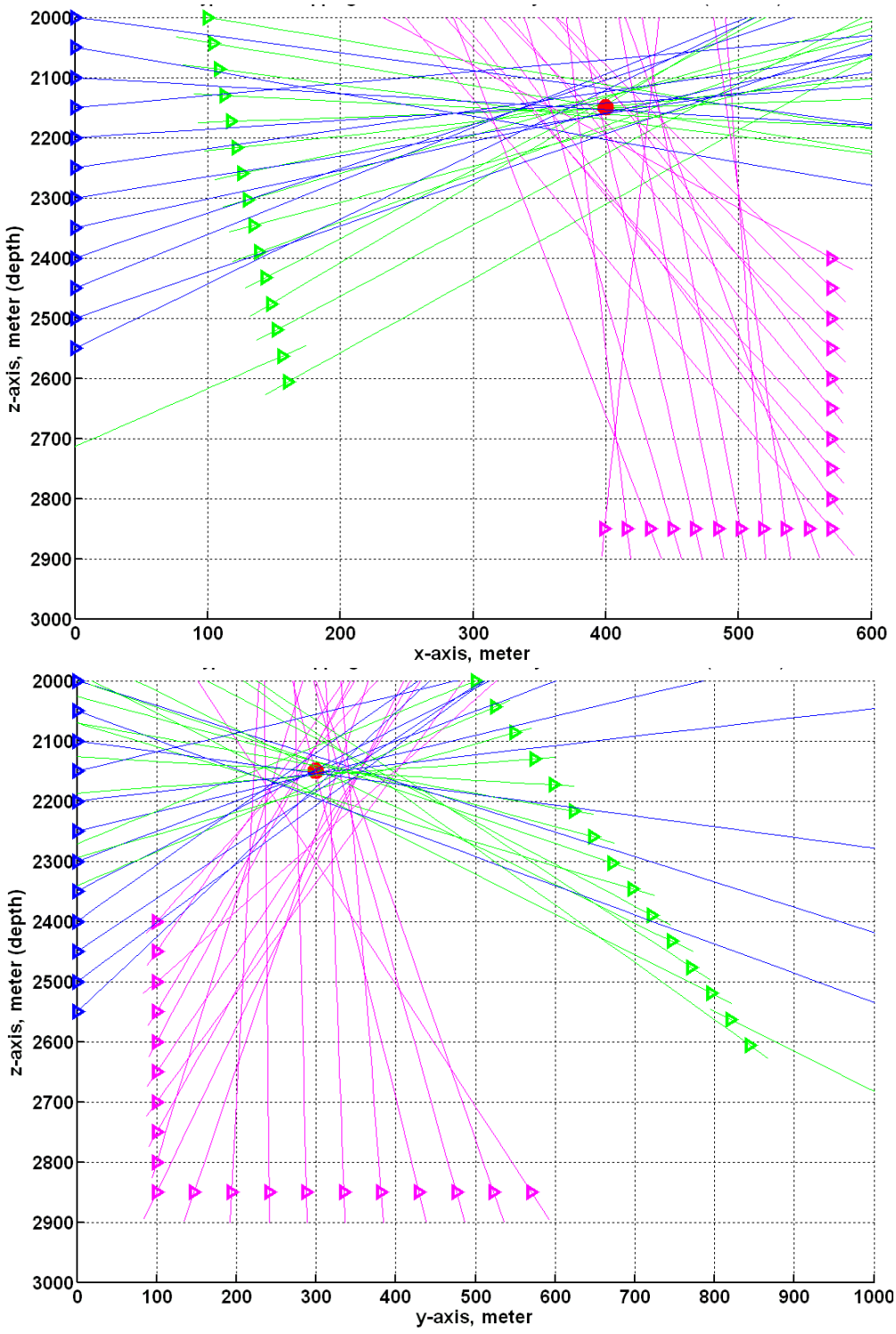

Figure A1.6: Section views of raypaths of incident propagation derived on noise attenuated data from three wells.

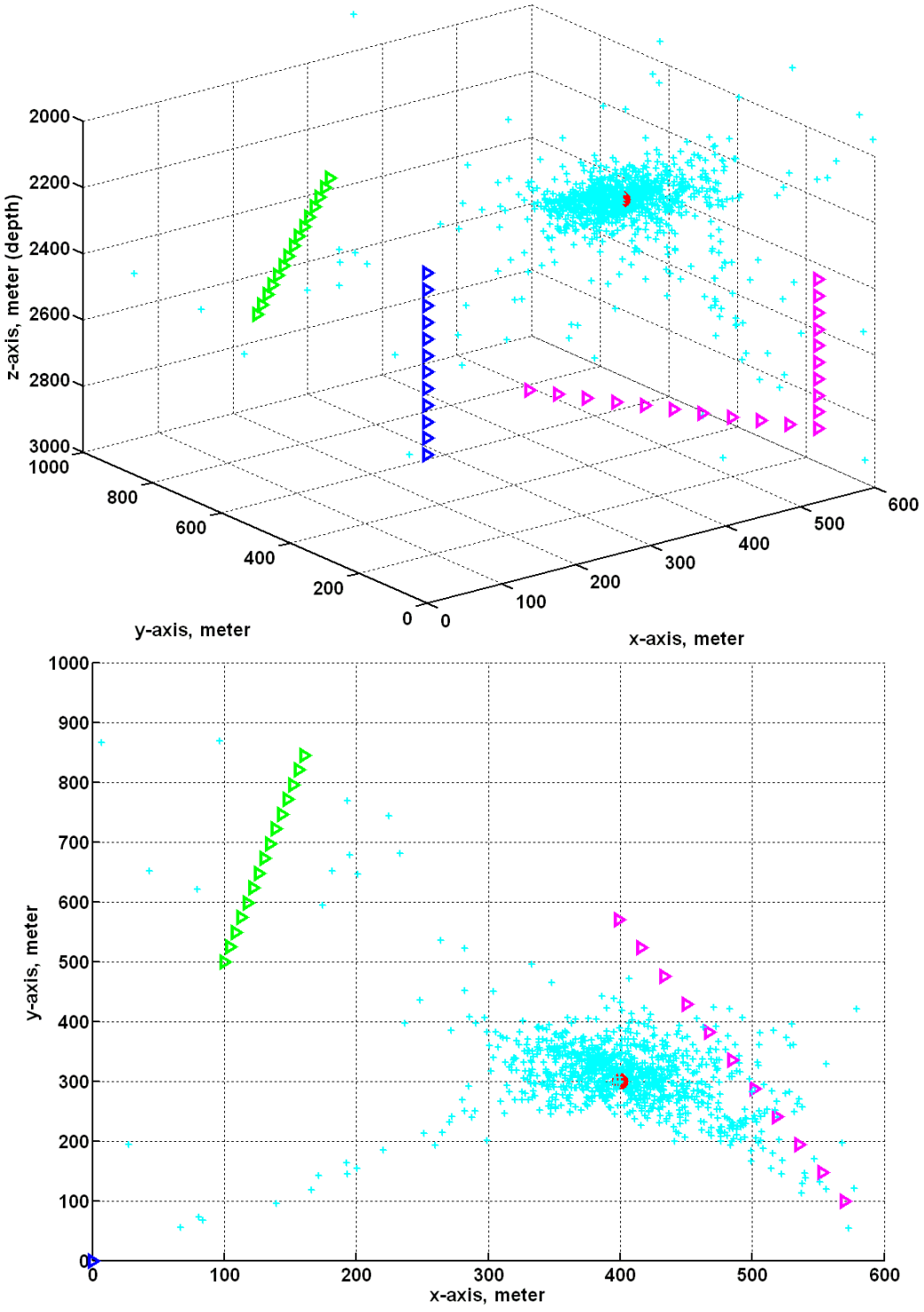

Figure A1.7: 3D and map views of nearest points of mutual raypaths derived on noise attenuated data from three wells.

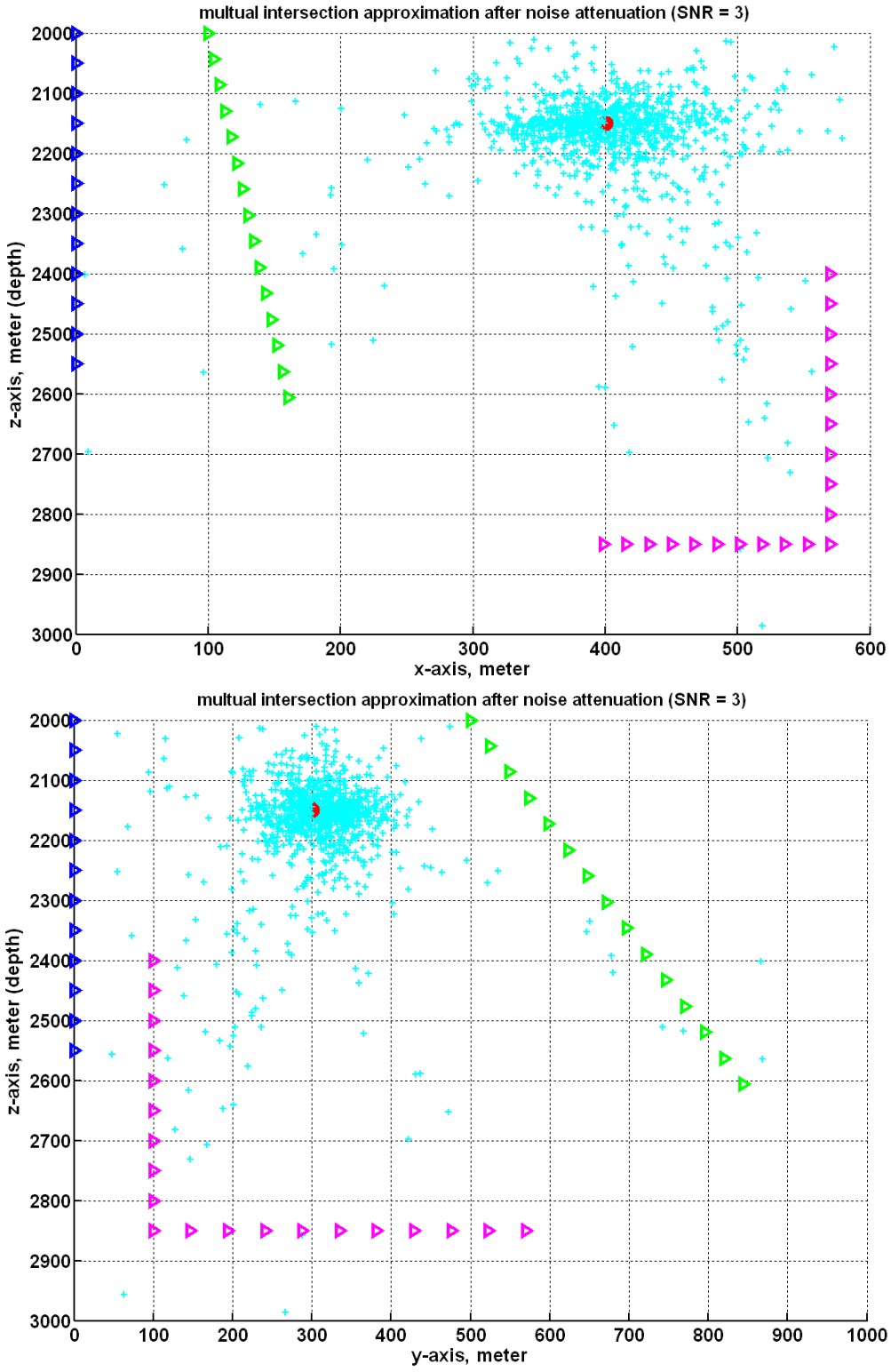

Figure A1.8: Section views of nearest points of mutual raypaths derived on noise attenuated data from three wells.

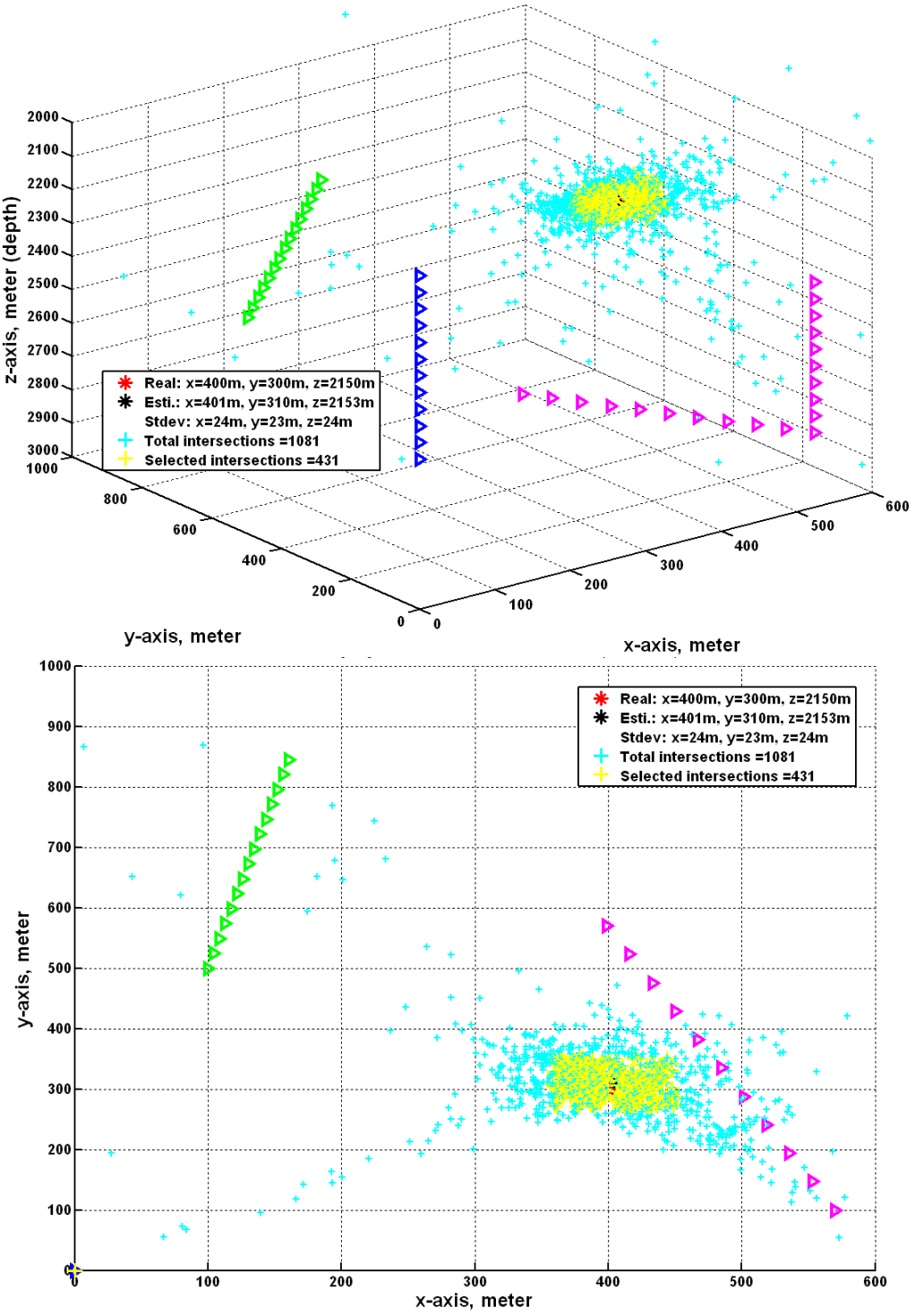

Figure A1.9: 3D and map views of hypocenter location estimated on noise attenuated data from three wells.

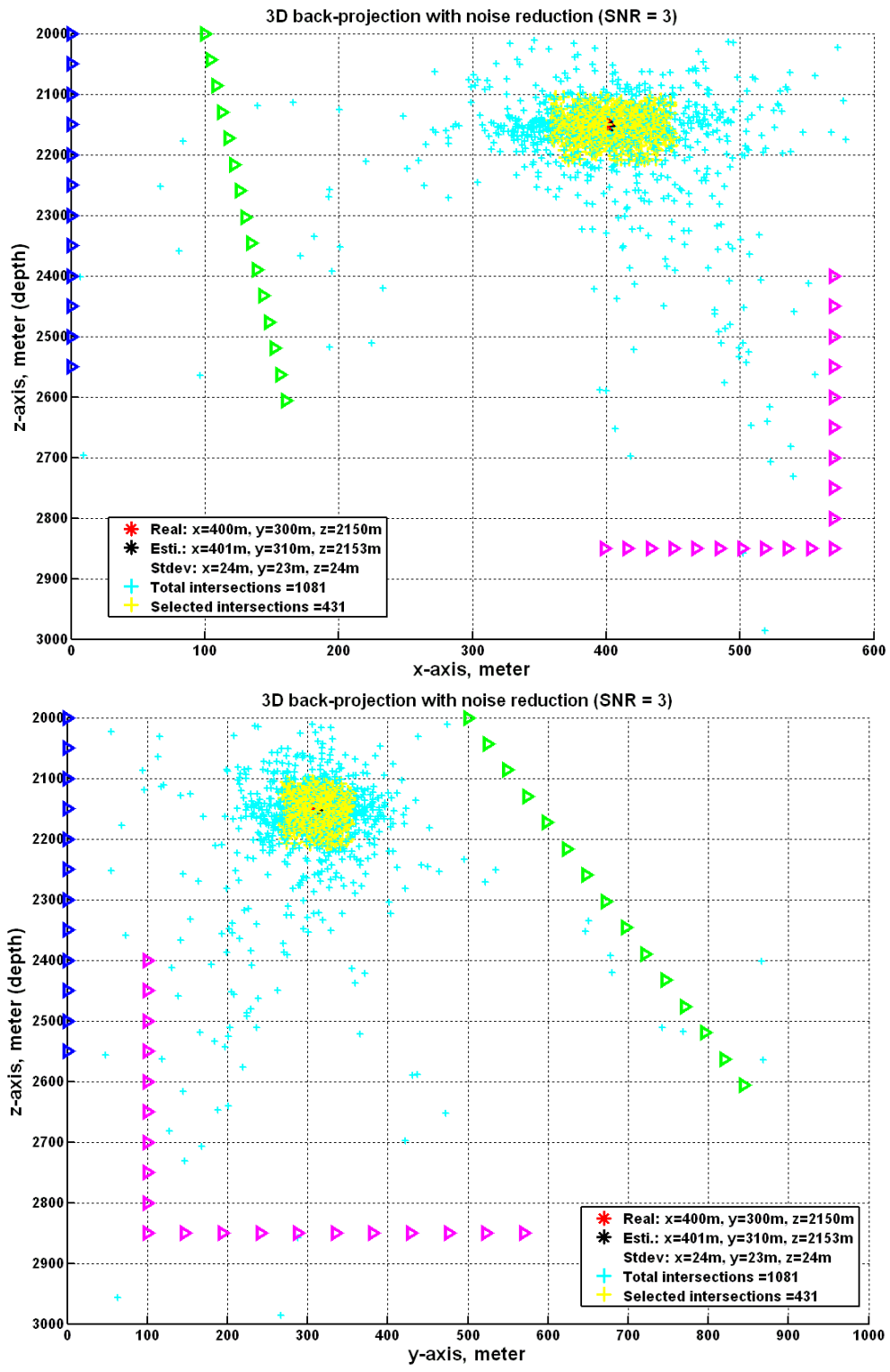

Figure A1.10: Section views of hypocenter location estimated on noise attenuated data from three wells.

REFERENCES

Albright, J. N., & Pearson, C. F. (1982). Acoustic emissions as a tool for hydraulic fracture location: experience at the Fenton Hill Hot Dry Rock site. Soc. Petr. Eng. Journal., 22 , 523-530.

Aster, R. C., Borchers, B., & Thurber, C. H. (2005). Parameter Estimation and Inversion Problems. Burlington, MA, U.S.A: Elsevier Academic Press.

Bancroft, J. C. (2009). Estimating the location of a microseismic event using a vertical array of receivers. CREWES Report, 21 , pp. 6.1-6.10.

Bancroft, J. C., Wong, J., & Han, L. (2010). Sensitivity measurements for locating microseismic events. CSEG Recorder, 35 , 27-36.

Bland, H. C., & Hogan, C. (2005). A hypocenter location method for microseismicity in complex regions. CREWES Research Report 17 , pp. 18.1-18.14.

Brady, B. T. (1977). Anomalous seismicity prior to rock bursts: Implications for earthquake prediction. Pure and Applied Geophysics, 115 , 357-374.

Brady, B. T. (1997). Seismic precursors before rock failures in mines. Nature, 252 , 549-552.

Chambers, K., Brandsberg-Dahl, S., Kendall, J. M., & Rueda, J. (2008). Testing the ability of surface arrays to locate microseismicity. 78th Ann. Int. Meeting, SEG Expanded Abstracts, (pp. 1436-1439).

Chen, Z., & Stewart, R. R. (2005). A multi-window algorithm for picking of microseismic events on 3C data. 75th Annual International Meeting, SEG, Expanded Abstracts, (pp. 1288-1291).

Eisner, L., Abbott, D., Barker, W. B., Lakings, J., & Thornton, M. P. (2008). Noise suppression for detection and location of microseismic events using a matched filter. SEG Ann. Int. Mtg., Expanded Abstracts, 27, (pp. 1431-1435).

Flinn, E. A. (1965). Signal analysis using rectilinearity and direction of particle motion. Proc. IEEE , 1874-1876.

Golub, G. H., & Reinsch, C. (1970). Singular value decomposition and least squares solution. Numerical Mathematics, 14 , 403-420.

Hasawega, H. S., Wetmiller, R. J., & Gendzwill, D. J. (1989). Induced seismicity in mines in Canada-an overview. Pure and Applied Geophysics, 129 , 423-453.

Hons. (2008). Seismic sensing: comparison of geophones and accelerometers using laboratory and field data. M.Sc. thesis, University of Calgary .

House, L. (1987). Locating microearthquakes induced by hydraulic fracturing in crystalline rock. Geophys. Res. Lett., 14 , 919-921.

Kolda, T. G., Lewis, R. M., & Torczon, V. (2003). Optimization by direct search: new perspectives on some classical and modern methods. Soc. for Indus. and Appl. Mathematics, 45 , 385-482.

Lakings, J. D., Duncan, P. M., Neale, C., & Theiner, T. (2006). Surface based microseismic monitoring of a hydraulic fracture well stimulation in the Barnett shale. 76th Ann. Int. Meeting, SEG Expanded Abstracts, (pp. 605-67).

Levenberg, K. (1944). A method for the solution of certain nonlinear problems in least squares. The Quarterly of Applied Mathematics, 2 , 164-168.

Lowrie, W. (1997). Fundamentals of geophysics. Cambridge University Press.

Maher, K. (2009). Microseismic mapping: Short Course Notes. CSPG/CSEG/CWLS Convention. Calgary, Alberta.

Mahrer, K. (2009). Microseismic mapping: Workshop Notes. CSPG/CSEG/CWLS Convention, (p. Slide 206). Calgary, Alberta.

Marquardt, D. (1963). An algorithm for least-squares estimation of nonlinear parameters. SIAM Journal on Applied Mathematics, 11 , 431-441.

Mathieson, A., Midgley, J., Dodds, K., Wright, I., Ringrose, P., & Saoul, N. (2010). CO2 sequestration monitoring and verification technologies applied at Krechba, Alberta. The Leading Edge, 29 , 216-222.

Maxwell, P. W. (1999). A new seismic sensor-at last. The Leading Edge, 18 , 1182-1183.

Maxwell, P. W., Du, J., & Shemeta, J. (2008). Passive seismic and surface monitoring of geomechanical deformation associated with steam injection. The Leading Edge, 27 , 1176-1184.

Maxwell, S. C., & Urbancic, T. I. (2001). The role of passive microseismic monitoring in the instrumented oilfield. The Leading Edge, 20 , 636-639.

Monroe, J. S., & Wicander, R. (1997). The Changing Earth: Exploring Geology and Evolution, 2nd ed. Belmont West Publishing Co.

Munro, K. A. (2005). Analysis of microseismic event picking with application to landslide and oil-field monitoring setting. M.Sc. thesis, University of Calgary .

Munro, K. A. (2004). Automatic event detection and picking P-wave arrivals. CREWES Research Report 18 , pp. 12.1-12.10.

Oye, V., & Roth, M. (2003). Automated seismic event location for hydrocarbon reservoirs. Computers and Geosciences, 29 , 851-863.

Pavlis, G. L. (1992). Appraising relative earthquake location errors. Bull. Seismol. Soc. Am., 82 , 836-859.

Press, W. H. (1992). Numerical recipes in FORTRAN: the art of scientifc computing. Cambridge University Press.

Rutledge, J. T., Phillips, W. S., & Schuessler, B. K. (1998). Reservoir characterization using oil-production-induced microseismicity. Tectonophysics, 289 , 129-152.

Ruud, B. O., Husebye, E. S., Ingate, S. F., & Christoffersson, A. (1988). Event location at any distance using seismic data from a single, three component station. Bull. Seismol. Soc. Am., 78 , 308-325.

Saari, J. (1991). Automated phase picker and source location algorithm for local distances using a single three-component seismic station. Tectonophysics, 189 , 37-315.

Torczon, V. (1997). On the convergence of pattern search algorithms. SIAM Jour. on Optimization : 7 , 1-25.

Verdon, J. P., Kendall, J. M., White, D. J., Angus, D. A., Fisher, Q. J., & Urbancic, T. (2010). Passive seismic monitoring of carbon dioxide storage at Weyburn. The Leading Edge, 29 , 200-206.

Vidale, J. E. (1986). Complex polarization analysis of particle motion. Bull. Seis. Soc. America, 76 , 1393-1397.

Vose, M. D. (1999). The simple genetic algorithm: foundations and theory. MIT Press, Cambridge.

Whitley, D. (1994). A genetic algorithm tutorial. Statistics and Computing, 4 , 65-85.

Zhou, R., Huang, L., & Rutledge, J. (2010). Microseismic event location for monitoring CO2 injection using double difference tomography. The Leading Edge, 29 , 208-214.